# 3D Segmentation of Cam-Type Pathological Femurs with Morphological Snakes

by

**Gabriel Telles O'Neill**

A thesis submitted to
the Faculty of Graduate and Postdoctoral Studies
In partial fulfillment of
the requirements for the degree of

Master in Computer Science

Ottawa-Carleton Institute for Computer Science
School of Information Technology and Engineering
The University of Ottawa

Ottawa, Ontario, Canada

June 2011

# Abstract

We introduce a new way to accurately segment the 3D femur from pelvic CT scans. The femur is a difficult target for segmentation due to its proximity to the acetabulum, irregular shape and the varying thickness of its hardened outer shell. Atypical bone morphologies, such as the ones present in hips suffering from Femoral Acetabular Impingements (FAIs) can also provide additional challenges to segmentation. We overcome these difficulties by (a) dividing the femur into the femur head and body regions (b) analysis of the femur-head and neighbouring acetabulum's composition (c) segmentations with two levels of detail – rough and fine contours.

Segmentations of the CT volume are performed iteratively, on a slice-by-slice basis and contours are extracted using the morphological snake algorithm. Our methodology was designed to require little initialization from the user and to deftly handle the large variation in femur shapes, most notably from deformations attributed to cam-type FAIs. Our efforts are to provide physicians with a new tool that creates patient-specific and high-quality 3D femur models while requiring much less time and effort.

We tested our methodology on a database of 20 CT volumes acquired at the Ottawa General Hospital during a study into FAIs. We selected 6 CT scans from the database, for a total of 12 femurs, considering wide inter-patient variations. Of the 6 patients, 4 had unilateral cam-type FAIs, 1 had a bilateral cam-type FAI and the last was from a control group. The femurs segmented with our method achieved an average volume overlap error of 2.71 ± 0.44% and an average symmetric surface distance of 0.28 ± 0.04 mm compared against the same, manually segmented femurs. These results are better than all comparable literature and accurate enough to be used to in the creation of patient-specific 3D models.

# Acknowledgments

To start off, I would like to thank my supervising professors, Dr. WonSook Lee (School of Information Technology and Engineering, The University of Ottawa) and Dr. Amiya Nayak (School of Information Technology and Engineering) for sharing their invaluable knowledge, advice and guidance.

Thank you to my lab-mates, Mauricio, Ming, Nima and Ava for being great sources of commiseration.

I would also like to thank Dr. Paul Beaulé (Division of Orthopedic Surgery, Faculty of Medicine, The University of Ottawa) for his medical insight in regards to the human hip, supplying us with our medical data and Anna Fazekas (The Ottawa Hospital) for being all-around helpful.

Thanks to the National Science and Engineering Research of Canada for awarding me with the Alexander Graham Bell Canada Graduate Scholarship which funded this research.

Finally, thanks to all my friends and family whose unwavering support fills me with strength. Special mention goes to my mother and father whose gifts I can never fully repay- and yet shall forever endeavour to try.

# Table of Contents

Abstract ..... i
Acknowledgments ..... ii
Table of Contents ..... iii
List of Tables ..... v
List of Figures ..... vi
Glossary of Terms ..... viii
Chapter 1 - Introduction ..... 1
1.1 Motivation ..... 1
1.2 Problem Statement ..... 2
1.3 Proposed Solution ..... 3
1.4 Thesis Organisation ..... 4
Chapter 2 - Literature Review ..... 5
2.1 The Hip Joint ..... 5
2.1.1 Anatomy ..... 5
2.1.2 Function ..... 10
2.2 Femoral Acetabular Impingement ..... 12
2.2.1 What is F.A.I? ..... 12
2.2.2 Symptoms ..... 13
2.2.3 Types of F.A.I ..... 13
2.2.4 Surgical Correction ..... 14
2.2.5 Prevalence ..... 14
2.3 Computed Tomography ..... 15
2.4 Current Medical Segmentation Methods ..... 17
2.4.1 Manual Segmentation ..... 17
2.4.2 Energy Minimizing Curves ..... 18
2.4.3 Level Set Based ..... 21
2.4.4 Model Based ..... 24
2.5 Hip Segmentation Methods from CT/MRI ..... 27
Chapter 3 - Methodology Overview ..... 32
3.1 Objective ..... 32
3.2 Complications ..... 32
3.2.1 Technical limitations of CT scans ..... 32
3.2.2 Patient-specific complications ..... 33
3.2.3 Object segmentation complications ..... 34
3.3 Solution Overview ..... 37
3.4 Morphological Snakes ..... 40
Chapter 4 - Segmentation ..... 44

4.1 Input ..... 44
4.2 Pre-Processing the Hospital-Provided Input ..... 46
4.3 Initializing Regions of Interest ..... 48
4.3.1 ROI for the Femur Head ..... 49
4.3.2 ROI for the Femur Body ..... 51
4.4 Acetabular Rim Removal ..... 52
4.4.1 Thresholding ..... 53
4.4.2 Creating the mask ..... 54
4.4.3 Cut-Out Filling ..... 55
4.5 Pre-processing Region of Interest contents ..... 57
4.5.1 Ceiling Thresholding ..... 57
4.5.2 Flooring Thresholding ..... 58
4.5.3 Upscaling ..... 59
4.6 Femur Head ..... 60
4.6.1 Primer slice segmentation ..... 62
4.6.2 Subsequent Slice Segmentation ..... 67
4.7 Femur Body ..... 73
4.7.1 Primer Slice Segmentation ..... 74
4.7.2 Subsequent Slice Segmentation ..... 75
4.8 Post-Processing ..... 80
Chapter 5 - Experimental Results and Evaluations ..... 81
5.1 Hospital Database ..... 81
5.1.1 DICOM Format ..... 81
5.1.2 CT Scans ..... 82
5.2 Testing Database ..... 83
5.3 Experimental Setup ..... 86
5.4 Segmentation Qualitative Results ..... 87
5.5 Segmentation Quantitative Results ..... 97
5.6 Results Evaluation and Discussion ..... 103
5.6.1 Segmentation Process ..... 103
5.6.2 Qualitative Results ..... 104
5.6.3 Quantitative Results ..... 106
5.6.4 Comparison ..... 107
Chapter 6 - Conclusion ..... 109
6.1 Contributions ..... 110
6.2 Future Research ..... 110
References ..... 112
Appendix A Anatomical Terms ..... I

# List of Tables

Table 2.1: Normal values for the Range of Motion of hip-joints [14] ..... 11
Table 4.1: Sample sequence of initial contours (red) and final contours (green) starting from the primer slice and iterating towards the top of the femur head ..... 71
Table 4.2: Sample sequence of initial contours (red) and final contours (green) starting from the primer slice and iterating towards the bottom of the femur head ..... 72
Table 4.3: Sample sequence of initial contours (red) and final contours (green) starting from the primer slice and iterating towards the top of the femur ..... 78
Table 4.4: Sample sequence of initial contours (red) and final contours (green) starting from the $Z_s$ and continuing with its neighbouring slices ..... 79
Table 5.1: Breakdown of the 20 patient from the Hospital's database ..... 81
Table 5.2: Spatial properties of pelvic radiographs ..... 82
Table 5.3: Spatial properties of pelvic CT scans ..... 82
Table 5.4: Characteristics of the six patients who had their femurs manually segmented ..... 83
Table 5.5: Test parameters for Morphological snake with edge-threshold-balloon (Rough Contours) ..... 87
Table 5.6: Test parameters for morphological snake with snake-balloon-difference-radius (Fine Contours) ..... 87
Table 5.7: Comparison of our segmentation method results for the femur head with those from a manual segmentation ..... 88
Table 5.8: Comparison of our segmentation method results for the femur body with those from a manual segmentation ..... 89
Table 5.9: Comparison of Volumetric Models for Patient #1 ..... 91
Table 5.10: Comparison of Volumetric Models for Patient #2 ..... 92
Table 5.11: Comparison of Volumetric Models for Patient #3 ..... 93
Table 5.12: Comparison of Volumetric Models for Patient #4 ..... 94
Table 5.13: Comparison of Volumetric Models for Patient #17 ..... 95
Table 5.14: Comparison of Volumetric Models for Patient #20 ..... 96
Table 5.15: Voxel Overlap Errors for each femur ..... 100
Table 5.16: Symmetric Surface Distances with no slice restriction on Y ..... 100
Table 5.17: Symmetric Surface Distances with Y restricted to the same slice as X ..... 101
Table 5.18: Slice-by-slice case study of qualitative results obtained for Patient #2's left femur 101
Table 5.19: Time estimates for individual steps in our method's segmentation process ..... 104
Table 6.1 List of Anatomical Directions ..... I

# List of Figures

Figure 2.2: Upper extremity of right femur [4] ..... 7
Figure 2.3: Right pelvis, right lateral view [4] ..... 7
Figure 2.4: Opened view of the hip joint [8] ..... 8
Figure 2.5: Typical structure of a long bone (a) Diaphysis, epiphysis and medullary cavity (b) compact bone surrounding the yellow bone marrow in the medullary cavity (c) spongy bone and compact bone in the epiphysis [9] ..... 10
Figure 2.6: (a) Ball-and-socket joint [12] (b) Hinge joint [13] ..... 11
Figure 2.7: (a) Anterior rotations of the hip (b) Lateral rotation of the hip [5] ..... 12
Figure 2.8: Single slice from a CT scan crossing a patient's femur head ..... 16
Figure 2.9: Transverse Section of the Hip Joint [5] ..... 17
Figure 2.10: Evolution of the balloon curve as it inflates to detect the contour of the left heart ventricle [25] ..... 19
Figure 2.11: Convergence of a snake using (left) traditional potential forces (middle) distance potential forces (right) GVF external forces [27] ..... 20
Figure 2.12: Level sets of an embedding functions u for a closed curve C in $R^2$ [30] ..... 22
Figure 2.13: Two examples of image landmarks which can be used to construct a PDM [39] ... 24
Figure 2.14: Enhancing the joint-space by the Hessian filter (a) noisy acetabulum and femur (b)The left, middle and right images show the results of filtering the initial image in the horizontal, diagonal and vertical direction respectively (c) Results of Hessian Filtering [51]28
Figure 2.15: Examples of segmentation using ASM of acetabulum on CT slice of hip-joint. (a) Initialisation (b) after two iterations (c) after size iteration (d) after twelve iterations [39] .... 30
Figure 3.1: (left) decreased CCD angle (middle) normal CCD angle (right) increased CCD angle [57] ..... 33
Figure 3.2: (left) CT slice where the femur's topology consists of two disconnect objects (right) Antero-posterior view of this slice's location ..... 35
Figure 3.3: (a) CT slice of femur shaft displaying thick compact bone shell (b) CT slice of femur head displaying thin compact bone shell (c)Cross-section of femur top that displays compact & spongy bone distribution [10] ..... 36
Figure 3.4: CT slice depicting the feathered edges of the top of a femur head ..... 37
Figure 3.5: Region of interest for the femur (left) head (right) body ..... 38
Figure 3.6: cross-section (left) prior to the acetabular rim being cut-out (right) after the acetabular rim is cut-out and filled ..... 38
Figure 3.7: Sample process of segmenting the primer slice of the femur head's ROI ..... 39
Figure 3.8: Sample process of obtaining an initial contour for an un-segmented slice of the femur head's ROI. Here, $Z_i$ is a slice in need of an initial contour while $Z_{i+1}$ is its fully segmented neighbour ..... 40
Figure 4.1: (a) Radiograph of a patient's hip and waist (b) region commonly scanned by CT machine when investigating FAIs (c) Example top-most slice (d) Example bottom-most slice ..... 45

Figure 4.2 Average voxel intensity distribution as observed from twenty pelvic CT scans. The blue bars demark the intensities at which the hospital-provided CT data is cropped during pre-processing ..... 46
Figure 4.3: Example $ROI_H$ is red seen from the patient's (left) front (right) right [59] ..... 50
Figure 4.4: Example $ROI_B$ in red with $Z_s$ as a blue stripe seen from patient's (left) front (right) right [59] ..... 51
Figure 4.5: CT slice showing the potential proximity of the femur to acetabulum ..... 53
Figure 4.6: Example slice from the femoral head ROI before (left) and after (right) thresholding ..... 53
Figure 4.7: (left) Example initial mask for acetabular cut-out (right) Same mask after dilation and flood-filling, all regions not shaded in grey are used as the final mask ..... 54
Figure 4.8: (left) Example acetabular cut-out with black fill (right) Same cut-out with low-gradient fill ..... 55
Figure 4.9: slice (left) before ceiling-thresholding (right) after ceiling-thresholding ..... 57
Figure 4.10: Cross-section of the femur body (left) before flooring threshold applied (right) after flooring thresholding applied ..... 58
Figure 4.11: Progression chart of each slice's segmentation where the primer slice appears in blue and the subsequent slices in red. Note that the ROI's primer slice, top-most slice and bottom-most slice are denoted as $Z_p$, $Z_t$ and $Z_b$ respectively ..... 61
Figure 4.13: Primer slice with superimposed rough final contour in black ..... 64
Figure 4.14: Primer slice(left) with superimposed circle from Hough Transform (right) with superimposed widened circle ..... 65
Figure 4.15: Example of how Hough's transform can be used to recover from errors in the rough step: (a) initial contour for the rough step (b) final contour for the rough step with error due to greater trochanter (c) Best fitting circle from Hough Circle Transform (d) Widened circle ... 66
Figure 4.16: Example final segmentations for the femur head detected during the rough (left) and fine (right) contour extraction ..... 67
Figure 4.17: (a) Slice $Z_i$ in need of an initial contour (b) Slice $Z_{i+1}$ with final contour (c) Slice $Z_{i+1}$ with dilated final contour (d) Slice $Z_i$ using $Z_{i+1}$'s dilated final contour as an initial contour ..... 69
Figure 4.18: (left) Initial contour for rough step (right) final contour for rough step ..... 74
Figure 4.19: (left) Initial contour for the fine step (right) Final contour for the fine step ..... 75
Figure 4.20: Slices (left) $Z_s$ where the femur appears as two disconnected objects (right) $Z_{s+1}$ where the femur appears as a single connected object ..... 76
Figure 4.21: (a) Final contour for slice $Z_{s+1}$ in $ROI_B$ (b) Voxels of set $V_B$ (c) Final contour for slice $Z_{s+1}$ in $ROI_H$ (d) Voxels of set $V_H$ (e) Volume for $ROI_H$ subtracted from $ROI_B$ (f) slice $Z_s$ with its initial contour ..... 77
Figure 4.22 Sample union of the 3D model from $ROI_H$ and the 3D model from $ROI_B$ ..... 80
Figure 5.1: Femur and acetabulum appear (left) well-spaced (right) close at points ..... 84
Figure 5.2: Cross-sections where the femur head appears (left) near-circular (right) deformed .. 84
Figure 5.3: Concavity between femur head and greater-trochanter is (left) wide (right) narrow . 85
Figure 5.4: Various shapes of the femur head's fovea ..... 85
Figure 6.1 Human Anatomical Directions [67] ..... I
Figure 6.2 Planes of human anatomy [68] ..... II

# Glossary of Terms

| | |
|---|---|
| **2D** | Two Dimensional |
| **3D** | Three Dimensional |
| **AAM** | Active Appearance Model |
| **ASM** | Active Shape Model |
| **ACM** | Active Contour Model |
| **CAT** | Computerized Axial Tomography |
| **CCD** | Caput-Collum-Diaphyseal |
| **CT** | Computed Tomography |
| **DICOM** | Digital Imaging and COmmunication in Medicine |
| **DRR** | Digitally Reconstructed Radiograph |
| **FAI** | Fermoral-Acetabular Impingement |
| **GPU** | Graphical Processing Unit |
| **HTBS** | Hip-To-Be-Square |
| **JATH** | Joined-At-The-Hip |
| **MRI** | Magnetic Resonance Imaging |
| **PCA** | Principle Component Analysis |
| **ROI** | Region of Interest |
| **SSD** | Symmetric Surface Distance |
| **SSM** | Statistical Shape Model |
| **VOE** | Volume Overlap Error |

# Chapter 1 - Introduction

## 1.1 Motivation

In image processing, **segmentation** is the subdivision of a digital image into its contained regions or objects [1]. Segmentation's goal is to find a new representation of an image which is more meaningful and easier to analyse [2]. Practically speaking, segmentation is used to label the pixels of digital image or the voxels of a digital volume such that similarly labelled pixels/voxels can be used to extract areas of interest.

In the domain of **medical imaging**, segmentation can be used to extract to contours of organs or bones. The shapes of these extracted contours can later be used by physicians to aid in their diagnosis. In the case of segmented volumetric data, such as **Computed Tomographic** (CT) Imaging, segmented objects can be used to create three-dimensional (3D) models which can be the subjects of further investigation and testing in a medical environment.

Our research has focused on a particular ailment; **Femoral-Acetabular Impingment** (FAI), which refers to a common condition among young adults with hip pain [3] where there exists deformities on the hip bones. These deformities appear as bumps on the bone surfaces which cause unwanted collisions with its associated bone during hip movement, eventually leading to the deterioration of the joint's soft tissue. Segmenting a pelvic CT scan allows models of the bones that make up a patient's hip to be created. These models can then be used by physicians to detect the locations and severity of impingement as well as aid in the planning of minimally invasive procedures to correct the condition.

We are motivated by the medical need for patient-specific 3D models of hip bones for the treatment of FAIs. At present, the best segmentation results for bones from pelvic CT scans

comes from manually labelling the voxels. While providing the most accurate results, manual segmentation is extremely time-consuming; requiring hours or days of work for a single pelvic scan. Our goal is to create a machine-driven segmentation scheme which greatly reduces the time required to segment the hip-bones from a pelvic CT scan while returning the sufficiently accurate results required for physicians to treat FAIs.

## 1.2 Problem Statement

*This thesis addresses the problems of developing algorithms to segment the bones that constitute the human hip.*

In the field of image processing, segmenting non-trivial images is reputed as one of the most difficult tasks [1]. Pelvic CT scans have a number of elements that complicate segmentation. These complications include:

- CT scans are usually taken at a comparatively low image resolution
- CT scans do not contain any colour information
- CT scans contain significant amounts of noise
- Visible separation between the two hipbones may not exists at all points
- Bone size and shape differ greatly between individuals
- The orientation of a patient's leg and pelvis differ between scans
- Bone form may differ from the norm due to a pathological disease

In the face of these difficulties, the primary question this research seeks to answer is:

- How can the femur in a hip joint be accurately, robustly and quickly segmented from a CT volume?

In addition, to the driving question of this research, we seek to answer the following secondary question:

- Are the 3D models created from our segmentations sufficiently accurate to aid in the diagnosis and treatment of patients with FAIs?

## 1.3 Proposed Solution

This section details the methodology we use to solve our primary question in the face of the previously listed complications:

1. We have a user initialise our segmentation strategy. This entails the placement of two regions of interest (ROI); one which covers the femur's heads while the other covers the femur's body. Appended to the ROI for the femur head is an approximation of its spherical center while the ROI for the femur body includes the index number of an exceptional CT slice. The user also has the option of modifying our default segmentation parameters. This concludes the manual portion of our segmentation strategy.
2. The content of each ROI is pre-processed. This starts by re-encoding the intensities for each voxel in the hospital-provided CT volume into more convenient grayscale values. Also, a ceiling threshold can be used to emphasize bone-like voxels while a flooring threshold can be used to minimize the impact of soft tissue during segmentation.
3. In order to negate any influence the acetabulum may have during segmentation, we isolate its shape and remove it. The acetabular rim is composed of a thicker and denser shell of compact bone than the femur head, making it easier to extract. To diminish its

influence during the segmentation procedure, sections of the acetabulum near the femur head are replaced with a low-gradient fill.

4. The femur head is segmented using the Morphological Snakes algorithm on sequential slices of the femur head's ROI. The process starts with the mid-most slice of the region of interest, using morphological snakes to perform a rough, then a fine segmentation. After this first slice, the femur is segmented sequentially outwards until all of the slices in the region of interest have had their contours extracted.
5. Similarly, the femur-body is segmented using the Morphological Snakes algorithm on sequential slices of the femur-body's ROI. The process starts with the bottom-most slice of the region of interest, using morphological snakes to perform a rough, then a fine segmentation. After this first slice, the femur is segmented sequentially upwards until all of the slices in the region of interest have had their contours extracted.
6. The extracted contours for the femur head and femur body are joined together to create a 3D single model for the femur.

## 1.4 Thesis Organisation

The rest of this thesis is organized as follows: Chapter 2 contains literature presenting background information of the human hip, femoral-acetabular impingements, computed tomography and medical segmentations methods. Chapter 3 performs an overview of our objective, the complications associated with that objective and our proposed solution. Chapter 4 describes our new femur-segmentation method in detail. Chapter 5 lists our qualitative & quantitative experimental results followed by evaluations and discussion. Chapter 6 marks our conclusion along with the direction of future research.

# Chapter 2 - Literature Review

## 2.1 The Hip Joint

Appendix A lists the names and descriptions of common anatomical terms.

### 2.1.1 Anatomy

The hip joint, scientifically known as the *acetabulofemoral joint*, exists between the pelvis and the thigh (Figure 2.1). To understand how this joint works, it is most helpful to look at the structure of its bones.

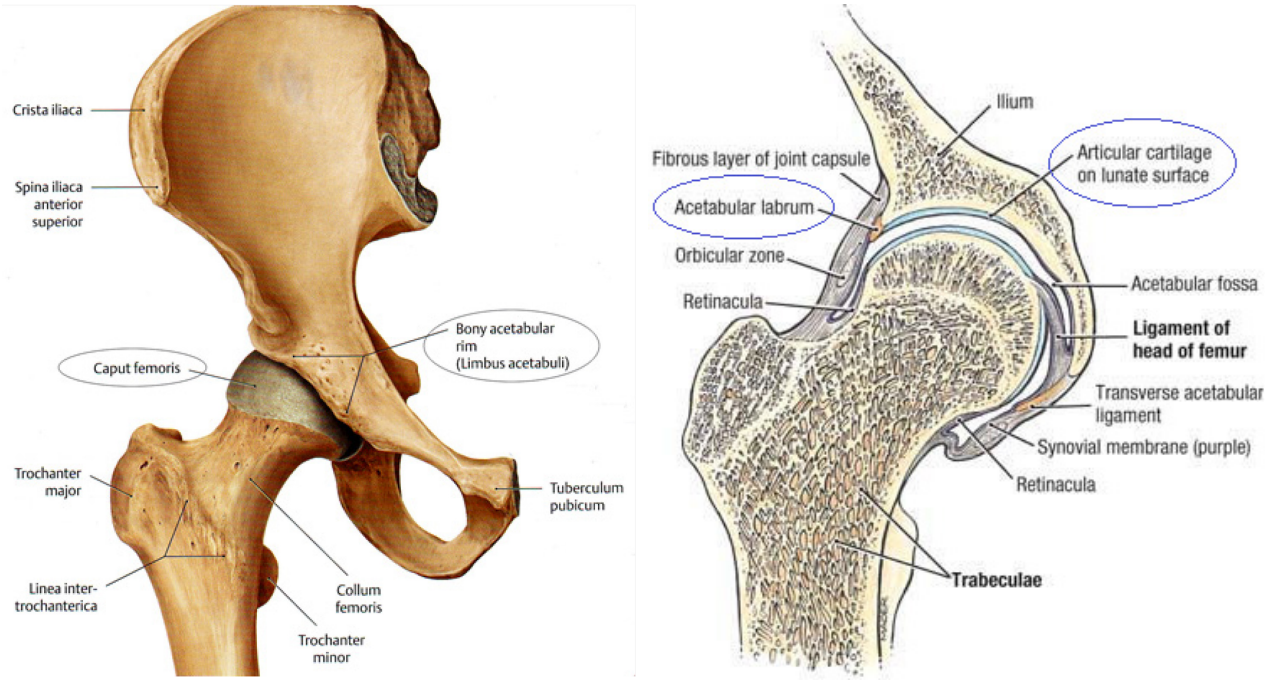


*Figure 2.1: (left) Bony Features of the Hip Joint [4] (right) Coronal Section of the Hip Joint [5]*

The **thigh** is composed of a single bone, called the *femur*, which is the longest bone in the human body. The upper extremity of the femur (Figure 2.2), is involved in the workings of the hip joint while the lower extremity is integral to the knee joint. The upper extremity of the femur has a number of notable features:

- The **femur head**, or *caput femoris*, is the rounded end of the femur. Its surface comes in the closest contact with the pelvic bones and can generally be approximated with the shape of a sphere.
- The **pit** for the ligament of the head of the femur, or *fovea capitis femoris*, is an indentation in the otherwise spherical surface of the femur-head(Figure 2.4)
- The **femur shaft/body**, or *corpus femoris*, is the near-cylindrical tube which makes up the majority of the femur.
- The **femur neck**, or *collum femoris*, is a bony-bar which spouts from the femur body which acts as a bridge between the femoral head and body.
- The **intertrochanteric line**, or *linea intertrichanterica*, is a bony ridge found on the anterior side of the femur, where the femoral neck and body join.
- The **greater trochanter**, or *trochanter major*, is a large bony-bump at the top of the intertrochanteric line. This bump serves as the attachment point for muscles of the buttocks.
- The **lesser trochanter**, *or trochanter minor*, is a small bony bump at the bottom of the intertrochanteric line. This bump serves as the attachment point for muscles of the buttocks and thigh.

The **pelvis** on the other hand is composed of multiple bones, namely the sacrum, illium, ischium, pubic bone, pubic symphysis, acetabulum and coccyx. Of these, it is the acetabulum (Figure 2.3) which comes into closest contact with the femur. The acetabulum can be described as a shallow, semi-spherical cup with prominent, but uneven, rim. It is into the acetabulum that the femoral head joins the pelvis.

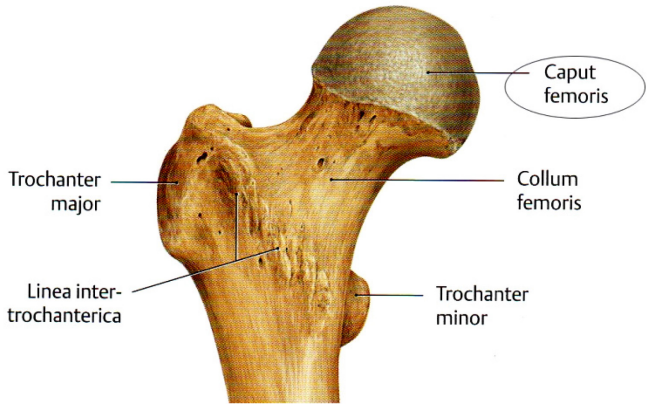


*Figure 2.2: Upper extremity of right femur [4]*

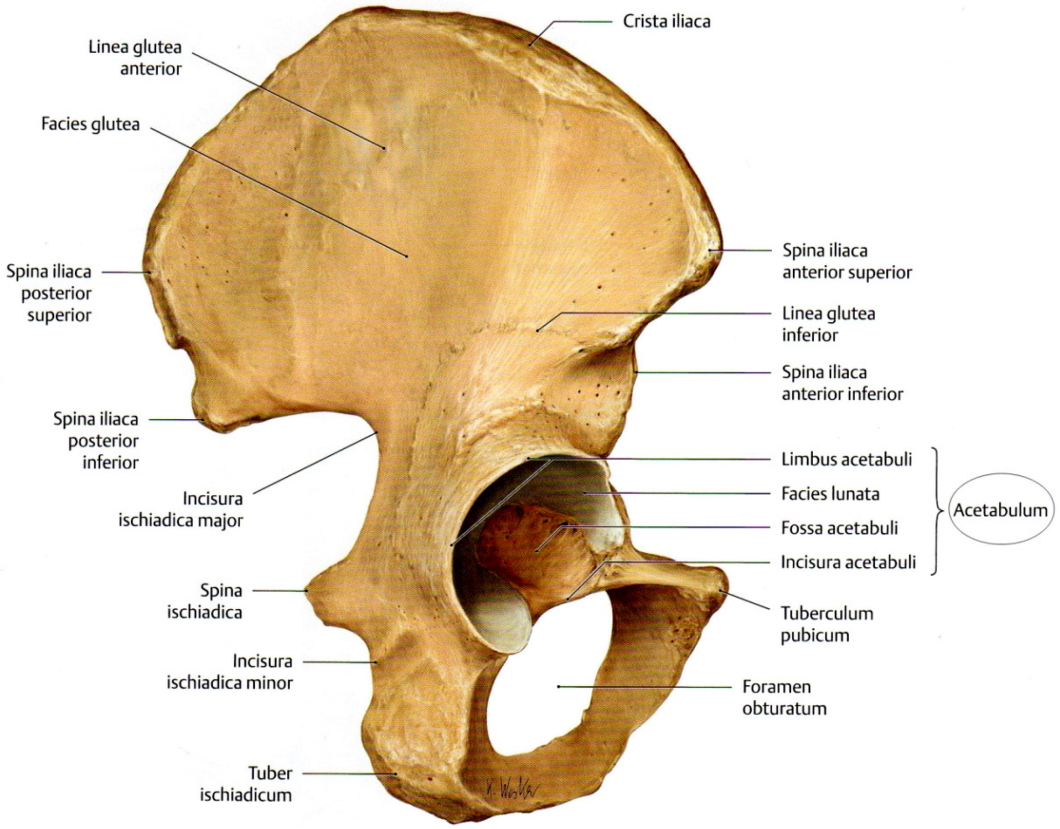


*Figure 2.3: Right pelvis, right lateral view [4]*

Between bones that form the hip joint, there are soft tissues that protect the contact surfaces of the bones and facilitate the smooth, pain-free operation of the joint(Figure 2.4). These include:

- **Articular cartilage**, which covers the surface of the femur head and the interior of the acetabulum. It absorbs shocks and provides a slick surface which allows low-friction sliding between the bones joints [6].
- The **acetabular labrum**, is a ring of cartilage which follows the acetabular rim around the femur. It's primary functions are to artificially deepen the acetabulum, act as a seal which keeps lubricant fluid between the femur-head/acetabulum and makes it more difficult for the femur-head to slip-out (sublux) of the joint. [7]

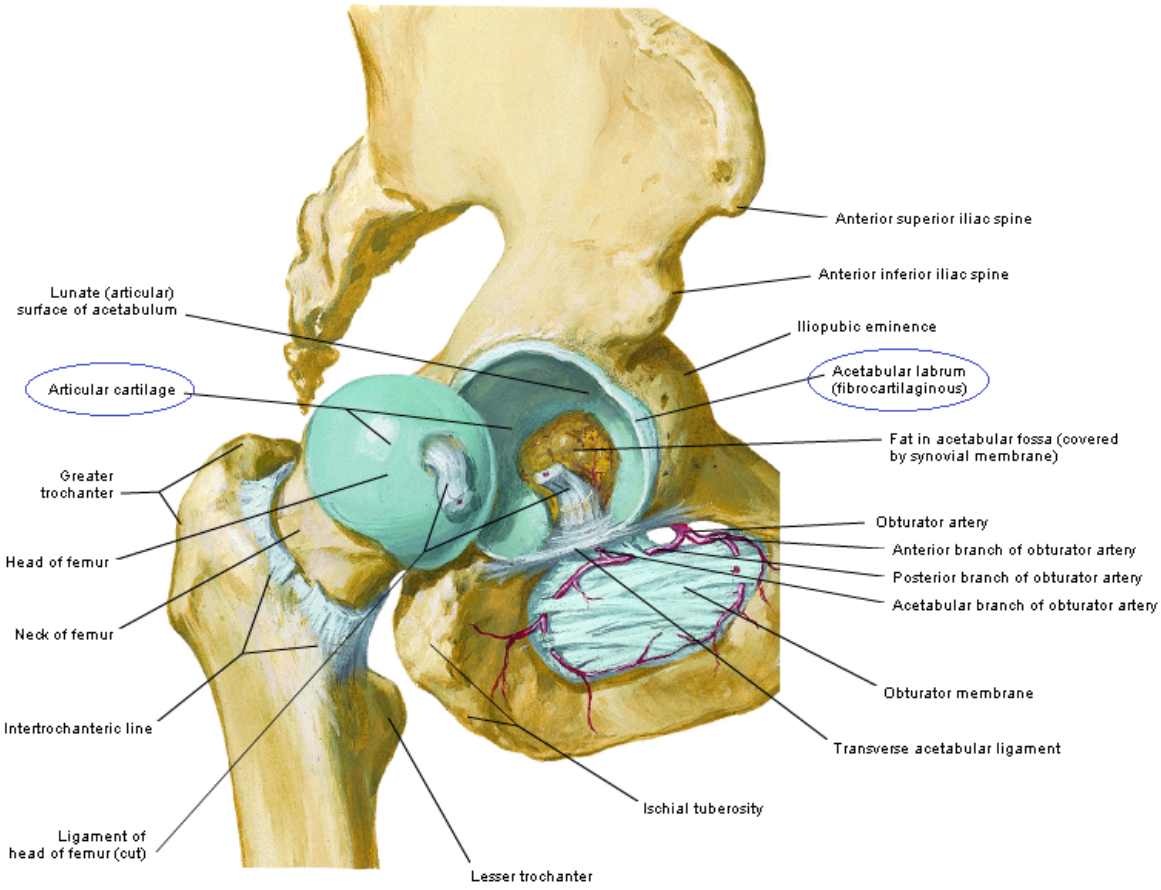


*Figure 2.4: Opened view of the hip joint [8]*

The internal structure of the bones is primarily composed of osseous tissue interspersed with bone marrow. Osseous tissue is characterized as being either *spongy* or *compact* while bone marrow comes in a *red* or *yellow* variety. [9] [10]

- **Compact bone**, synonymous with **cortical** bone, is the dense and strong bone cell arrangement which forms the outer shell of most bones. These cells provide the functions most often associated with bones, such as supporting the body's weight and protecting organs. Compact bone forms the thick tube-like walls of long bones (the shaft) which surround the medullary cavity (see Figure 2.5). A thin layer also covers the epiphyses of long bones.
- **Spongy bone**, synonymous with **cancellous** or **trabecular** bone, consists of a meshwork of interconnecting sections of bone called *trabeculae* which create a sponge-like appearance. This type of bone is found at the ends of long bones and at the center of all other bones. Trabeculae give strength to bones without the added weight of being solid like compact bones.
- **Red marrow** fills the many pockets inside of spongy bone. It is primarily composed of hematopoietic tissue (tissue which creates new red & white-blood cells).
- **Yellow marrow** fills the medullary cavities of long bones. It is primarily composed of fat cells which can be converted into red marrow when it becomes depleted.

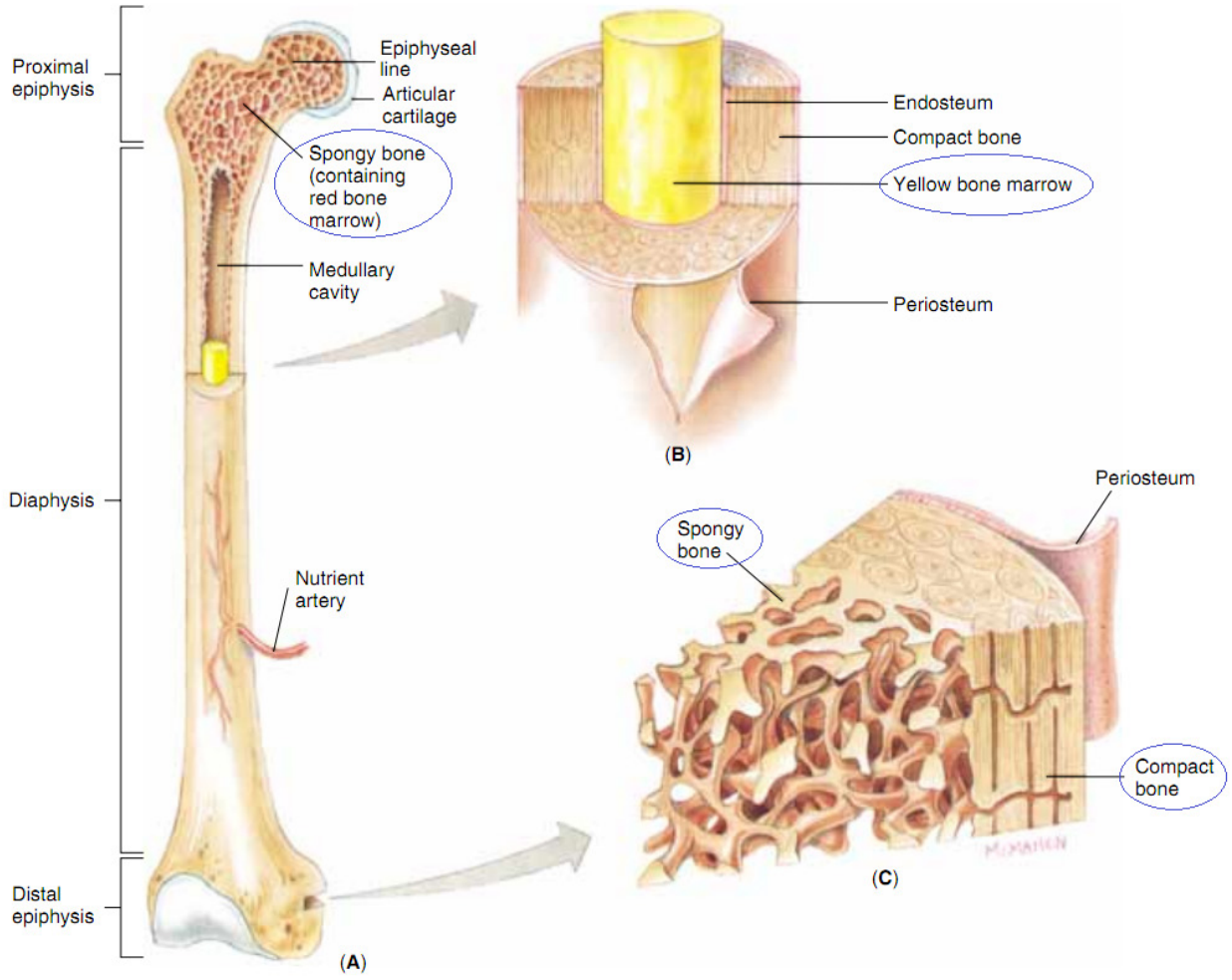


*Figure 2.5: Typical structure of a long bone (a) Diaphysis, epiphysis and medullary cavity (b) compact bone surrounding the yellow bone marrow in the medullary cavity (c) spongy bone and compact bone in the epiphysis [9]*

## 2.1.2 Function

The hip-joint's task in the human body is to support upper-body weight- both while standing still and during movement.

Hip movement is enabled by the hip functioning as a ball-and-socket [11]. This type of joint(Figure 2.6(a)) affords the hip three rotational Degrees Of Freedom (DOF), while other joints, like the one used in the knee (Figure 2.6(b)) only afford one DOF.

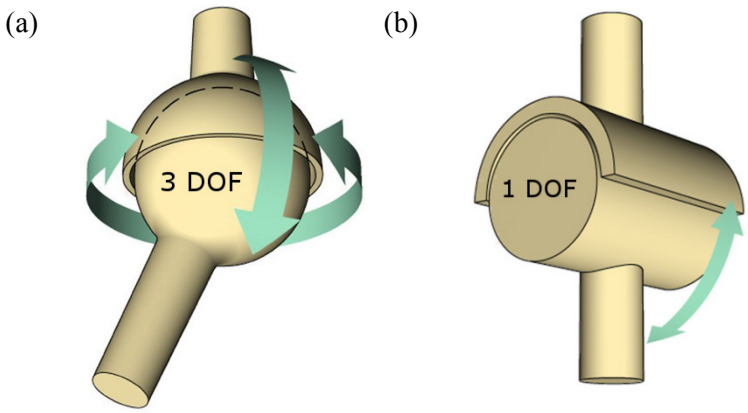


*Figure 2.6: (a) Ball-and-socket joint [12] (b) Hinge joint [13]*

These three DOF do not have full rotation in the human hip and are constrained to certain Range Of Motion (ROM). This ROM refers to the maximum distance (in degrees) the femur can rotate from a neutral position (Table 2.1). In total, there are six base types of movements which the hip-joint permits (each with their own range of motion), which can be classified according to the anatomical plane their motions parallel:

a. Sagital plane – **Flexion** and **Extension** (Figure 2.7 a)

b. Corronal plane – **Abduction** and **Adduction** (Figure 2.7 b)

c. Transverse plane – **Lateral rotation** and **Medial rotation** (Figure 2.7 b)

*Table 2.1: Normal values for the Range of Motion of hip-joints [14]*

| **Motion** | **Range (°)** |
|---|---|
| Flexion | 0-125 |
| Extension | 115-0 |
| Hyperextension | 0-15 |
| Abduction | 0-45 |
| Adduction | 45-0 |
| Lateral rotation | 0-45 |
| Medial rotation | 0-45 |

(a) (b)

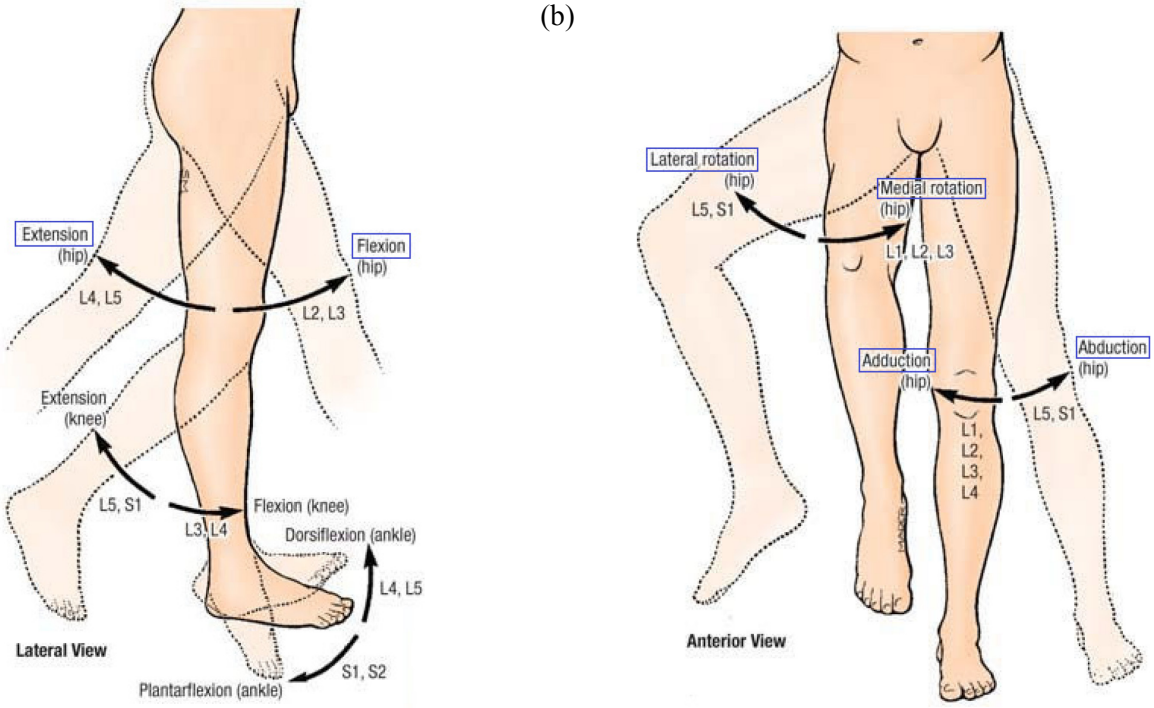


*Figure 2.7: (a) Anterior rotations of the hip (b) Lateral rotation of the hip [5]*

## 2.2 Femoral Acetabular Impingement

### 2.2.1 What is F.A.I?

Hip impingement, or *Femoral-Acetabular Impingment* (FAI), is a pathological condition where there is a deformity on either of the hip joint's bones [7] [15]. This deformity usually manifests itself as a bony-bump on the acetabular rim or the femur's head-neck junction (or both.) As a result, the hip joint will lose its ideal ball-and-socket shape which causes abnormal contact (impingement) between the femur and acetabulum during normal hip-rotation. In turn, this abnormal contact causes chaffing of the soft-tissue protecting the two bones which over time deteriorates the integrity of the joint.

### 2.2.2 Symptoms

FAI is most often associated with pain during hip flexion, adduction, and the internal rotation of the femur [16]. If left untreated, a FAI can lead to cartilage damage, labral tears, early hip arthritis, hyperlaxity, sports hernias and chronic lower back pain.

### 2.2.3 Types of F.A.I

*Table 2.2: (left) Normal bone configuration of the hip joint with sufficient joint clearance (center) Cam impingement due to aspherical head-neck junction which collides with the acetabulum (right) Pincer impingement due to excessive acetabular over-coverage [17]*

| Normal | Cam | Pincer |
|---|---|---|
| 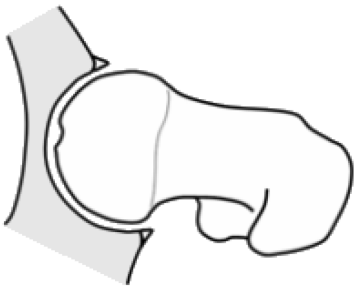 | 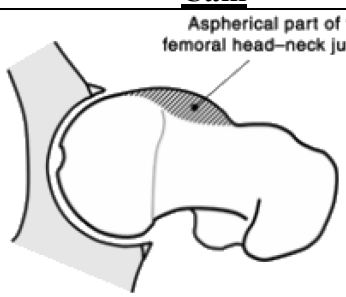 | 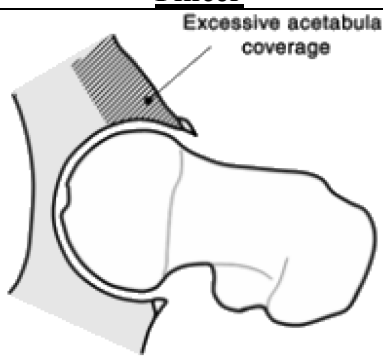 |
| 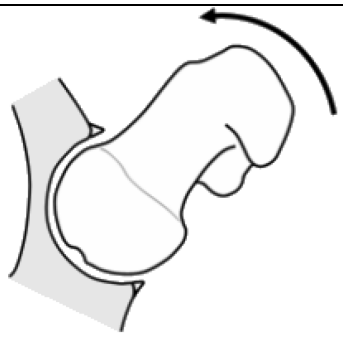 | 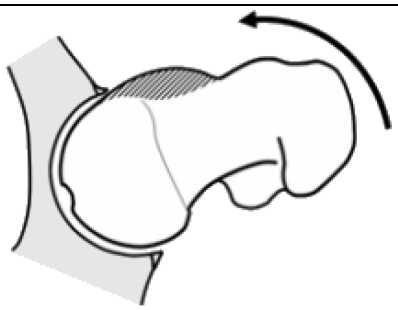 | 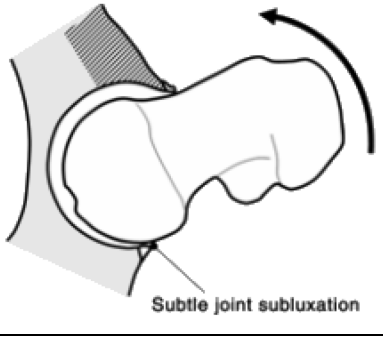 |

FAIs come in two varieties:

**Cam impingements** describe the case when the deformity causes a loss of sphericity for the femur head. In this case, the bony bump is usually located at the head neck-junction of the femur, which further reduces the head-neck offset. Chaffing at the deformity causes cartilage injury, especially during forced flexion and internal rotation.

**Pincer impingements** describe the case when the acetabulum has *too much* coverage of the femur head. In this case, the bony bump exists on the acetabular rim, which prematurely intercepts the femur at the neck. The labrum ends up being pinched between the two bones and forcing the flexion can cause the subluxation (small dislocation) of the femur head away from its normal center of rotation.

### 2.2.4 Surgical Correction

There are three categories [15] of surgical techniques used for the treatment of FAIS:

1. A fully open surgical procedure in which the femoral head is dislocated, providing full access for the correction of cam impingement as well as trimming of the acetabular rim as needed.
2. An arthroscopic technique, where the whole surgery is done arthroscopically or in conjunction with an arthrotomy (incision into the joint). No dislocation is needed in this case.
3. A periacetabular osteotomy (bone-cutting) performed for certain forms of pincer type impingements.

### 2.2.5 Prevalence

The prevalence of FAIs is not very well understood and variant dependant on the population. Some estimates set the prevalence levels of FAI between 10-15% [18] [19].

However, it is thought to be most prevalent in physical active young adults. One examination reported that 94% of the hip from 34 athletes who presented with "long-standing adductor-related groin pain" showed signs of FAIs in radiographs [20].

One study [3] examined 157 young patients (aged 18-50 years, means age 32 years) who presented with hip-related complaints. The study reported that 87% of the patients had at least one radiograph that showed sign of FAI.

Another study from Japan [21] examined 817 consecutive patients who underwent primary surgery for osteoarthritis. The researchers reported that they found a few (0.6%) cases determined to be FAI positive by looking at pre-operative radiographs. Instead, they found that the majority of their osteoarthritic hips were caused by developmental dysplasia of the hip.

## 2.3 Computed Tomography

Computed Axial Tomography (shortened to CAT or just CT) is a volumetric medical imaging technique whose result is composed of multiple 2D cross-sections of the volume. The cross-sections are called *slices* (Figure 2.8) and, and in x-ray tomography, the slices are made by moving and x-ray source and film axially around a patient's body. A "CT scan" is the process of taking a number of consecutive slices of the human body and collating their results into a single voxelized (3D pixel) volume. In the case Magnetic Resonance Imaging, a similar technique is used with the substitution of x-rays with radio-frequency-waves.

During a CT scan, the gap between consecutive slices and their dimension is specified. These dimensions can range from 256x256 to 4056x4056 voxels-per-slice, but 512x512 voxels-per-slice is common with medical CT scanner. Higher resolutions than this require higher radiation levels to be used which may present an unacceptable health risk to the patient being scanned.

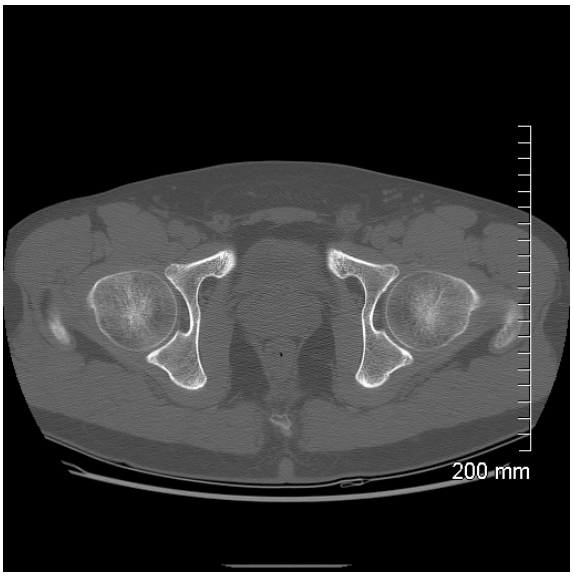


*Figure 2.8: Single slice from a CT scan crossing a patient's femur head*

The base unit of the CT scan is a voxel which may not necessarily be cubic. A voxel's dimensions dictated by the following correspondence:

- Length = Physical length of the scanning area／ horizontal resolution of the slice
- Width = Physical length width of the scanning area／ vertical resolution of the slice
- Depth = Spacing between the position of the last slice and the current one

Each voxel also has an associated *Hounsfield Unit* (HU). These units are a measure of x-ray attenuation while traversing through a substance. The *Hounsfield scale* starts at -1000HU (attenuation of air) centers a 0HU (attenuation of water) and ends at +1000HU (densest bone)

*Table 2.3: The Hounsfield Scale of CT numbers [22]*

| **Substance** | **Hounsfield Unit Range** |
|---|---|
| Air | -1000 |
| Lung | [-400, -600] |
| Fat | [-60, -100] |
| Water | 0 |
| Soft Tissue | [+40, +80] |
| Bone | [+400, +1000] |

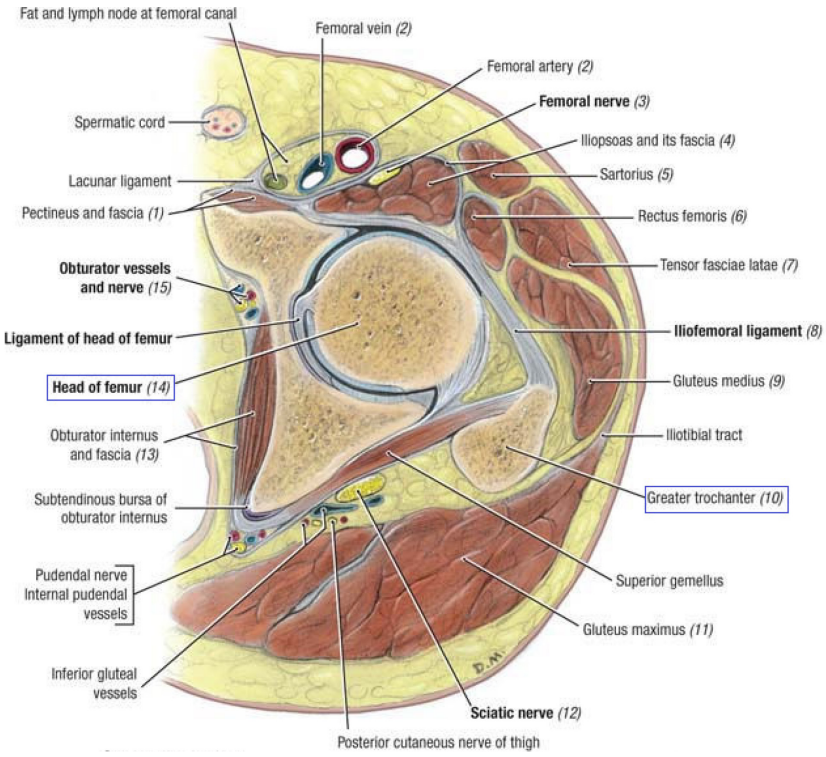


*Figure 2.9: Transverse Section of the Hip Joint [5]*

## 2.4 Current Medical Segmentation Methods

### 2.4.1 Manual Segmentation

Regarding the segmentation of medical data, the golden standard against which all other methods are compared is manual segmentation. This refers the case where a medical professional labels each voxel individually as belonging to an object of interest or belonging to the background. This provides the highest accuracy out of any scheme and is usually performed by a radiologist, in the case of radiographs of CT scans.

That being said, the manual segmentation process is still subject to inaccuracies(1-2 voxels error [23]) due to the scaled-down resolution and blurry details sometimes present in medical

images. For the highest possible accuracy, it is sometimes necessary to have multiple radiologists manually segment the same medical images in order to be able to reach a consensus.

Unfortunately, this method is also the most time-consuming, especially in the case of 3D volumes. So much so, that it becomes a deterrent to creating patient-specific models of organs and bones for pre-operative planning.

### 2.4.2 Energy Minimizing Curves

This section covers early efforts to move a curve from its starting locating in an image nearer to pertinent image features, such as gradients.

In 1987, Kass et al. introduced *Active Contours Models* (ACMs) [24]; a new framework for finding prominent image contours. The initial idea was to use energy-minimizing splines that would be influenced by image forces and attracted to such features as edges, lines and line endpoints. However, their implementation required the initial contour to be quite close to the region of interest in order to capture that contour accurately. In addition, this implementation was also designed to be user interactive; relying on human intervention to exert artificial forces on the spline in order help it escape from local minima. In fact, the first ACMs were designed to be more of a "power assist" for image interpretation than an automated image segmentation scheme. Kass also gave ACMs the popular designation of "Snakes" because of "the way the contours slither while minimizing their energy".

In 1989, Cohen detailed a number of improvements [25] to Kass' active contour models. The first few of these improvements targeted the instability of the curve evolution due to image forces. Cohen improved the curve evolution by optimizing the elasticity and rigidity coefficients of the active contours, normalising the image force in order to address the time discretization problem and using bilinear interpolation of the image forces at non-integer positions to address

the space discretization problem. In addition, Cohen introduces a way to integrate locally detected edge information (such as edges found through Canny edge detection) into the snakes normal curve evolution. However, the most influential of Cohen's improvements was the "Balloon Model". While previously, the initial contour needed to be close enough to an edge in order to be attracted to it, Cohen's model adds an additional constant force to curve evolution which has the effect of "inflating" the initial contour like a balloon. The sign of this force can also be reversed in order to reproduce a "deflating" effect. The pressures from these constant forces are used to bypass weak edges (corresponding to local minima) but still be attracted to and stop at sufficiently strong edges.

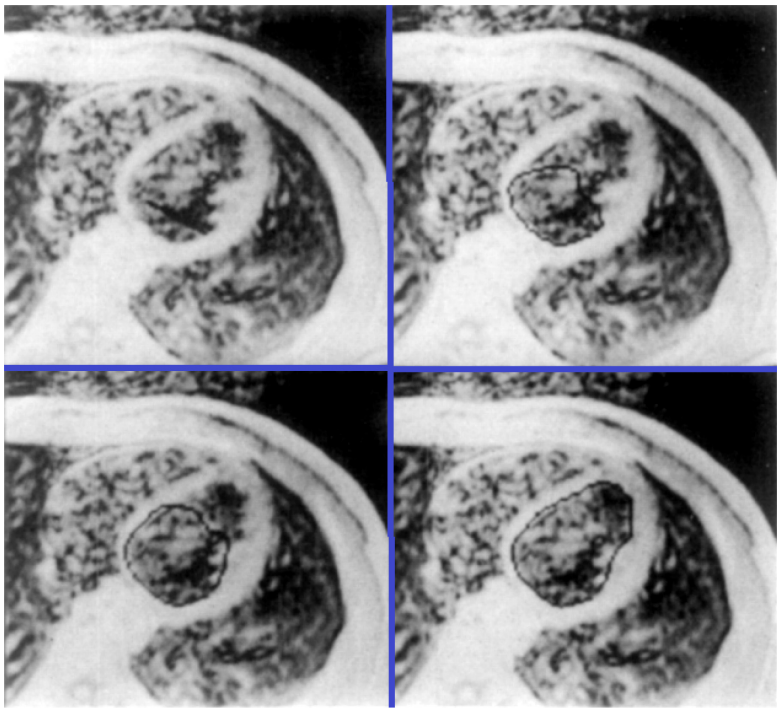

*Figure 2.10: Evolution of the balloon curve as it inflates to detect the contour of the left heart ventricle [25]*

In 1991, Cohen & Cohen returned with further improvements [26] to the balloon model. Previously, snakes were adapted to for use in 3D segmentations by dividing the problem into a set of successive 2D curve evolutions. Cohen & Cohen introduced a 3D generalisation of their

balloon model as well as a simplification of it which divided the problem into a set of simultaneous 2D curve evolutions. This simplification proved faster than its successive counterpart and the interaction between neighbouring slices allowed the model to recover from missing edge segments. In addition to this, the algorithm uses a Finite Element Method (instead of the original Finite Difference Method) which reduced to algorithmic complexity and produced more accurate results.

In 1996, Xu and Prince sought to fix two of snake's native shortcomings with a single solution [27]. The first shortcoming being the classical active contour model's limited *capture range* (previously addressed through balloon snake's pressure force) and the second being an active contour's difficulty evolving into boundary concavities. Xu and Prince resolved these by introducing a new irrotational & solenoidal external force model, called *Gradient Vector Flow* (GVF). GVF is a static vector field calculated from the diffusion of the gradient vectors of grayscale or binary edge-map. The resulting GVF snake is relatively insensitive to staring positions, does not need to be told to inflate or deflate in order to capture a contour at a distance and evolves into concavities without risking overwhelming weaker contour edges.

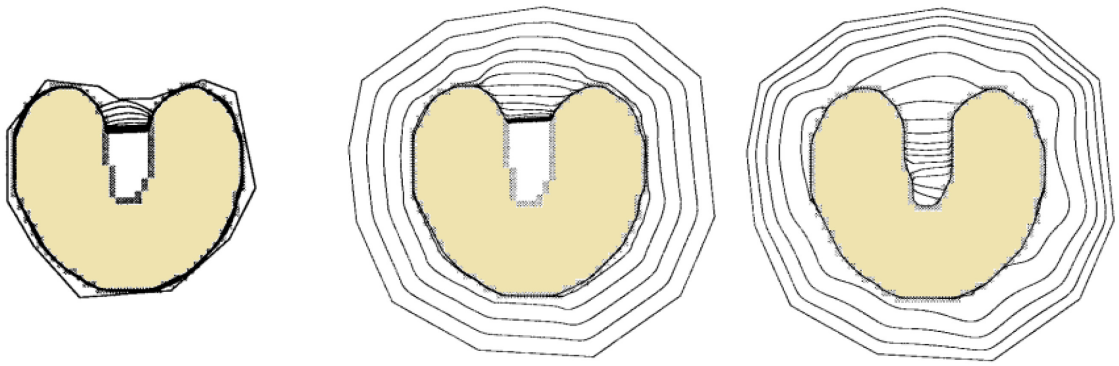

*Figure 2.11: Convergence of a snake using (left) traditional potential forces (middle) distance potential forces (right) GVF external forces [27]*

In 1998, McInerney & Terzopoulos compensated for the topological inflexibility of snakes by adapting [28] the balloon snake's deformation phase to exploit affine cell decomposition. Their method decomposes the image space into triangular cells which are used to approximate the active contour. Triangles are evaluated as being inside, outside or intersecting the active contour, allowing the contour topology to be checked quickly during deformations. Crossing contours signify the need to split a single contour into two independent snakes or to merge two independent contours into a single snake.

### 2.4.3 Level Set Based

This sections covers level set methods, which could be described as the successors to the original snake methods. Unlike snakes, these new methods are less curvature based and more contour based, producing closed loops around objects.

In 1993, Malladi et al. sough to present a new shape modeling scheme [29] that retained some of the desirable features of popular shape modeling methods (like snakes) while overcoming some of their deficiencies (difficulty with topological changes, long protrusions and complex shapes; sensitivity to shape initialisation). The new method is based on the idea to represent the evolving curve(s) as the zero level-set of a higher dimensional function. In order to accomplish segmentation, an initial, closed, nonintersecting hypersurface is placed in the image space. The hypersurface then propagates along its normal direction with a velocity based on the hypersuface's curvature. Whether the front sticks to an object's boundaries or not is decided by a halting criterion obtained by synthesising a velocity term from image data. Malladi et al. also introduced a number of extensions to their level-set method, such as the *narrow-band* extension which speeds up front propagation by only updating the level-set function at points within a specified neighbourhood around the front.

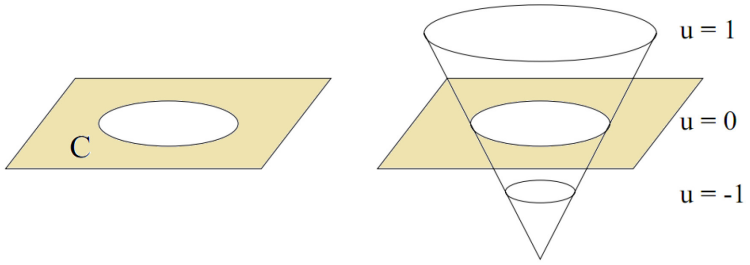


*Figure 2.12: Level sets of an embedding functions u for a closed curve C in $R^2$ [30]*

In 1994, Caselles et al. introduced a new level set method called the *geodesic active contour model* [31]. The aim of their paper was to prove that a particular case of the classical energy snakes model is equivalent to finding a geodesic curve in a Riemannian space using a metric derived from the image content. After assuming that the geodesic active contour is represented as the zero level set of a 3D function, the geodesic curve computation was reduced to a geometric flow. This flow is comparable to the evolution approach introduced by Malladi et al in 1993. In addition to this, Caselle's new model introduced a new component to the velocity term (synthesised from image data) which permits better tracking of boundaries where large variations in the gradient or gaps exist.

In 1997, Siddiqi et al. modified [32] the geodesic active contour method by replacing the constant inflation force with a new term obtained from minimizing a weighted area energy functional. This modification was shown to strengthen the evolving contour's attraction to features of interest, like edges, and increased the speed at which the deformable contours converged to the desired boundaries. Saddiqi et al. also showed that in some image segmentation experiments, the *weighted length* minimization flow (from the original geodesic method) can be dismissed completely in favour of the newly introduced *weighted area* minimization flow. This offers significant computational savings since the weighted area minimization flow only uses first order derivatives.

In 1999, Chan and Vese proposed a different type active contour model [33] [34], one that does not rely on the image gradient information to provide a stopping process for curve evolution. Instead of minimizing the energy of a curve functional, the new model attempts to minimize the energy inside of the curve(s), making it region-based rather than boundary-based. This allows Chan & Vese's method to detect objects that are not defined by gradients or have very smooth gradients. Experimental examples of these included segmenting textures with different densities, shapes or orientations. In addition to this, the initial curve can be anywhere in the image and the method automatically detects interior contours (holes) in objects of interest.

In 2001, Wang et al. proposed [35] a new framework that integrated region information into existing boundary-based deformable contour methods. This was accomplished by adding the homogeneity of the curve interior as an extra constraint within the energy minimization framework. The described approach uses an evolutionary/genetic method (favouring mutations with the lowest evolving contour energy) on a level set while using the fast marching method [36]. Since region information is more global and less susceptible to noise than boundary based methods, this method returns much more robust and precise results in complex images, like medical scans [37].

In 2010, Álvarez et al. described a modification to Geodesic Active Contours called *Morphological Snakes* [37]. The authors observed that the solution to the differential operators used in the Partial Differential Equations (PDE) of the snakes evolution model can be approximated using morphological operators, specifically, the *inf* (infimum) and *sup* (supremum) operators. The advantages from this modification are that curve evolution is faster (and simpler to implement), morphological snakes do not suffer from instability and the embedding function

does not require re-initialisation. As this method is the driving force behind our contour extractions, a more in-depth description is given in Section 3.4 .

### 2.4.4 Model Based

Model based segmentation methods are intended to segment objects which follow known patterns. By balancing model information and image information, they are sometime able to overcome weak or missing image information, such a edges.

In 1992, Cootes et al. described Point Distribution Models (PDMs) [38], a statistical model for shapes constructed from training sets of image landmarks. PDMs represent objects as a set of labeled points, the mean positions of which provide and average shape. Afterward the means modes of variation of the points are determined in order to describe the main ways in which the landmarks tend to deform from the average.

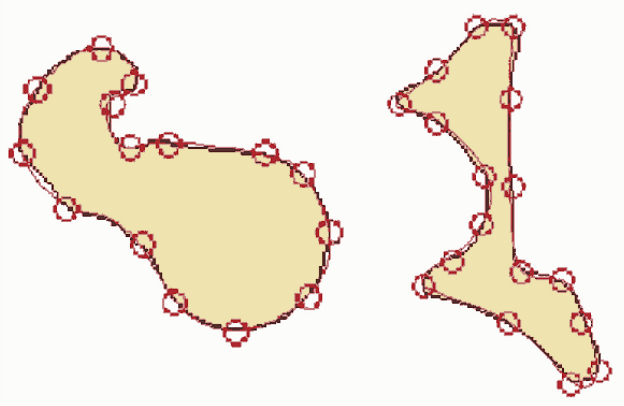

*Figure 2.13: Two examples of image landmarks which can be used to construct a PDM [39]*

In 1992, Cootes et al. introduced a new segmentation Method called Active Shape Models (ASMs) [40]. The main idea behind ASM is to locate within an image a desired object by iteratively deforming its corresponding PDM. Using PDMs in this case constricts the model to only deforming in ways seen in the training set. The constrained flexibility of PDMs allows ASMs to capture objects which do not have identical shapes (an advantage over rigid

registrations methods) and prevents the model from deforming into invalid object shapes (an advantage over standard Snake & level set methods) while still being robust against image clutter or object occlusion.

In 1998, Cootes et al. introduced Active Appearance Models [41]; an extension to ASMs which added a statistical appearance model [42]. This new approach sought to use the modeling information of not only the variations in the object's shape (as with PDMs) but also the variations in the grey-level appearance of the object's interior. A statistical model of an object's appearance is created by warping each training image so that its landmarks correspond to those from the PDM's average shape. Afterwards, PCA is performed on the normalized data to provide an average appearance model along with its mean modes of variation. Once an object of interest has both a statistical shape and appearance model, its location in an image can be found by minimizing the difference between the image and the synthesized ASM model. This step is implemented through a multi-resolution, least squares technique. While AAMs are slower to converge than ASMs, the authors argue that the additional robustness introduced by using more image evidence makes up for the difference.

In 2000, Leventon et al. proposed [30] a statistical framework for incorporating prior shape knowledge into the geodesic active contour method. The prior shape model in this case is created by performing PCA on the signed distance maps of the training set objects. At each step of the curve evolution, the force applied to the curve is modified to include a shape-force parameter. This parameter is calculated from the maximum *a posteriori* estimated position and shape of the curve.

In 2000, Cremers et al. first introduced Diffusion Snakes [43] [44] [45]: a region-based segmentation scheme that makes use of prior shape knowledge. Specifically, the authors modify

the Mumford-Shah energy functional so as to integrate shape energy based on a Gaussian approximation of the shape distribution.

In 2001, Y. Chen et al. [46] proposed a variational framework for incorporating prior shape knowledge into an active contour. The key idea was to introduce an energy term which measures the closeness of an active contour to the training set's average curve in a way that is independent of the location, orientation or scale of the active contour. The authors also prove the existence of minimum of the energy functional used if this framework. This segmentation model differentiates itself from Leventon's by using a variational approach instead of a probabilistic one.

In 2004, Cremers et al. proposed solutions [47] to problems associated with statistical prior shape information for level set schemes. In their paper, they claimed two major contributions. The first of these was representing (through Kernel Density Estimation [48]) and integrating (through Bayesian Inference) the statistical shape priors into level set segmentation methods for arbitrary shape distributions. This addressed the limitation of previous approaches where all detected objects needed to follow a Gaussian distribution constructed from shape priors. The paper's second contribution is a scheme to introduce translation & scaling invariance to shape priors through an intrinsic registration of the evolving level set function. This removed the need to numerically and iteratively optimize a set of explicit pose parameters for the shape priors at each step.

In 2009, S. Chen and Radke expanded [49] upon Cremers' shape prior segmentation scheme by including intensity priors. This is achieved by including both a shape and an image energy parameter to the Bayesian formulation, with the image energy also being represented through the Kernel Density Estimation of the training samples. In this case, image energy is based on the

regional intensity distribution of training samples, expressed as normalizes histogram of an object's interior. The authors argued that the inclusion of intensity priors to the level set evolution process allows their solution to segment objects with highly inhomogeneous interiors and/or weak boundaries.

## 2.5 Hip Segmentation Methods from CT/MRI

The following segmentation methods are the precursors to our research. Many of these approaches attempt to segment the acetabulum along with the femur.

In 1999, Safont and Marroquin made one of the first attempts [50] at model-based segmentation and reconstruction femurs from CAT images. Their primary challenge was to segment the femur from slices where there was little to no contrast between the femur head and acetabulum. To accomplish this, a model was built of standard femur composed of six "key-frames" which spanned from the top of the femur head to the top of the femur body. These key-frames were initially placed on the CAT scan using semi-automatically based on the inertia moments of high gradient points around the femur head. Intermediate slices which aren't overlaid with key-frames have their initial contour determined through the linear combination of the nearest key-frames. Afterwards, the slice is thresholded to highlight the bones and a new contour is obtained after looking for binary edges in the normal direction to the contour's control points. The final contour for each slice is decided on a point-to-point basis, favouring the initial contour's control points over those from the new contour when the distance between corresponding points in the two contours grows too large.

In 2001, Zoroofi et al. described a set of techniques that [51] can be used to segment the femur head and acetabulum. The first step involved assigning the CT scan of a hip into one of four groups based on features anticipated to increase the difficulty of segmentation. Hips

belonging to Group #1 had the acetabulum and femur-head well separated from each other while femurs in Group #2 & #3 had the two bones close enough to cause problems. The differentiating factor between femurs in Group #2 & #3 was that the femur heads in the former were near perfectly ellipsoidal while those in the latter were not. Finally, femurs in group #4 were observed to suffer from sever bone disease. After group classification, the femurs from group#1-#4 were resampled, smoothed with a 3D Gaussian filter, thresholded based on histogram information, had noise removed, holes filed at while point the largest 3D object was detected. While sufficient for detecting the bones in group #1, femurs from group #2-#4 require additional steps. Femurs from group #2 get their final segmentation result by using a Hough transformation to find the ellipsoid that best describes the femur head. Femurs from groups #3 & #4 get their final result by (a) Applying a Hessian filter to the CT scan (c) using a custom method called the "Moving-Disk algorithm" to refine the boundary between the femur-head and acetabulum. The authors describe the "Moving Disk algorithm" as a combination of the Hueckel-based operator and orthogonal line edge detection.

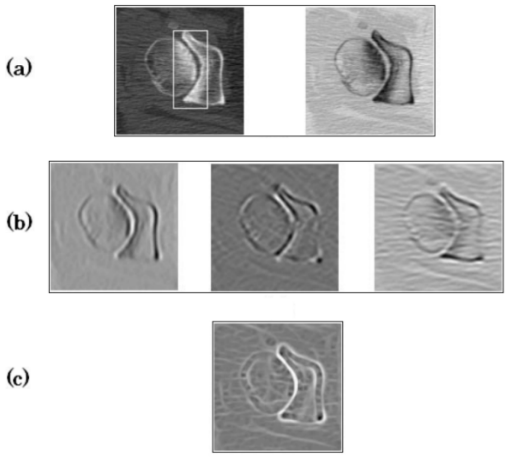


*Figure 2.14: Enhancing the joint-space by the Hessian filter (a) noisy acetabulum and femur (b)The left, middle and right images show the results of filtering the initial image in the horizontal, diagonal and vertical direction respectively (c) Results of Hessian Filtering [51]*

In 2003, Magnenat –Thalman et al, briefly described [52] how they semi-automatically segmented femurs in their MRI data. The driving force behind the segmentation was a custom-written discrete snake procedure based on Kass' model. On each MRI slice, a set of points was manually placed at 1-2 cm intervals around the femur head, which when linked together provided the initial contour for their snake procedure. The active contour method was then used make an attempt at finding the best fit to the actual boundary and manual corrections were made anytime the Snakes method failed due to fuzzy edges.

In 2006, Gilles et al. described [53] a more modern, model-based method to segmenting from MRI scans the femur, acetabulum as well as the major muscles of the thigh. In the case of the femur, four generic models were created; each corresponding to a different level of detail. The highest of these was a mesh composed of 85100 vertices. The initial placement of the femur model was determined by the thin-plate-spline interpolation of manually identified landmarks in the MRI scan. Afterwards, the generic model is deformed from the coarsest level to the finest level using multi-resolution internal forces (shape and smoothness constraints), external forces (intensity-profile based) and non-penetration constraints (collisions handling between bones).

In 2007, Song et al. proposed a new method [39] to segment the femur head and acetabulum from CT datasets of the hip joint using an ASM for each bone. Specifically, the authors describe a method to segment the cross-sections of the femur or acetabulur for single slices in a CT volume. These cross sections do not include the entirety of the pelvic bones but range from the top of the femur head to the bottom of the greater trochanter. In addition to the ASMs, the authors also construct grey-level appearance models of the shape interiors adopted from Cootes and Taylor. After initial placement of the femur, this method iterates across a multi-resolution

framework in an attempt to find the beat translation, rotation, scale and shape mode parameters. Figure 2.15 illustrates this process.

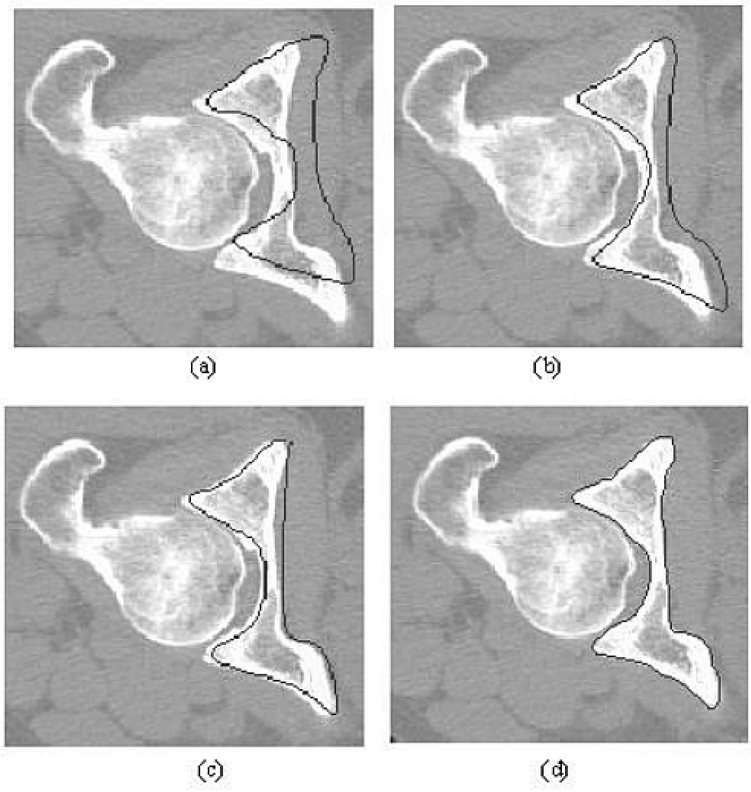


*Figure 2.15: Examples of segmentation using ASM of acetabulum on CT slice of hip-joint. (a) Initialisation (b) after two iterations (c) after size iteration (d) after twelve iterations [39]*

In 2008, Schmid & Magnenat-Thalmann, proposed [54] a method to segment the bones from MRI datasets using deformable models and shape priors. Their method uses Principle Component Analysis to define global shape variations and Markov Random Field for local deformations. The researchers reported a mean accuracy of 1.44 ± 1.1mm and computation time of 2 min and 43 seconds.

In 2009, Yokota et al. described [55] their method to segment the pelvic bones from hips suffering from osteoarthritis using a hierarchical statistical shape model. The top-most level of the hierarchical SSM combined both the pose and shape variations of the two pelvic bones. The

hierarchy is then decomposed into a combine model for the femur and acetabulum as well as two individual models for the two bones. The researchers reported an average segmentation accuracy of 1.20mm for the whole hip shape and 1.78mm for sections near the joint space.

In 2011, Schmid et al. experimented [56] with the segmentation of the pelvic bones from MRI datasets whose acquisition was accelerated through lowered resolutions or limited Fields Of View (FOV). Accurate segmentation of bones taken under low fields of view presents an additional challenge as some important bone landmarks are cropped out. This is particularly true of model-based methods, so a new, multi-resolution deformable model based on a robust SSM algorithm was proposed to handle incomplete or corrupted image sources. Using high resolution, low field of view datasets, the researchers reported an average distance error of 1.21 ± 0.53 mm for segmented femurs.

# Chapter 3 - Methodology Overview

## 3.1 Objective

We wish to segment femurs from CT datasets of human pelvises. The final segmentations of these femurs will be used to create patient-specific 3D model. Our segmentation strategy must be sufficiently accurate, robust and quick so as to be useful in (a) medical environments for the diagnosis and pre-operative planning for surgical correction of FAIs (b) simulation environments for the kinematic modeling of hip motion.

## 3.2 Complications

Several factors complicate any attempt to segment a femur from a CT pelvic scan. These complications can be classified as either a technical limitation associated with CT imagery, a patient-specific complication, or a complication associated segmentation schemes themselves.

### 3.2.1 Technical limitations of CT scans

The highest spatial resolutions attainable by CT machines require doses of radiation that present health risks which are too high to be used on living subjects. Such doses are reserved for examining cadavers, however since we wish to have our method used to treat otherwise healthy patients, we must anticipate the use of scaled-back doses. Safer radiation doses result in CT slices with *lower resolution* which end up producing voxels whose length and width give the CT scan a "blocky" appearance when viewed at full scale. In addition, the space between consecutive slices, which accounts for voxel depth, is often much larger than a voxel's length and width. This leads to the CT scan having a *low vertical resolution* due to brick-shaped voxels.

Other technical limitations include the presence of *noise* & *artefacts* being introduced by the CT's machine filter that reconstructs images from radiographic waves.

Finally, it's worth mentioning that CT machines *cannot detect the color* of the objects which they scan. If the CT scan's voxels contained colour and density information, the segmentation process would be greatly facilitated.

### 3.2.2 Patient-specific complications

Unlike segmenting objects whose potential shapes differ very little; many differences can exist between the femurs of multiple patients. These need to be considered when attempting an automatic or semi-automatic segmentation.

Some variations in human morphology need to be considered in order to form a robust segmentation solution. Common variations like different sized femurs across different patients require only superficial adjustments in the segmentation parameters. Other potentially extreme variations, like the caput-collum-diaphyseal (CCD) angle, which measures the angle between a femur's neck and shaft (Figure 3.1), require a segmentation strategy constructed to be able to capture more than one permutation of an object of interest.

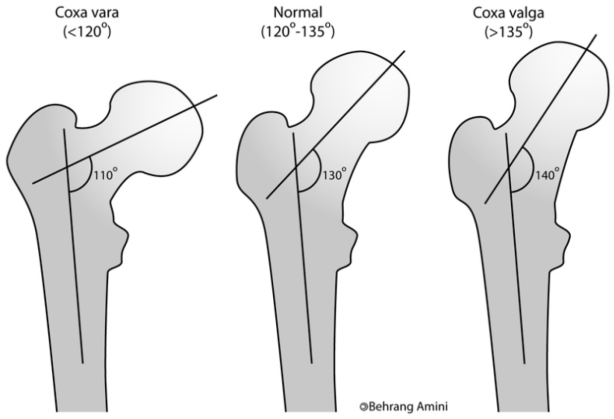


*Figure 3.1: (left) decreased CCD angle (middle) normal CCD angle (right) increased CCD angle [57]*

The *potential presence of a cam impingement* on the femur head-neck junction can deter usage of model-based segmentation schemes. The bony bump attributed to cam impingements is difficult to capture using statistical models of femurs due to its uncertain location. Incorporation FAI information into a statistical model for femurs would inflate the number of dimensions required to accurately describe the femur's shape. As a result, a larger dataset of patients would be needed in order to derive that statistical model.

Even slight variations between CT scans need to be considered when designing segmentation solutions. For example, no patient being scanned is likely to have a leg rotation and foot-spacing identical to any other patient. These subtle shifts cannot be completely eliminated and affect *femur head orientation* in the resulting CT volume.

### 3.2.3 Object segmentation complications

In addition to complication that arise from using a CT scan as input and the diversity of human morphology and scanning conditions, some of the difficulties that prove the most challenging to overcome stem directly from our object of interest.

The most immediate challenge of segmenting a femur is how to perform the *3D segmentation*. This is because most automated segmentation schemes are geared towards efficient 2D segmentation. A few of these methods have 3D extensions, but they inevitably involve additional compromises and complexity. Segmentation schemes capable of extracting 3D objects fall under two categories:

a) Those that segment the 3D object as a single process

b) Those that segment 2D subdivisions of the 3D object in multiple processes

The former has the advantages associated with the consistency of a unified approach- such as inter-slice smoothness. The latter allows the segmentation process to handle an object's subdivisions with an amount of independence when it is deemed appropriate.

Whichever segmentation scheme is chosen, the femur's *off-tubular morphology* is likely to provide additional challenges. In certain slices of a pelvic CT scan, the femur will appear as two disconnected objects (Figure 3.2). This stems from the greater trochanter having its own local crown independent of the femur head. The split occurs at the height of intertrochanteric line and the greater trochanter terminates shortly thereafter. Any femur segmentations strategies will require a mechanism or protocol which can correctly register both parts of the femur object.

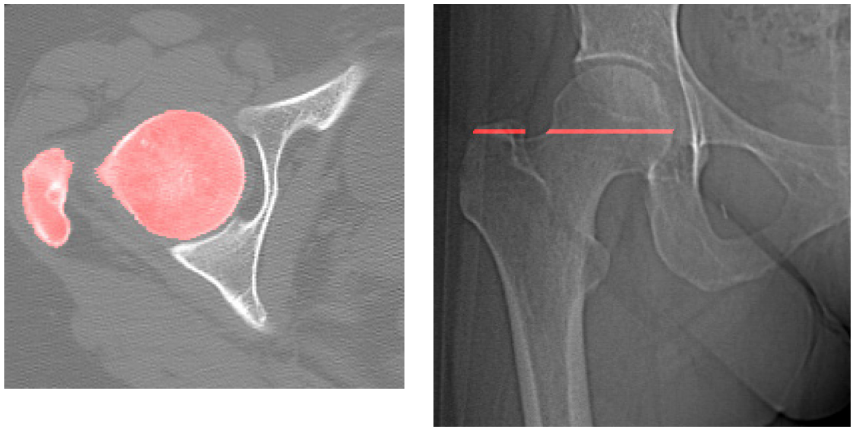

*Figure 3.2: (left) CT slice where the femur's topology consists of two disconnect objects (right) Antero-posterior view of this slice's location*

Segmentation strategies which use edge information to provide a stopping criterion for their evolving curves might prove to be the most effective at capturing the femur's contour. However, there are three factors which may cause the stopping criterion give poor results:

1. **Blurred/Thin edges** – As described earlier, large bones are composed of two different types of osseous tissue, referred to as "compact" and "spongy" bone. In CT scans, compact bone has a much higher Hounsfield unit value than spongy bone due to its density. As a result, it is much easier to use edge-based segmentation methods on compact

bone due to its high contrast with soft tissue. This compact tissue forms a protective shell of varying thickness around a bone. In the case of the femur, the compact tissue is at its thickest at the femoral shaft and at its thinnest a the epiphyses (Figure 3.3) Combined together, the thin compact bone, spongy bone full of red marrow and noisiness of the CT scan can lead to some very thin and blurred object boundaries which are difficult to detect by machine.

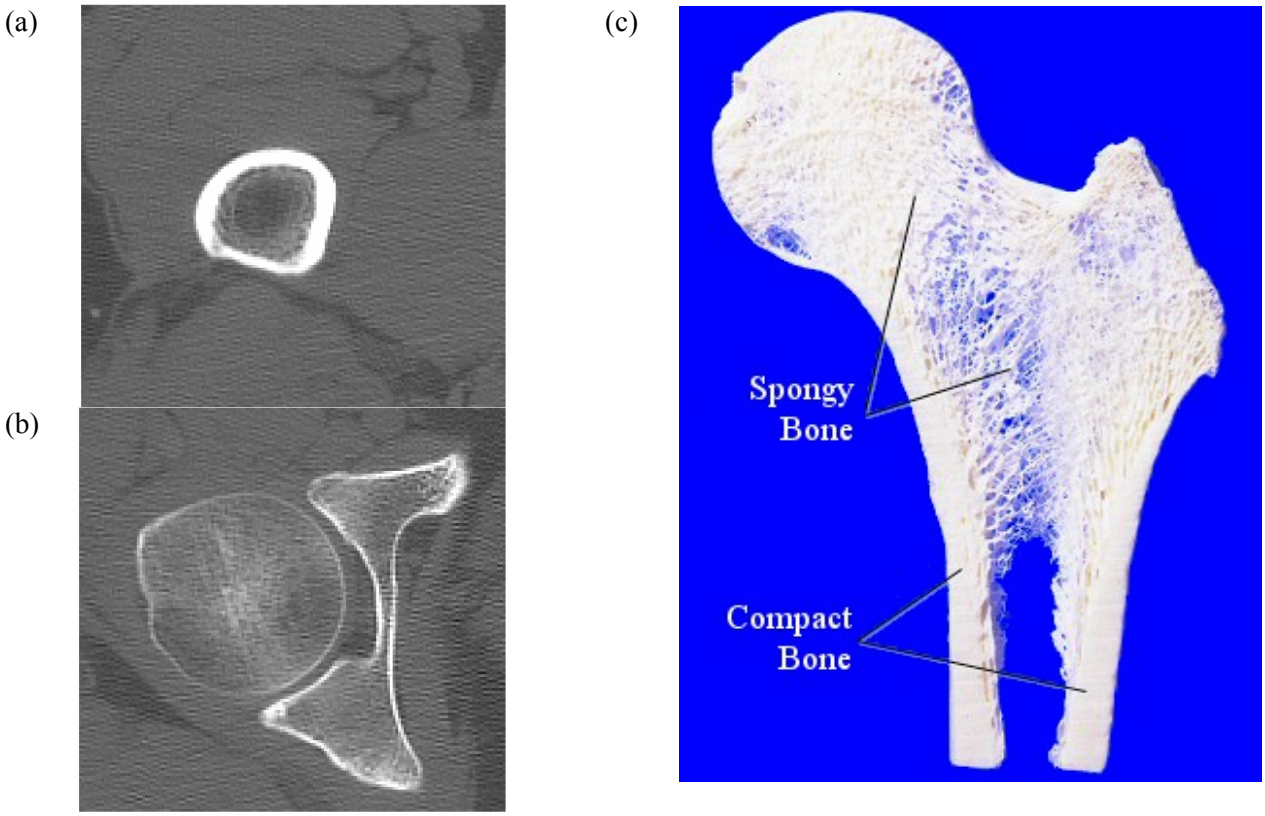


*Figure 3.3: (a) CT slice of femur shaft displaying thick compact bone shell (b) CT slice of femur head displaying thin compact bone shell (c)Cross-section of femur top that displays compact & spongy bone distribution [10]*

2. **Bone surfaces which are not orthogonal to radiation source** – Voxels containing the surface of bones are at their sharpest when that surface is orthogonal to the CT scanner's radiation source. As the bone surface becomes increasingly parallel to the radiation source, edges become more feathered in appearance and become much more susceptible

to noise. This can be seen in Figure 3.4, where the surface of the femur head (nearly parallel to the radiation source) has its edges spread over a gradient while the interior surface of the acetabulum (nearly orthogonal to the radiation source) has much clearer cut edges. This "feathered" edge effect can make it more difficult for automatic segmentation methods to capture the boundaries of the bone using gradient-based methods.

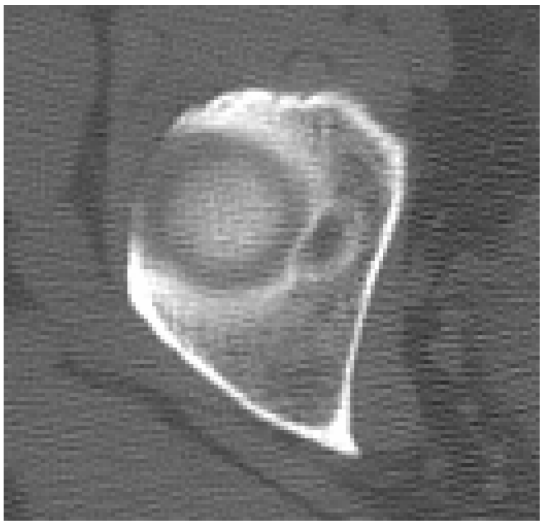

*Figure 3.4: CT slice depicting the feathered edges of the top of a femur head*

3. **Near contact regions between the femur and acetabulum** – In certain slices it may appear as though the femur and acetabulum are coming in direct contact with each other. This is usually due to a combination of slice spatial resolution and joint compression which thins the appearance of the protective soft issues in the joint. Any segmentation scheme which relies on a visible gap between the two bones would thus has difficulty separating the two objects.

## 3.3 Solution Overview

Chapter 4 covers the full details of the segmentation strategy we developed to meet our objective. A brief summary follows:

**User interaction** - We first have a user place two, 3D regions of interest: one covering the femur head and another for the femur body. Depending on the ROI, a landmark slice or voxel may also be attached.

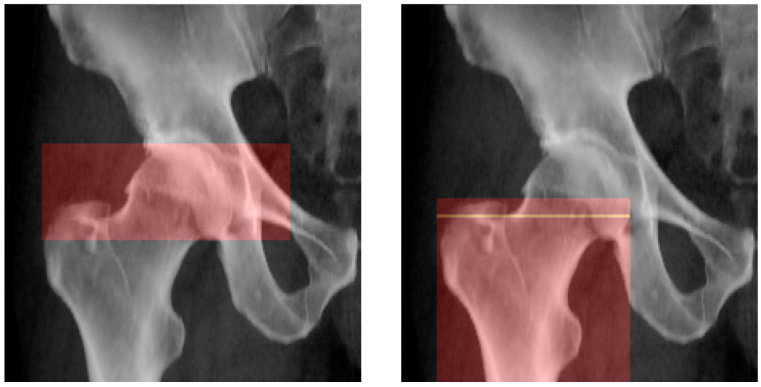

*Figure 3.5: Region of interest for the femur (left) head (right) body*

**Pre-processing –** Next, the contents of each ROI are pre-processed to highlight voxels attributed to compact bones and diminish the effect of soft tissue during the segmentation process. Afterwards, sections of the acetabular rim inside of the femur head's ROI is cut-out and replaced with a low-gradient fill to further aid the segmentation process.

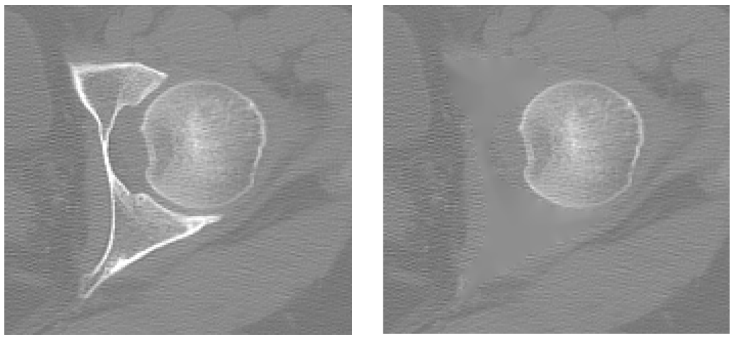

*Figure 3.6: cross-section (left) prior to the acetabular rim being cut-out (right) after the acetabular rim is cut-out and filled*

**Contour Extraction** – In order to extract 3D shapes for each of the two ROIs, a set of successive 2D segmentations is performed which are later collated to obtain a 3D model. These 2D segmentations are done on a slice-by-slice basis, where the first slice to have its contours extracted, known as a "primer slice" serves as the foothold from which the rest of the slices to be

segmented. For the ROI of the femur head, this primer slice is the middle-most slice, while for the ROI for the femur body, it is the bottom-most slice.

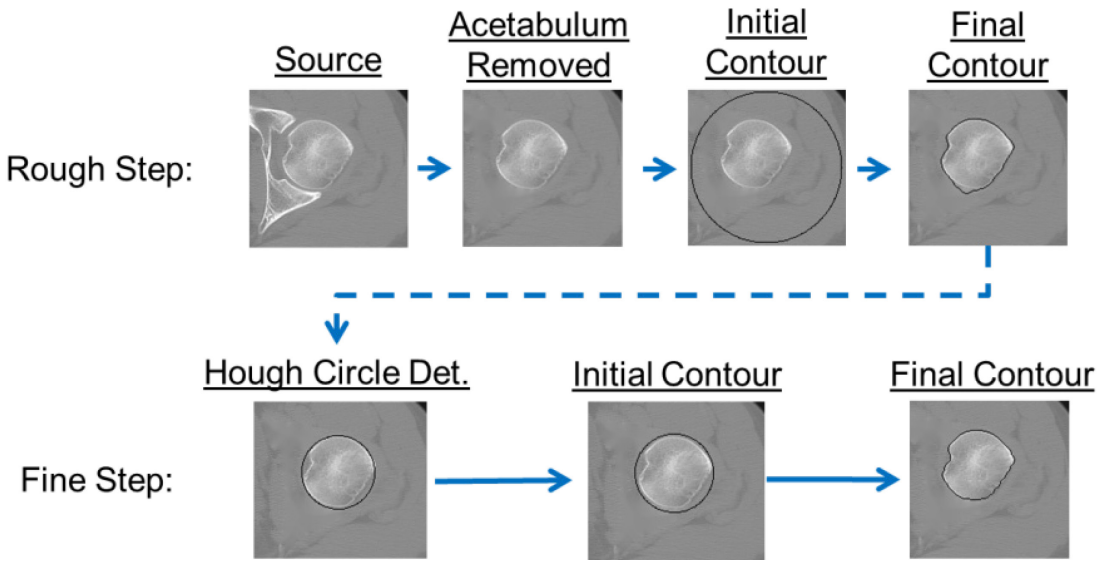


*Figure 3.7: Sample process of segmenting the primer slice of the femur head's ROI*

Both of the regions of interest are segmented using the same sequence: (a) the final contour for the primer slice is determined with two passes of the morphological snake algorithm (b) subsequent slices are segmented iteratively, outward from the primer slice, using its neighbours final contour to obtain its own initial contour.

The first pass of the primer slice's segmentation is referred to as the "rough step". This step is primarily responsible for getting the approximate location of the femur's cross-section within the ROI. The rough step is initialized with a very wide initial contour which is evolved using morphological snakes and a "rough" set of parameters to attain an intermediate contour.

The second pass of the primer slice's segmentation is referred to as the "fine step". This step is responsible for getting the first final contour in a region of interest. This step uses as input the intermediate contour obtained in the rough step to provide an initial contour which is evolved using morphological snakes and a "fine" set of parameters to attain a final contour.

Once a primer slice has been fully segmented, its neighbouring slices are segmented, followed by their neighbouring slices being segmented, and so on. This segmentation cascade is a way to establish initial contours for un-segmented slices by basing them on the final contours of their fully segmented neighbouring slices (see Figure 3.8). Here, the morphological snake algorithm is used again to evolve these initial contours into final contours, using the same set of parameters as were used for the primer slice's fine step. Once every slice in an ROI has had its contours extracted, this sequence of segmentations ends and a volumetric 3D model is obtained for the ROI's encompassing femur region.

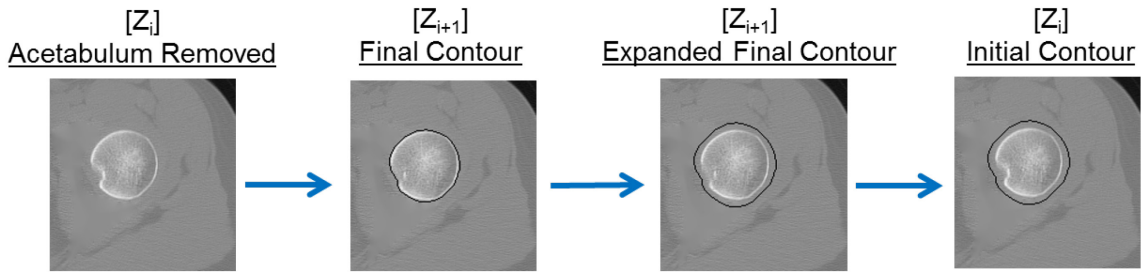


*Figure 3.8: Sample process of obtaining an initial contour for an un-segmented slice of the femur head's ROI. Here, $Z_i$ is a slice in need of an initial contour while $Z_{i+1}$ is its fully segmented neighbour*

**Post Processing** - Finally, the union of the two segmented ROIs is calculated to provide the final, patient-specific model of the femur.

## 3.4 Morphological Snakes

Morphological Snakes algorithm [58] provides the driving force behind the contour extractions for our segmentation method. This algorithm is a recent modification of Geodesic Active Contours [31] which takes a different approach to solving the PDEs responsible for curve evolution. Alvarez et al. noted that the differential operators normally involved in this evolution

model could be approximated using the composition of *infimum-supremum* morphological operators. This new scheme claims three advantages over its predecessor:

1. **Simplicity of implementation** – The level set is expressed a binary piecewise constant function
2. **Speed** – In testing, execution time was shorter, sometimes by full orders of magnitude
3. **Stability** – No re-initialisation of the level set or contour is required

The curve evolution for geodesic active contours in a level set framework is governed by the following equation:

$$\frac{\partial u}{\partial t} = g(I)v|\nabla u| + g(I)|\nabla u|\left(div\left(\frac{\nabla u}{|\nabla u|}\right)\right) + \nabla g(I)\nabla u \qquad \text{Eq. 3.1}$$

Where $u$ is the curve of the level set, $I$ is the image, $g(I)$ are the regions of $I$ which attract the curve (e.g. edges) and $v$ is the balloon force parameter.

Originally, the differential equation found in Eq. 3.1 was solved with numerical integration methods such as a finite-difference scheme. However, the newer evolution scheme uses a combination of morphological operators whose infinitesimal behaviour is equivalent to the flow expressed by the above equation. The first two terms in the above equation consist of the internal forces exerted on a curve (balloon force and smoothing respectively) while the third term comprises the external forces which attract the curve. Analysis of how morphological snakes approximates these terms follows:

**The Balloon-force term:**

The term responsible for the general expansion or reduction of a contour is given by

$$\frac{\partial u}{\partial t} = g(I)v|\nabla u| \qquad \text{Eq. 3.2}$$

Which strongly relates to the classical erosion and dilation morphological operators, defined by the functions $(E_h u)(x) = inf_{y \in hB} u(x - y)$ and $(D_h u)(x) = sup_{y \in hB} u(x - y)$ respectively.

As such, given the snake evolution at iteration *n*, the balloon force PDE applied over $u^n$ can be solved using the following morphological approach:

$$u^{n+1}(x) = \begin{cases} D_d u^n(x) & if \quad g(I)(x) \geq t_1 \wedge v > 0 \\ E_d u^n(x) & if \quad g(I)(x) \geq t_1 \wedge v < 0 \\ u^n(x) & otherwise \end{cases} \qquad \text{Eq. 3.3}$$

Where $t_1$ is a threshold value for the balloon force.

**The Smoothing Term:**

The term responsible for keeping the curvature of the level set's contour smooth is given by

$$\frac{\partial u}{\partial t} = g(I)|\nabla u| \left( div\left( \frac{\nabla u}{|\nabla u|} \right) \right) \qquad \text{Eq. 3.4}$$

The solution of the above PDE can be approached using line morphological operators. Letting *B* be the set of all line segments of length 2 centered at the origin, the line operators can be defined as $(SI_h u) = sup_{S \in B} inf_{y \in x + hS} u(y)$ and $(IS_h u) = inf_{S \in B} sup_{y \in x + hS} u(y)$.

Using these morphological operators, Eq. 3.4 is approached using the numerical scheme:

$$u^{n+1}(x) = \begin{cases} (SI_d \circ IS_d u^n)(x) & if \quad g(I)(x) \geq t_2 \\ u^n(x) & otherwise \end{cases} \qquad \text{Eq. 3.5}$$

Where $t_2$ is a threshold value for the smoothing force.

**The Attractor Force Term:**

The term responsible for attracting the curvature to certain image features is given by:

$$\frac{\partial u}{\partial t} = \nabla g(I) \nabla u \qquad \text{Eq. 3.6}$$

The solution to the above PDE can be approached using the following morphological discretization:

$$u^{n+1}(x) = \begin{cases} 1 & if \quad \nabla u^n(x) \nabla g(I)(x) > 0 \wedge g(I)(x) \geq t_3 \\ 0 & if \quad \nabla u^n(x) \nabla g(I)(x) < 0 \wedge g(I)(x) \geq t_3 \\ u^n(x) & otherwise \end{cases} \qquad \text{Eq. 3.7}$$

Where $t_3$ is a threshold value for the attractor force.

# Chapter 4 - Segmentation

## 4.1 Input

Full-body CT scans are unnecessary when diagnosis illnesses degenerative hip conditions. Physicians wishing to inspect a patient's hip-joint(s) via Computed Tomography would instead perform a localized scan centered on the joint. These partial-body scans usually start near the anterior superior iliac spine of the pelvis and end below the mine trochanter of the femur (see Figure 4.1(b)).

Current generation CT machines will often decompose the results of a scan as a set of numbered of slices, rather than the totality of the scan as a single volume. These slices are typically square in shape and parallel to a patient's transverse axis. Each slice is composed of a 2D grid of voxels, which when combined with every other slices composes recreates the entire volume of a scan.

Slices saved to disk can be likened to grey-scale images with intensity values representing levels of density rather than levels of color. Also unlike images, each intensity value does not range from [0, 255] but instead roughly follows the Hounsfield scale from [-1000, +1000].

In order to facilitate the adoption of our solution, we sought to keep our input as close to the output of CT machines as possible. To this end, we have chosen to use as initial input the sequence of numbered slices produced by CT machines. Once all slices have been loaded, these are reconstituted as a single volume with corresponding width, length and depth.

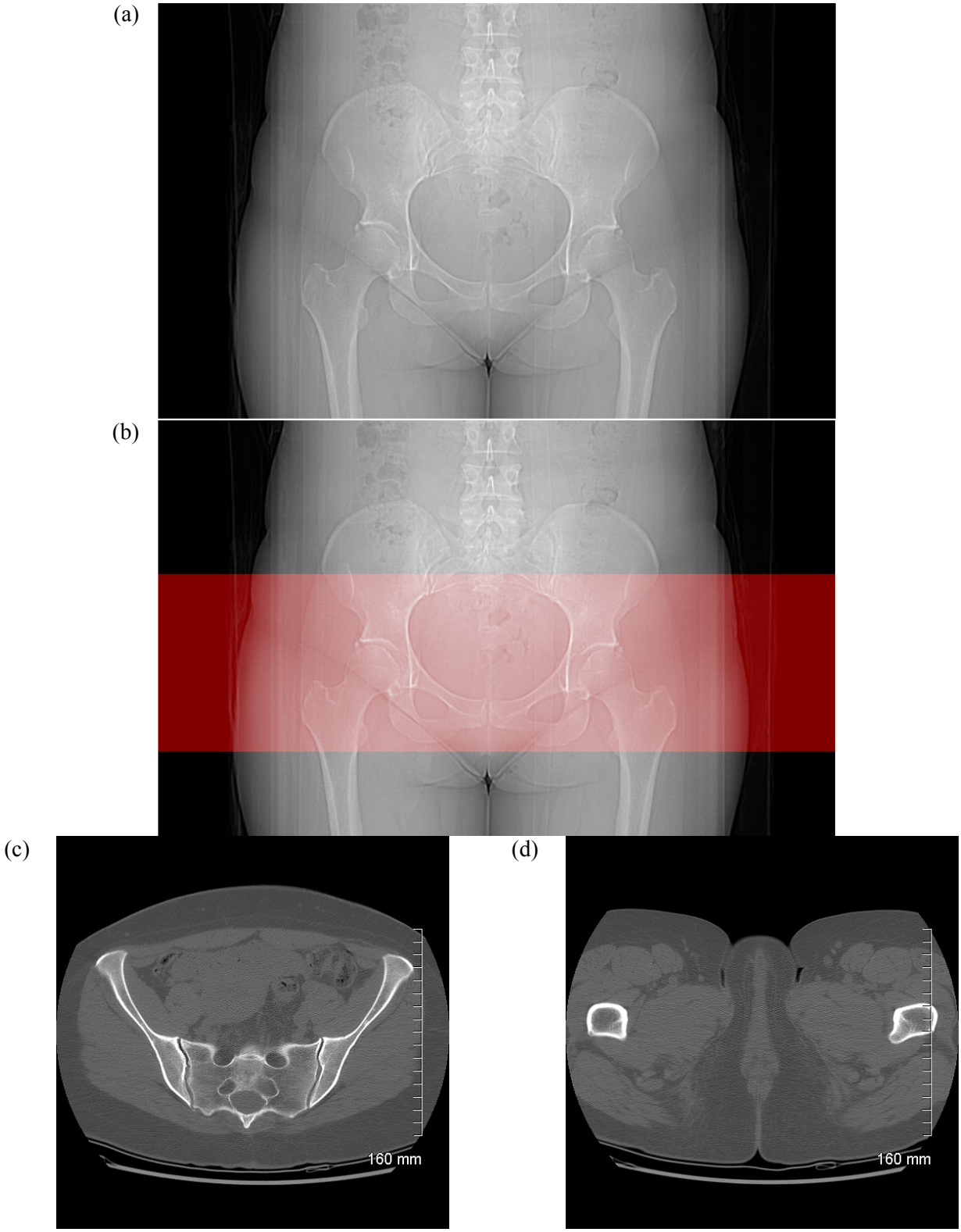


*Figure 4.1: (a) Radiograph of a patient's hip and waist (b) region commonly scanned by CT machine when investigating FAIs (c) Example top-most slice (d) Example bottom-most slice*

## 4.2 Pre-Processing the Hospital-Provided Input

The first step of the segmentation process is to convert the hospital-provided CT volume data into a format which more closely resembles an image format. This is done for three reasons:

1. To improve the compatibility of the CT data with pre-existing image-processing methods
2. To speed up slice processing by reducing the memory allocated to represent the volume
3. To facilitate visualisation of the CT data to the operator of our segmentation method

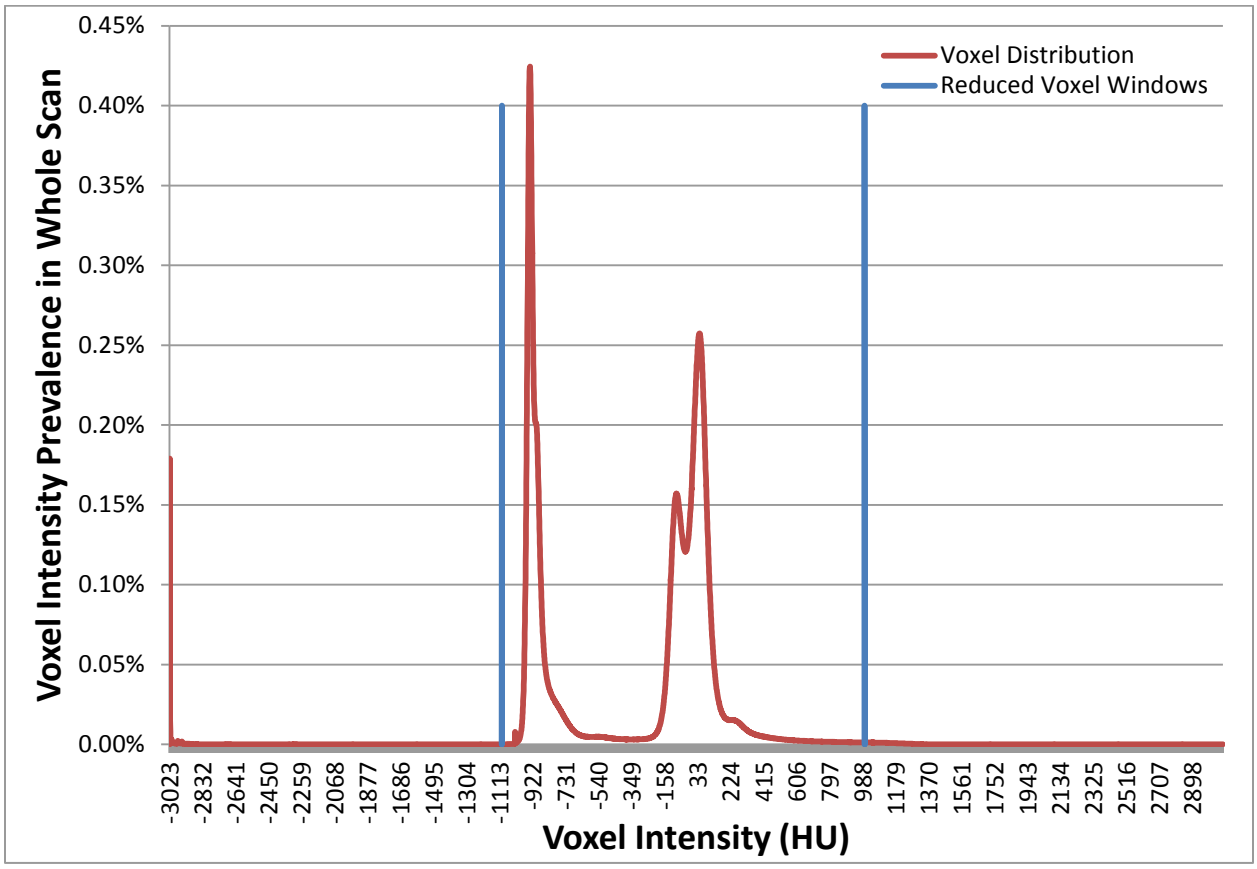


*Figure 4.2 Average voxel intensity distribution as observed from twenty pelvic CT scans. The blue bars demark the intensities at which the hospital-provided CT data is cropped during pre-processing*

The full range of the hospital-provided CT volume data's voxel values span beyond the expected -1000HU to +1000HU of the Hounsfield scale. In reality, sentinel value reserved

voxels outside of the CT machine's cylindrical scanning area registers as -3023HU while metal pins left over from past surgical corrections of fractured bones can go as high as +3100HU. However, as can be seen in Figure 4.2, the average CT scan is has the highest voxel concentration between -1100HU and +1000HU. In this graphic, the distribution's first maxima is located at air's radiographic attenuation level while the second and third maxima correspond to fat and muscle's radiographic attenuation level respectively. The distribution's long tail proceeding the third maxima represent the radiographic attenuation level for bones of varying densities.

In essence, the goal of the pre-processing step is to convert voxels whose value span [-3023, +3100] to the size of an unsigned byte [0, 255]. This conversion is helpful in that it (a) enables the use of pre-existing image processing tools without modification (b) allows a single dataset to be used both for the visualisation and processing of voxel data and (c) reduces the amount of memory allocated during individual processing steps. Conversion is accomplished through two steps:

1. **Cropping** – An upper and lower-bound is set to reduce the width of possible voxel intensities. Voxels whose values are lower than the lower-bound have their intensities set to the lower-bound. Likewise, voxels whose values are greater that the upper-bound have their intensities set to the upper bound. In testing, cropping with a lower-bound of -1000HU and upper-bound of +1000HU showed to be effective in keeping the sections of the Hounsfield scale most relevant to us intact. See the blue bars in Figure 4.2 to see how the window of possible voxel values shrinks. We included the attenuation for air within the cropping range because it provided the user a smoother, less grainy visualisation of the

CT slices. Other cropping ranges, such as ones only including the attenuations for fat, muscle and bone are also possible.

2. **Rescaling** – The remaining voxels of values [-1100, +1000] must be resized to fit within the [0, 255] range. This is done through are linear rescaling by using the following equation:

$$VOXEL_{PROCESSED} = round\left(\frac{(VOXEL_{SRC} - BOUND_{LOW}) \times 255}{BOUND_{HIGH} - BOUND_{LOW}}\right) \quad \text{Eq. 4.1}$$

Where $BOUND_{LOW}$ is the lower-bound for the cropping step, $BOUND_{HIGH}$ is the upper-bound for the cropping step, $VOXEL_{SRC}$ is the Hounsfield unit value of a voxel after the cropping step and $VOXEL_{PROCESSED}$ is the resulting voxel value whose value is between 0 and 255. Similarly to the $VOXEL_{SRC}$, increasing values in $VOXEL_{PROCESSED}$ correspond to voxels with higher radiographic attenuation values. Linear rescaling was used in order to liken our visualisations to those provided by the Hospital. However other quantization schemes which focus on bone are also possible.

Alternatively, an approximation of a processed voxel's corresponding Hounsfield unit value can be a retrieved by reversing the above formula to the one seen in Eq. 4.2.

$$VOXEL_{SRC} = round\left(\frac{VOXEL_{PROCESSED} \times (BOUND_{HIGH} - BOUND_{LOW})}{255} + BOUND_{LOW}\right) \quad \text{Eq. 4.2}$$

## 4.3 Initializing Regions of Interest

Our segmentation strategy is considered *semi-automatic* instead of *fully automatic* because it requires preliminary user-interaction in order to achieve its goal. The current stage of the

segmentation process contains all of these interactions, allowing the following stages to perform automatically.

The user's input is required in order to demarcate 3D regions-of-interest (ROI) within the volume of the CT scan. As we have decided to segment the femur head and body semi-independently, two partially-overlapping ROIs need to be specified before the segmentation procedure can begin in earnest. The first of these ROIs is tasked with encompassing the femur head and neighbouring acetabulum while the second contains the femur shaft all the way to the top of the greater trochanter.

Each ROI is given a starting voxel in the volume along with a length, width and depth (also measured in voxels). The advantages in using these ROIs are threefold:

1. **Side-specificity** – While delineating the ROIs, it is also possible to label it as belonging to the right or left femur. This is mostly useful in situations when a CT scan has been trimmed to include only one half of a patient's pelvis.
2. **Manual Placement of Landmarks** – Placing ROIs allows us ensure certain assumptions hold true regarding the object volume. Assumptions like the location of anatomical landmarks in the reduced volume.
3. **Efficiency** – Having a user take a short moment to place ROIs takes less time and invites less error than hypothetical automated methods designed to do the same thing.

### 4.3.1 ROI for the Femur Head

This ROI, hereby known as $ROI_H$, is composed of a single 3D box encompassing the whole femur head, the upper portion of the greater trochanter and neighbouring sections of the acetabulum (See Figure 4.3). Boundaries:

- The slice containing the very top of the femur head is used as an upper bound
- The slice containing the very bottom of the femur head is used as a upper bound
- The length and width of the ROI are sized to envelop
    - On one side: any section between the upper and lower bound containing the greater trochanter
    - On the other side: The acetabulum up until *obturator formen* (hole between the ischium and pubis bones)

Five to ten voxels padding are added as padding in each direction of the ROI's length and width. In addition to this, a voxel whose location roughly constitutes the *center of the femur head* is also selected by the user and attached to the ROI.

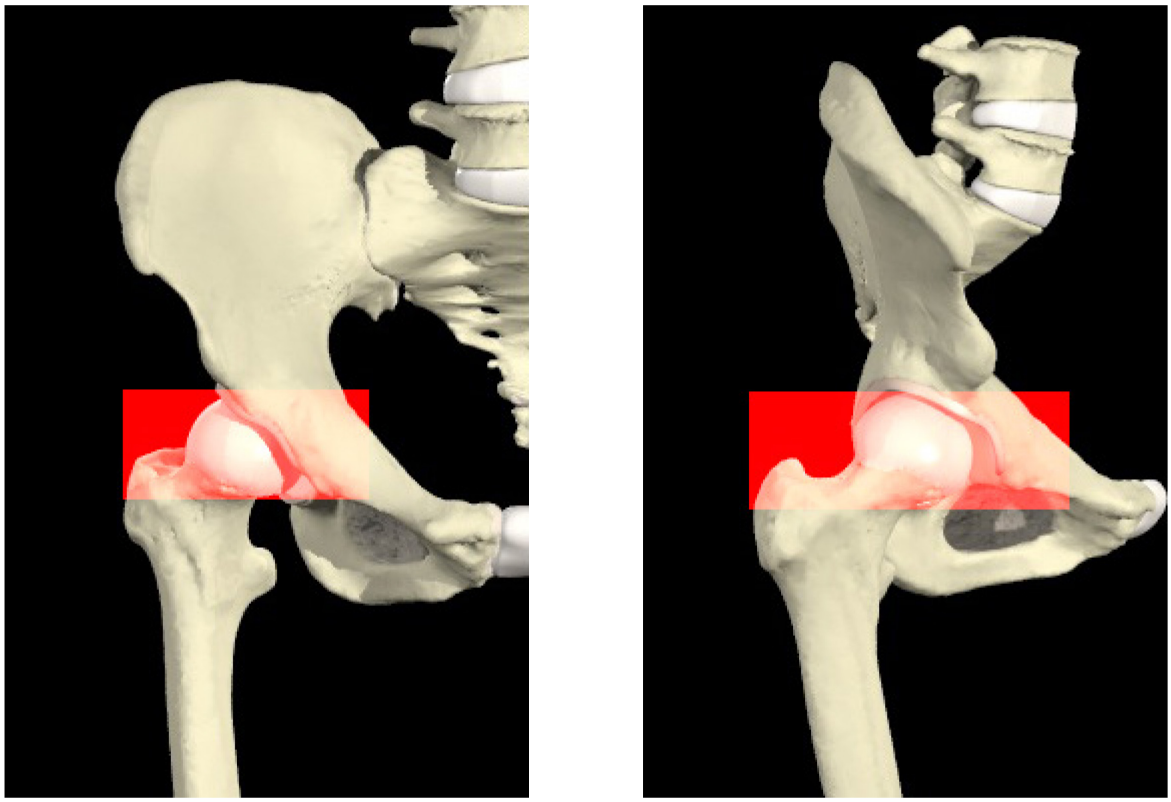

*Figure 4.3: Example $ROI_H$ is red seen from the patient's (left) front (right) right [59]*

### 4.3.2 ROI for the Femur Body

This ROI, hereby known as $ROI_B$, is composed of a single 3D box. This box contains the femur body up to the top of the greater trochanter (See Figure 4.4). Boundaries:

- Lower-bound is usually the lowest slice in the CT scan. It corresponds to a slice at the midsection of the femur's body.
- Upper-bound is the slice containing the top-most portion of the greater trochanter

The length and the width of the 3D box are roughly the same, centered on the middle of the femoral shaft and sized to include the entirety of the greater trochanter. In addition to this, the index of the slice where the cross-sections of the femur first appear as two disjoined objects (the femur head and greater trochanter) is also selected by the user and attached to the ROI. We hereby refer to this index as $Z_s$.

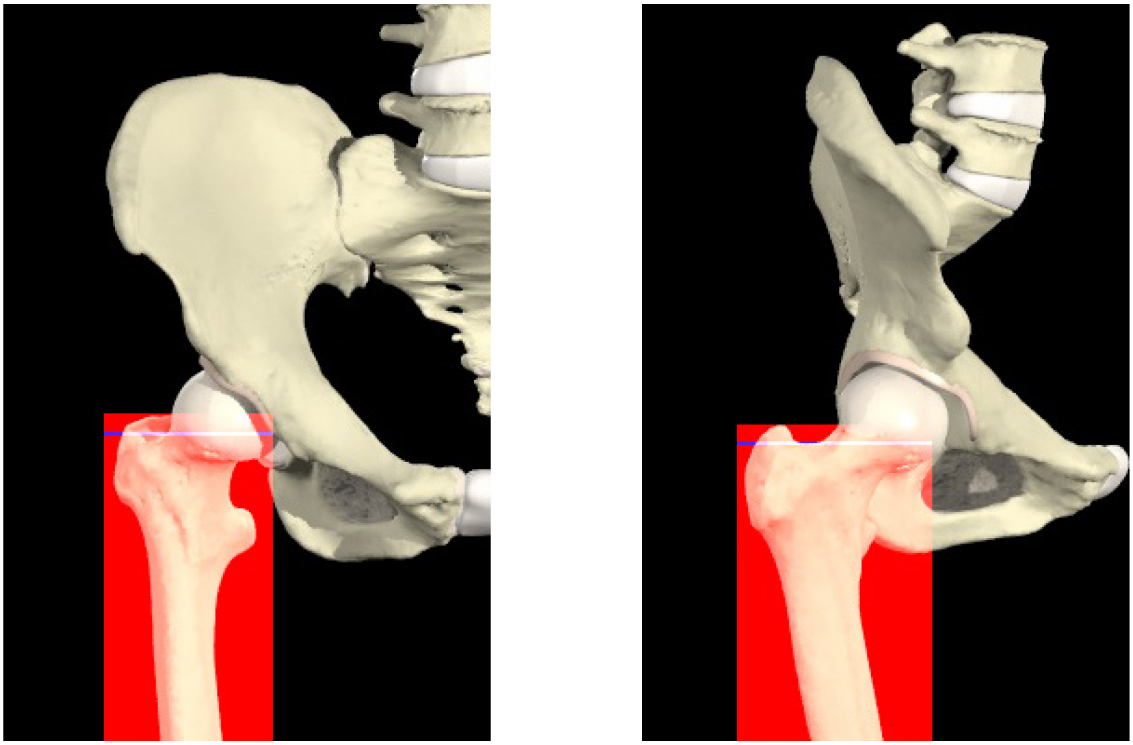

*Figure 4.4: Example $ROI_B$ in red with $Z_s$ as a blue stripe seen from patient's (left) front (right) right [59]*

## 4.4 Acetabular Rim Removal

The primary driving force behind our segmentation strategy is the morphological snake algorithm. If a slice contains a clear portion of the femur, we can envelop that portion with an initial contour for the snake method. The snake method with then be attracted to the femur's edges and provide us with an accurate outline of the femur which we can extract.

However, in cases where the femur is near to another object with strong edges, the snake may mistakenly be attracted to its edges instead, which leads to much less accurate outlines of the femur head. This is the case for the femur head being cupped by the acetabulum (Figure 4.5).

To neutralize this unwanted attraction, an "Acetabular-removal" phase is added to our solution prior to employing the snake segmentation methods. In this phase we cut-out portions of the acetabulum from our source data and cover-up the resulting hole with non-descript fill. Our starting point for this procedure is the ROI for the femur head created by the user in the last stage. This ROI facilitates acetabular removal by:

a) **Containing a list of all the slices near to the femur** - The ROI's upper-bound and lower-bound correspond to the slice number containing the very top and bottom of the femur. These two slices and all those between them constitute all of the set where the acetabulum might be close enough femur head to require removal.
b) **Additional parameters –** In addition the volume selected by the 3D bounding box, the femur head also has two additional parameters. The ROIs side (right or left) and femur-head center information allows us to better identify bone segments that might belong to the acetabulum based on their position to the femur head.

*Figure 4.5: CT slice showing the potential proximity of the femur to acetabulum*

It is important to note that this step is not concerned with segmenting the whole acetabulum. It instead concentrates on identifying parts of acetabulum which are near to the femur head and marginalizing their impact over the snake-based segmentation methods.

### 4.4.1 Thresholding

Our first step towards removing the acetabulum is to perform a thresholding of the image to highlight the segments of compact bone. Sections of the acetabulum adjacent to the femur have a shell of compact bone thick enough to preclude weak edges. As a result, thresholding a slice with an appropriate value provides a solid outline of the acetabulum in one or two connected fragments (see Figure 4.6).

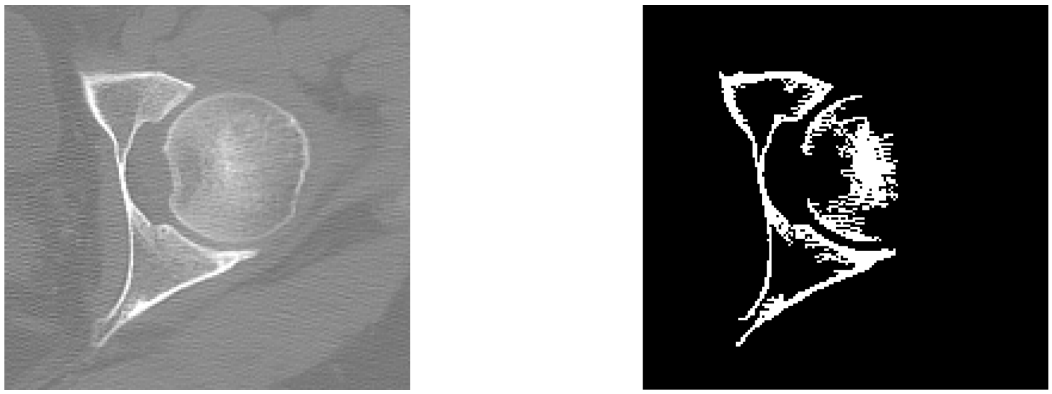

*Figure 4.6: Example slice from the femoral head ROI before (left) and after (right) thresholding*

### 4.4.2 Creating the mask

After having retrieved a binary image mapping the location of compact bone, we must create a mask of bone fragments for the original image which can cover the acetabulum without covering any section of the femur head. To do this, we decompose the thresholded image into sets of connected white pixels. Afterwards, we filter out fragments based which do not meet the following criteria:

- The fragment must be composed of a sufficient number of white pixels.
- The fragment location must be on the expected side (right or left) of the femur head center
- The fragment must have all of its elements a sufficient distance away from the femur head center

If the filtering process rejects all of the fragments, it is a sign that the value used during the thresholding phase was set too low. Tuning this parameter too low can cause the existence of a bridge of connected pixels between the femur head and acetabulum. If such a situation is detected, the threshold value is increased and the previous thresholding phase is automatically re-initiated.

*Figure 4.7: (left) Example initial mask for acetabular cut-out (right) Same mask after dilation and flood-filling, all regions not shaded in grey are used as the final mask*

Otherwise, any fragments which weren't filtered-out get imprinted onto a mask for the acetabulum. Following this, a dilation [60] is performed on the mask with a 3x3 square operator. This has the advantage of both joining disconnected fragments and also capturing the soft outline of the acetabulum which wasn't captured during the thresholding step.

The final touches include flood-filling a tertiary color into the corner of the mask. This allows us to distinguish between the empty area around the mask and the spongy-bone regions inside the acetabulum (Figure 4.7).

### 4.4.3 Cut-Out Filling

The final step of the acetabular removal process consists of replacing voxels which the mask identifies as belonging to the acetabulum. From the start, the goal of the acetabular removal phase was to eliminate some of the gradient which might cause the snake segmentation method to return erroneous results. To this end, we have opted to not replace the acetabulum with a flat colour, but with a *low-gradient fill* instead (see Figure 4.8). This low-gradient fill was specifically designed to provide a smooth appearance at all points of the cut-out acetabulum.

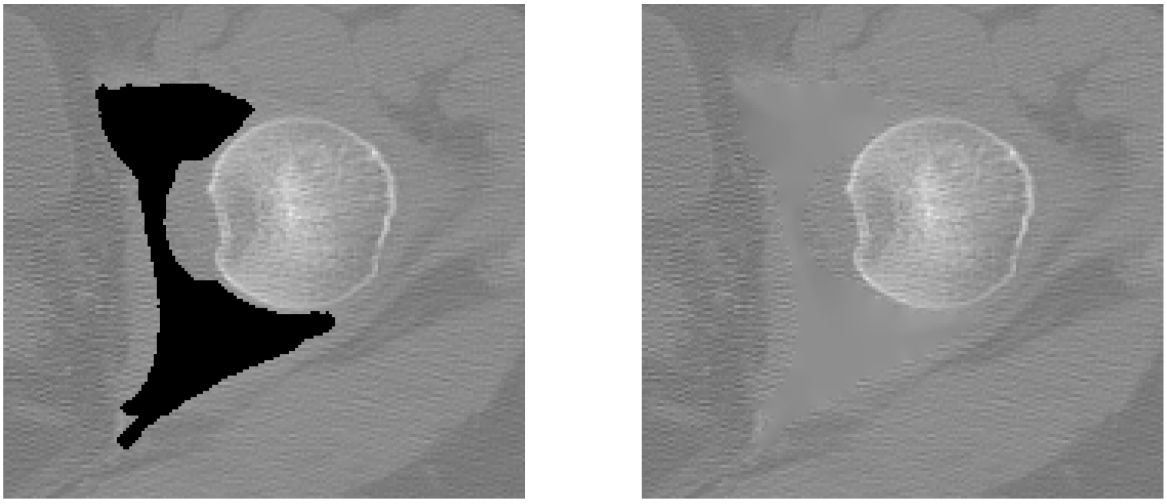

*Figure 4.8: (left) Example acetabular cut-out with black fill (right) Same cut-out with low-gradient fill*

The implementation details of the low-gradient fill can be read at Algorithm 4.1. The primary idea behind the algorithm is to use an offshoot of Gaussian smoothing to fill in the acetabuluar cut-out. The method works by starting at the outside of the cut-out and working its way in. An additional feature in the algorithm is that it attempts to converge the gradient to a certain color.

The soft tissue most often found around the acetabulum is muscle. As this is the case, instructing the low-gradient fill method to converge to the same color intensity as muscle prevents the formation of high-gradient spines along the center of the cut-out. This combination of blending and convergence allows the cut-out to be largely ignored by the snake segmentation method.

*Algorithm 4.1: Low-Gradient Fill*

Input:

$I_{original}$ : Original 2D Image
$I_{mask}$ : Binary mask of that image
SK[N][N] : Gaussian smoothing kernel of size N * N
CC : Convergence color

Output:

$I_{filled}$ : Original Image with filled acetabulum

1) All the pixels in $I_{filled}$ are initially set to a sentinel value
2) Any pixels from $I_{original}$ not covered by $I_{mask}$ are copied to $I_{filled}$
3) Any pixels from $I_{original}$ covered by $I_{mask}$...
   a) Are assigned a rank [from 0 to 8] based on the number of neighbours it has without sentinel values
   b) Are linked to a look-up-table based on this rank
4) While the look-up-table is not empty, choose one of the pixels with the highest rank ($P_R$)...
   a) Overlap SK over $I_{filled}[P_R]$ to get a set of neighbouring pixel ($P_N$) and smoothing kernel (SK[I][J]) pairs.
      i) If $P_N$ has a sentinel value
         (1) $Acc_V$ += CC
         (2) $Acc_N$ += 1
      ii) Otherwise
         (1) $Acc_V$ += $I_{original}[P_N]$ * SK[I][J]
         (2) $Acc_N$ += SK[I][J]
   b) Remove Sentinel value at $P_R$
   c) $I_{filled}[P_R] \leftarrow Acc_V \div Acc_N$
   d) Update ranks in look-up-table

## 4.5 Pre-processing Region of Interest contents

In addition to acetabular rim removal, we use three pre-processing methods which generally improve the quality of our results: ceiling thresholding, flooring thresholding and upscaling. By default, all three methods are applied prior to each one of the contour-extraction steps. However, these functions can also be toggled-off individually and for individual steps of the segmentation procedure if a user has reason to believe that it will improve results.

### 4.5.1 Ceiling Thresholding

We apply a *ceiling threshold* method to highlight bone voxels while still keeping lower-intensity voxel information. See Algorithm 4.2 for implementation details and Figure 4.9 for a before-and-after comparison.

*Algorithm 4.2: Ceiling Threshold*

Input:

$I_{original}$ : Original 2D Image
T : Threshold value
R : Replacement value

Output:

$I_{thresh}$ : Thresholded image

1. For every pixel *p* in $I_{original}$
2. If $I_{original}[p] >= T$
   a. $I_{thresh}[p] \leftarrow R$;
3. Else
   a. $I_{thresh}[p] \leftarrow I_{original}[p]$

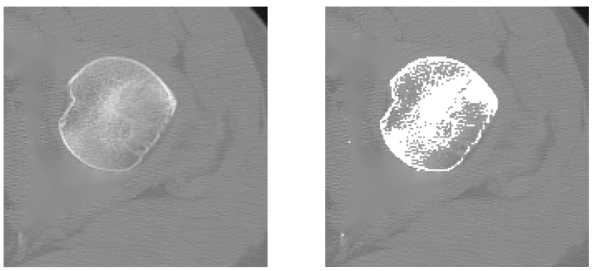

*Figure 4.9: slice (left) before ceiling-thresholding (right) after ceiling-thresholding*

### 4.5.2 Flooring Thresholding

We can also apply a *flooring threshold* method to unify the intensities of different types of soft tissues. See Algorithm 4.3 for implementation details and Figure 4.10 for a before-and-after comparison. Note that if this pre-processing method is enabled for a slice in $ROI_H$, the low-gradient-fill step can be omitted from the acetabular rim removal procedure. This stands to reason as the fill will be floored.

*Algorithm 4.3: Flooring Threshold*

Input:

$I_{original}$ : Original 2D Image
T : Threshold value
R : Replacement value

Output:

$I_{thresh}$ : Thresholded image

1. For every pixel *p* in $I_{original}$
2. If $I_{original}[p] <= T$
   a. $I_{thresh}[p] \leftarrow R$;
3. Else
   a. $I_{thresh}[p] \leftarrow I_{original}[p]$

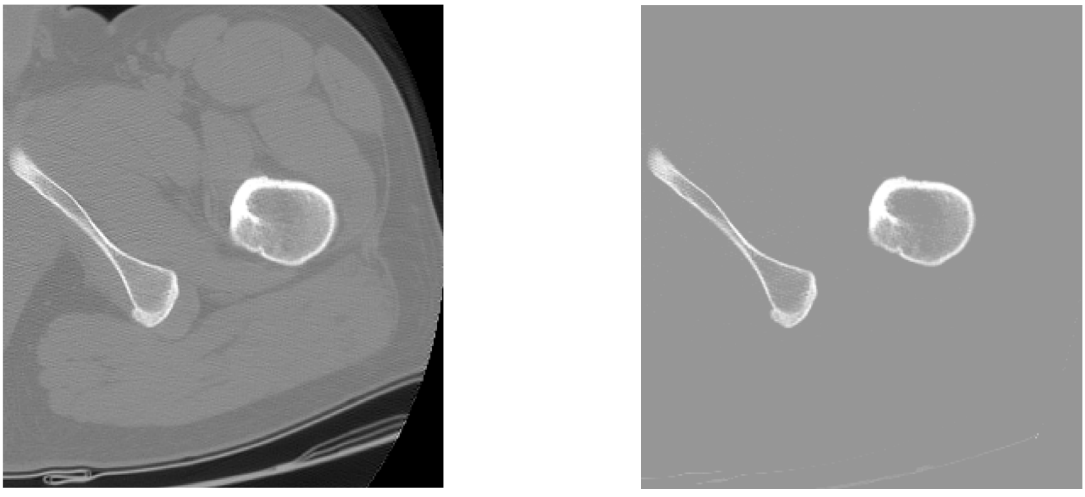

*Figure 4.10: Cross-section of the femur body (left) before flooring threshold applied (right) after flooring thresholding applied*

### 4.5.3 Upscaling

The internal forces acting on a snake's evolving contour exist to ensure that the curve remains smooth and well-rounded. This is desirable for segmenting objects whose curvature arc slowly. However, when applied to objects with narrow sections or sharp changes in the direction of edges, this internal force can be the source of premature termination of curve evolution or cause the curve to enter the object it is attempting to segment [61].

Due to the comparatively low resolution of the CT slices, small concavities exist in the in cross-sections of the femur head and neck which may invoke the detrimental effects of an evolving snake's internal forces.

Our simple, but effective solution is to *upscale* the contents of the ROI. In this case, upscaling refers to resizing a slice's contents inside the ROI by an integer scale factor, without using any interpolation. This has the effect of artificially widening narrow concavities on the femur's surface and diluting sharp angles in a cross-sections contour, leading to improve results. Once a final contour has been extracted from an upscaled ROI, the contour is downscaled by the same scale factor prior to becoming our final segmentation result.

The downside to this solution is that it increases the amount of time required to extract a femur contour. This can be attributed to the size of the evolving contour being increased, resulting in needing to calculate the external forces being exerted on the curve by more voxels. However, we find this trade-off acceptable for small scale-factor values due to the great improvement in results.

## 4.6 Femur Head

Once the relevant voxels belonging to the acetabulum are replaced with a low-gradient fill, the contour extraction of the femur can begin. Of the two ROIs which cover the femur, we approach the segmentation of the femur head first.

The femur head is near-spherical in shape. Correspondingly, a cross-section of the femur head which appears in CT slices will appear near-circular. This type of shape makes it well suited for snake-based segmentation methods. During the evolution of a snake's contour, internal forces assure that the curvature of the contour remains smooth. A side-effect of these internal forces is that snake methods cannot capture contours which have sharp corners or narrow protrusions. The near-circular cross-section of a femur head, possessing neither of these features, is therefore a better candidate for snake-based segmentation methods.

Our strategy for segmenting the femur head includes two successive steps:

1. **Primer slice segmentation** – Using ROI information, find the first 2D contour for the femur head
2. **Subsequent slice segmentation** – Using the primer slice's contour as a base, find neighbouring 2D contours for the femur head

Through the combination of these steps, the 2D contour of the femur head is found across every slice in the ROI, completing half of our 3D segmentation method.

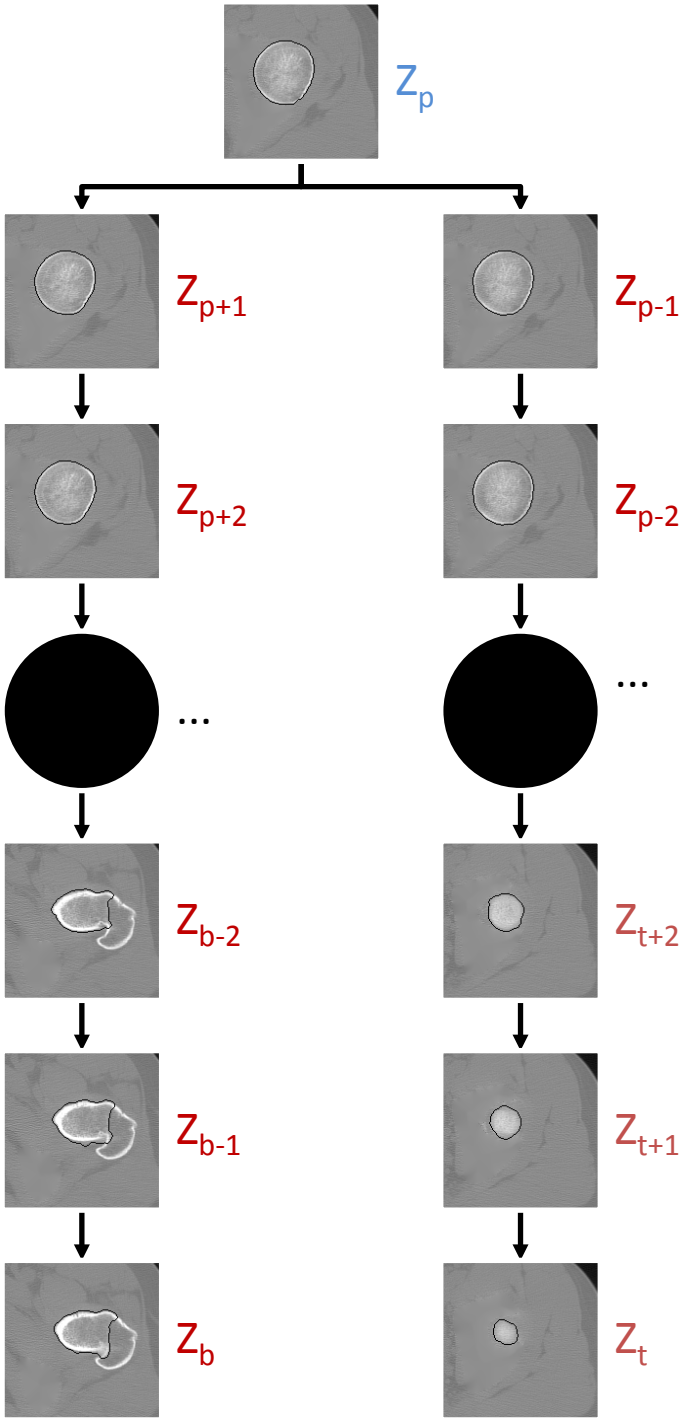


*Figure 4.11: Progression chart of each slice's segmentation where the primer slice appears in blue and the subsequent slices in red. Note that the ROI's primer slice, top-most slice and bottom-most slice are denoted as $Z_p$, $Z_t$ and $Z_b$ respectively*

### 4.6.1 Primer slice segmentation

We refer to the slice in an ROI which is the first to have its femoral contour extracted as the "primer" slice. What differentiates this slice's segmentation process from the others is how its initial contour is derived. Unlike the procedure for other slices, the primer slice has its femur head contour segmented twice: the first time to attain a *rough* contour and the second time to achieve a semi-final *fine* contour. This twice-over segmentation is a cost-effective way to free the user from setting an initial contour him- or herself.

Instead, *rough* contour extraction starts with an initial contour the size of the whole ROI. When used as input for the first morphological snake pass, this oversized initial contour will deflate into an approximation of the femur head which may have a few defects.

During *fine* contour extraction, the final contour from the rough extraction is re-processed to be used as the initial contour of the second morphological snake pass, which returns our final contour this slice.

Before extracting contours, we have found that pre-processing the slice promotes better results during the curve evolution. Specifically, we **upscale** the input of the snake algorithm and perform a **ceiling threshold** on the contents of the femur-head's ROI.

The primer slice for $ROI_H$ is chosen to be the slice which is nearest to the center. Formally, the primer slice $Z_p$ is chosen with Eq. 4.3:

$$Z_p = Z_t + round\left(\frac{Z_b - Z_t}{2}\right) \qquad \text{Eq. 4.3}$$

Where $Z_t$ is the top-most slice of the ROI and $Z_b$ is the bottom-most slice. Selecting a slice in the middle of the ROI guarantees two things:

1. The femur-head's cross-section will have a diameter which is amongst the largest in the ROI. This follows from the fact that the femur head's shape is near spherical
2. The femur-head's cross-section will have a sharp, if thin, border

#### *4.6.1.1 Finding a rough contour*

The rough contour extraction serves to find a starting point for the fine contour extraction. The initial contour for this stage is the largest circle whose entirety fits inside the ROI's area. This circle has its center at the ROI's mid-width and mid-height. The circle will also have a radius equal to the ROI's mid-width or mid-height, whichever is smallest. The femur-head is bound to be fully within the limits of the circle due to the landmarks used to size the femur-head ROI. See Figure 4.12 for an example.

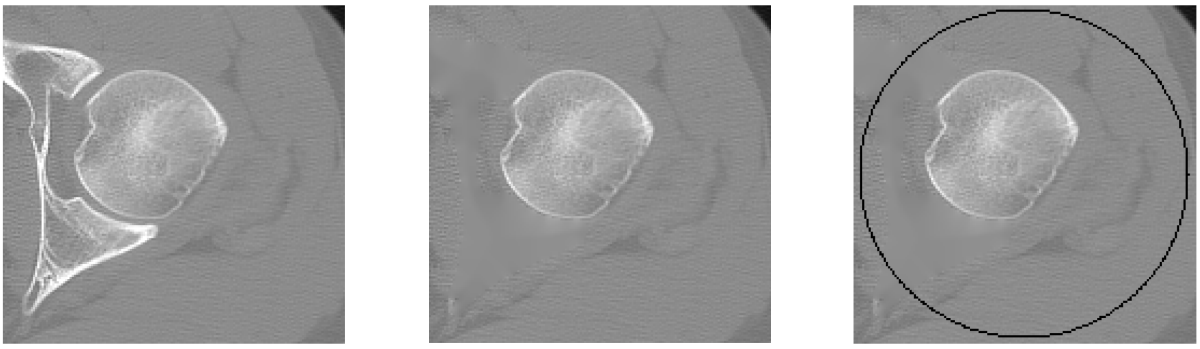

*Figure 4.12: Primer Slice (left)As it originally appears (middle) After acetabular removal (right)With superimposed rough initial contour in black*

The morphological snake algorithm is used on the Primer slice using the circle as an initial contour. For the rough contour, the snake parameters are set to have a strong, negative balloon force and a weak edge-attraction force.

The balloon force is set to negative value so that contour will "deflate" (contract in size) instead of "inflate" (expand).

The balloon force is high compared to the attraction force due to the expectation that the initial contour will be located some distance away from its final location. In order to reach its

expected destination, the algorithm may have to overcome local minima of gradients caused by soft tissues. For example, when a layer of fat meets muscle, it creates a streak of gradient which can prematurely halt the snake's evolution.

Given the circular initial contour and the right parameters, the morphological snake will return a rough final contour which approximates the femur head, as seen in Figure 4.13.This contour may approximate the femur-head's exterior near perfectly or it may contain have a few flaws. For the rough contour, a few protrusions or depressions from the femur head's shell is acceptable. What's most important to retrieve from the first pass of the morphological snake algorithm is the general curvature of the femur head.

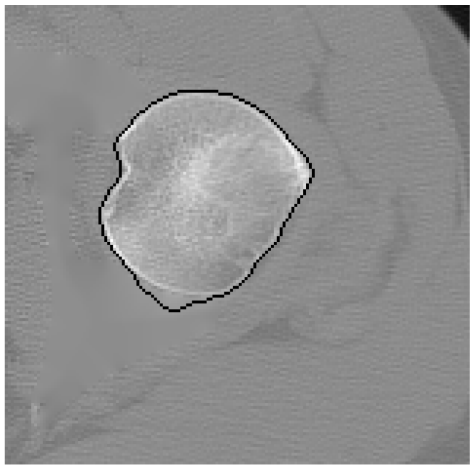

*Figure 4.13: Primer slice with superimposed rough final contour in black*

The final step in the rough contour extraction is to provide an initial contour for the fine contour extraction. We have chosen to use a circle which closely encapsulates the femur head to this end. To get a circle from our rough final contour we:

1. *Hough circle Transform* – We perform a Hough circle transform on the rough final contour to determine the circle which best approximates the shape of the femur. We improve our results by using an elliptical-Gaussian kernel voting scheme similar to the

one used by Fernandes & Oliveira [62]. In addition, we use a narrow-band approach around the ROIs femur –center point to speed-up the process.

2. *Widen circle radius* - While the Hough transform method will return the circle which best overlaps with the femur-head, some of the voxels belonging to the ideal contour may be outside this circle. In order to ensure their inclusion, we increment the radius value of the circle slightly.

Both the Hough-detected circle and the widened circle can be seen in Figure 4.14. Once we have the latter, we are ready to begin the fine-contour segmentation process.

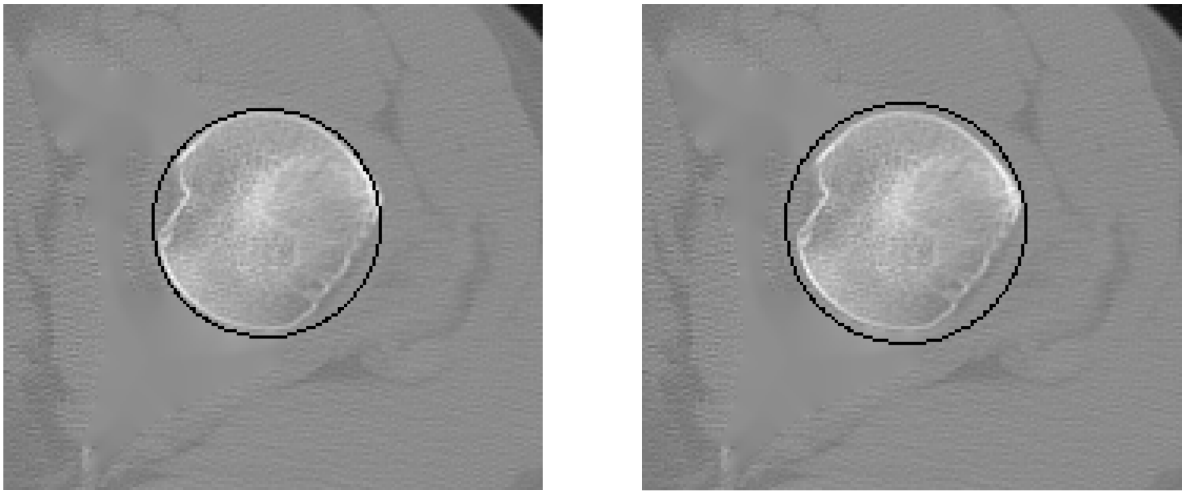

*Figure 4.14: Primer slice(left) with superimposed circle from Hough Transform (right) with superimposed widened circle*

Our reasoning for this circular re-initialisation of the primer slice stems from two observations:

1. Femur cross-sections at $ROI_H$'s middle-most slice are always circular or near-circular. This makes the final contour from the rough step an ideal candidate for Hough circle detection, both in terms of shape and short execution time. The elliptical-Gaussian kernel voting scheme we use for our Hough transformations returns very accurate

results, but is computationally expensive. Overall, we save time by applying the transformation on the comparatively sparse final contour of the rough step rather than applying it directly to the CT slice after acetabular removal.

2. The contour re-initialisation has proven useful in scenarios where distant fragments of the acetabulum linger after the rim is removed or the greater trochanter's top appears in the primer slice. These scenarios can cause small sections of the contour to remain isolated from the femur head during curve evolution. Re-initializing the contour through Hough circle detection allows us to guarantee that all sections of the initial contour for the fine step are within the same range of the femur head. See Figure 4.15 for an example.

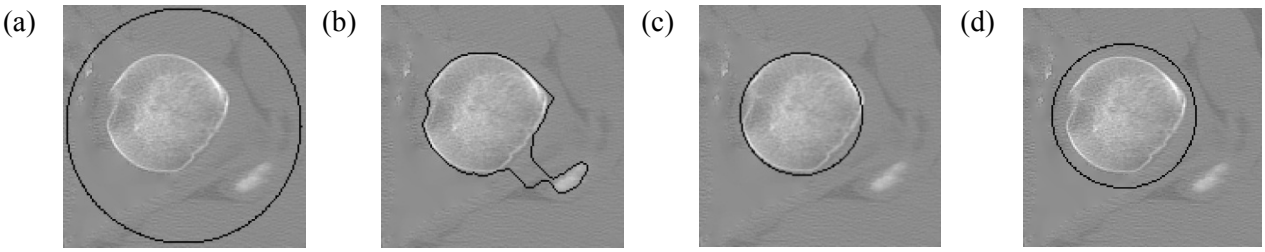


*Figure 4.15: Example of how Hough's transform can be used to recover from errors in the rough step: (a) initial contour for the rough step (b) final contour for the rough step with error due to greater trochanter (c) Best fitting circle from Hough Circle Transform (d) Widened circle*

#### *4.6.1.2 Finding a fine contour*

The fine contour segmentation is the second-pass of the morphological snake on the primer slice. The final contour of this snake operation provides us with the decisive segmentation result for the femur head in primer slice.

After the primer slice has undergone pre-processing, it is ready for the second pass of the morphological snake algorithm. The circle that was detected by Hough transformation and widened during the rough-contour extraction phase is used as the initial contour.

The snake parameters used in the second pass focus on a strong attraction force with a weaker deflation force. This is contrary to focus of the first snake pass. This change is validated by our knowledge that the initial contour will be much closer to the desired final contour in the second pass than the first.

Because of these changes, the snake algorithm will return results with are tighter to the bone and less-error prone than those of the rough contour. An example of the final segmentation of the fine contour is shown in Figure 4.16.

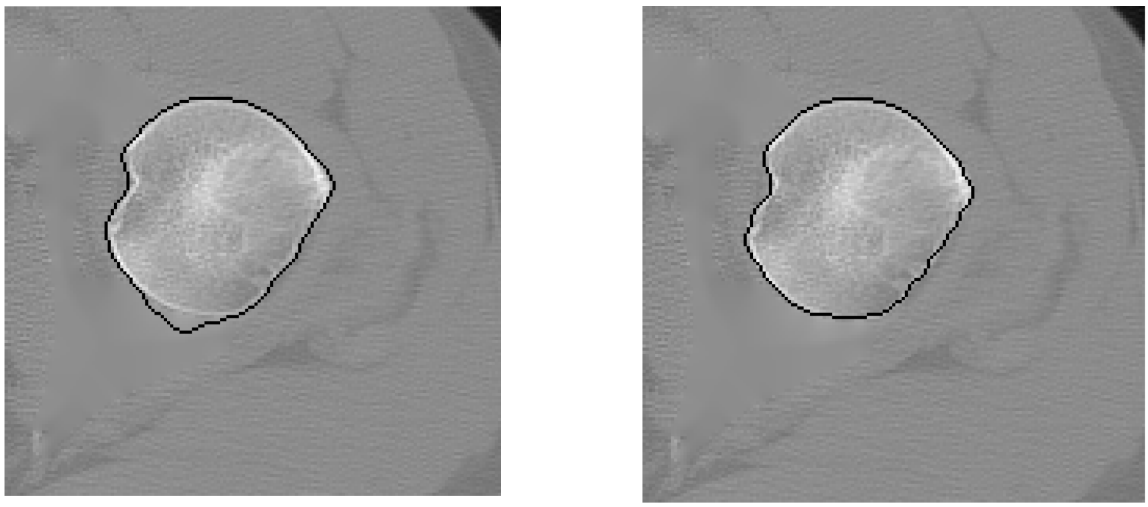

*Figure 4.16: Example final segmentations for the femur head detected during the rough (left) and fine (right) contour extraction*

### 4.6.2 Subsequent Slice Segmentation

Once the primer slice has been segmented, we can sequentially begin segmenting the other slices in the femur head's ROI. The slices are ordered based on their distance from the primer slice. If the primer slice is noted as $Z_p$, then the next slices to be segmented will be $Z_{p+1}$ & $Z_{p-1}$, followed by $Z_{p+2}$ & $Z_{p-2}$, $Z_{p+3}$ & $Z_{p-3}$ and so on. Segmenting the whole ROI entails performing individual, sequential segmentation away from the primer slice in both the superior and inferior direction. This cascading-style segmentation ends once the bottom-most slice has had its contour

extracted (in the case of the inferior direction) and when the top-most slice has its contours extracted (in the case of the superior direction)

The method of segmenting these subsequent slices is similar to the one reported during the fine contour stage. They differ only in how they obtain their initial contour. The primer slice obtains its initial contour by adding an introductory pass of the snake method. This pass allows the general size and location of the femur head to be deduced within that slice of the ROI. This information is used to place the ring which is used as the initial contour for the fine contour's pass.

Across different slice of the ROI, the femur head's location does not change very much, although the femur head's size does. Given the near-spherical size of the femur head, it can be safely assumed that the primer slice, being the middle-most slice, contains one of the largest cross-sections of the femur head. The near-sphericity of the femur head also allows us to assume that cross-sections of the femur head will gradually get smaller the farther away they are from the femur head center.

With these assumptions in mind, we have decided to base the initial contour of an as-of-yet un-segmented slice by basing it on the final contour of its neighbouring slice. Thus, an un-segmented slice $Z_i$ will base its initial contour on $Z_{i+1}$ if it is above the primer slice and $Z_{i-1}$ if it is below the primer slice. Before a neighbour's final contour can be used as an initial contour, it is expanded with the following steps:

1. A blank image is created with the same dimension as a slice
2. The neighbour's final contour is imprinted onto the blank image
3. A flood fill operation is used to distinguish between the background of the image and regions inside the imprint of the neighbour's final contour

4. The regions inside the contour are expanded using a set of successive dilation operations
5. The expanded contour is extracted from the image by first locating a pixel not belonging to the background and then tracing the exterior of the attached object

This expansion is used to safeguard against moderate differences in shape between neighbouring femur-head cross sections. An example of this contour expansion can be seen in Figure 4.17.

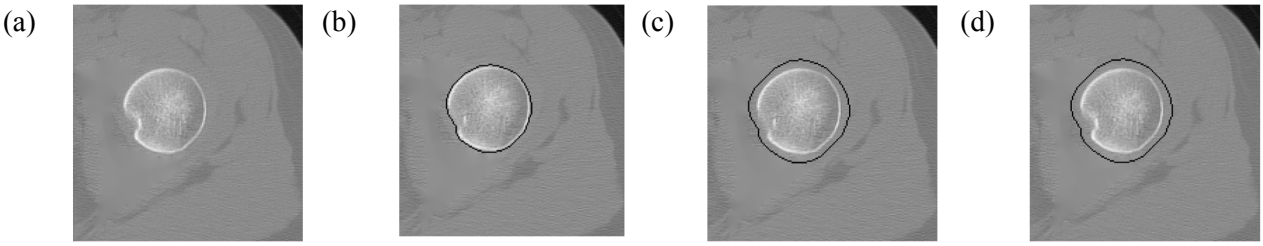


*Figure 4.17: (a) Slice $Z_i$ in need of an initial contour (b) Slice $Z_{i+1}$ with final contour (c) Slice $Z_{i+1}$ with dilated final contour (d) Slice $Z_i$ using $Z_{i+1}$'s dilated final contour as an initial contour*

Basing a slice's initial contour on its neighbour's final contour allows us to eliminate the rough pass of used for the primer slice. This "single pass" method allows us to reduce the time required to segment each slice. The removal of a rough pass includes the removal of a one of the two applications of the snake algorithm along with the Hough circle transformation.

Once the initial contour has been set for an un-segmented slice, the rest of the procedure is identical to the one used to get the fine contour for the primer slice. To reiterate these steps:

1. Obtain slice in ROI (Done)
2. Obtain initial contour for the femur-head cross-section of this slice (Done)
3. Perform ceiling threshold on slice's image information
4. Upscale Slice
5. Upscale Initial Contour
6. Apply a morphological snake on the upscaled slice with upscaled initial contour

7. Downscale the resulting final contour
8. Use final contour as segmentation of the femur-head for this slice

To illustrate how these steps work in conjunction with the initial contour being a modified version of the neighbouring slice's final contour, Table 4.1 shows nine iterations of this method for the top half of the femur head. These iterations start from a Primer slice $Z_p$ obtained though the rough/fine contour extraction previously detailed.

Conversely, Table 4.2 shows nine iterations of this method for the bottom half of the femur head. Once again, these iterations start from a primer slice $Z_p$. In slices containing traces of the greater trochanter, it can be seen that the final contours do not encapsulate the extra bone. This is both the case for slices containing the femur head and greater trochanter as joined or disjoined objects. This is an expected result of femur-head segmentation stage as it is only concerned with capturing the spherical portion of the femur head. Any part of the femur not segmented during the femur-head step will be segmented instead during the femur-body step and the union of both segmentations will provide a complete model of the femur.

*Table 4.1: Sample sequence of initial contours (red) and final contours (green) starting from the primer slice and iterating towards the top of the femur head*

| Slice | Contours | Slice | Contours |
|---|---|---|---|
| $Z_p$ | 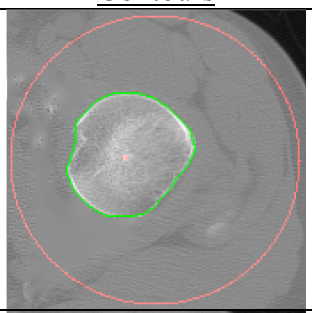 | $Z_{p-5}$ | 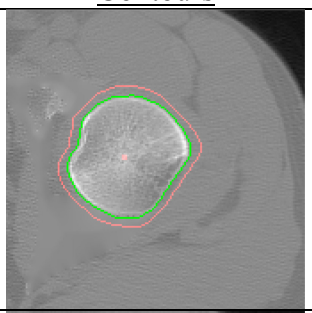 |
| $Z_{p-1}$ | 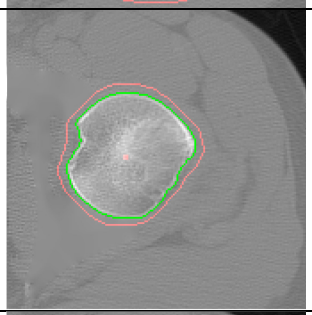 | $Z_{p-6}$ | 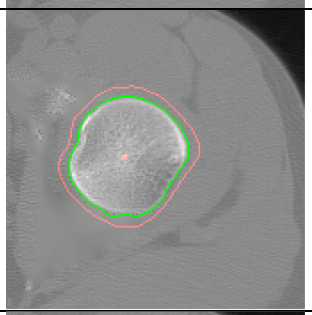 |
| $Z_{p-2}$ | 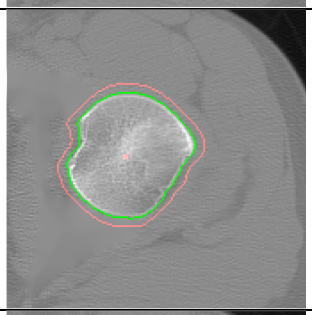 | $Z_{p-7}$ | 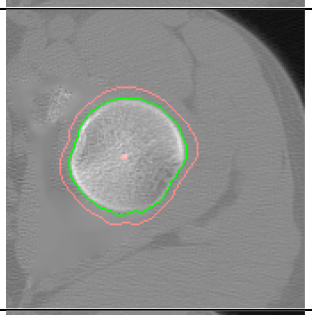 |
| $Z_{p-3}$ | 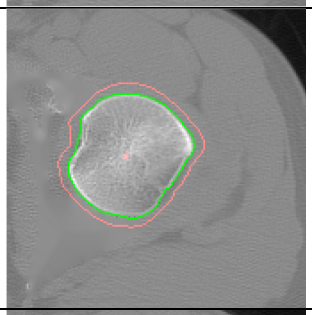 | $Z_{p-8}$ | 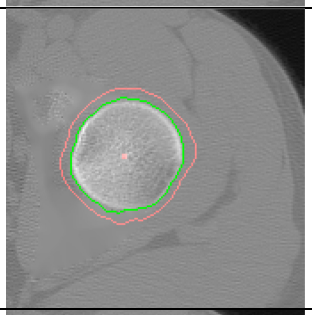 |
| $Z_{p-4}$ | 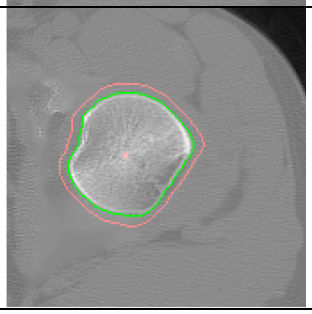 | $Z_{p-9}$ | 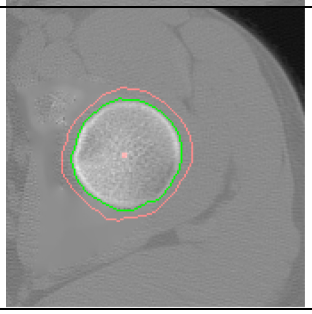 |

*Table 4.2: Sample sequence of initial contours (red) and final contours (green) starting from the primer slice and iterating towards the bottom of the femur head*

| Slice | Contours | Slice | Contours |
|---|---|---|---|
| $Z_p$ | 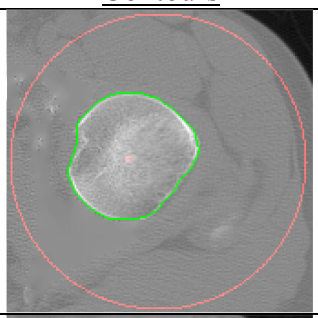 | $Z_{p+5}$ | 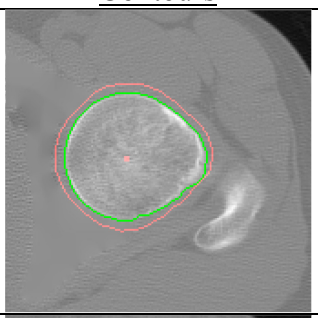 |
| $Z_{p+1}$ | 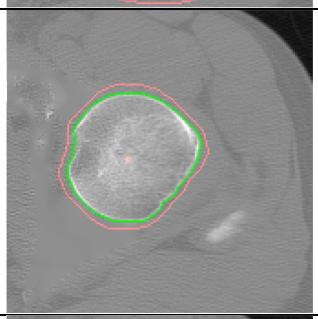 | $Z_{p+6}$ | 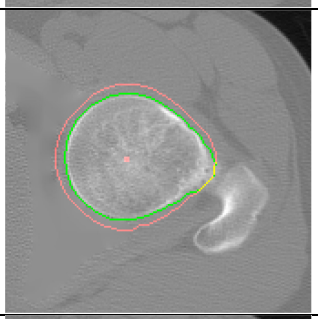 |
| $Z_{p+2}$ | 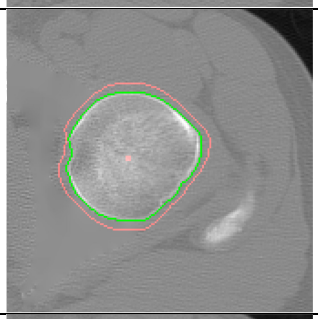 | $Z_{p+7}$ | 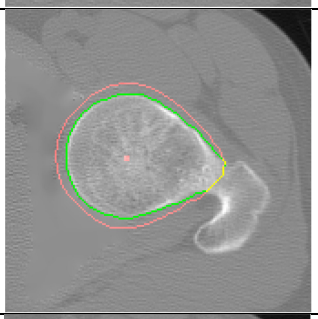 |
| $Z_{p+3}$ | 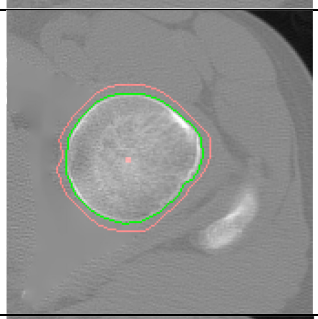 | $Z_{p+8}$ | 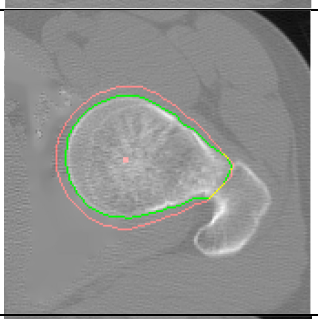 |
| $Z_{p+4}$ | 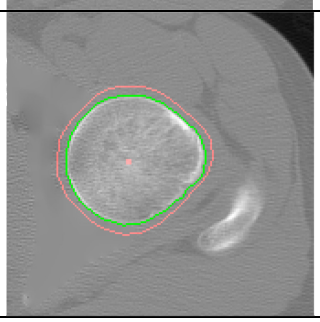 | $Z_{p+9}$ | 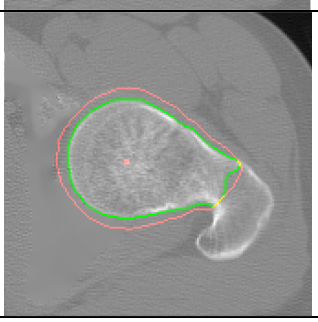 |

## 4.7 Femur Body

The femur, like most long bones, has as much thicker shell of compact osseous tissue around its shaft than it does at its epiphyses [9]. This results in the slices from the femur body being easier to segment than those from the femur head, on account of the compact bone's high contrast with the soft tissue that surrounds it. In addition, the femur body does not have adjacent bones which need to be isolated due to their proximity, once again unlike the femur head with the acetabulum.

The femur body, being vertically tubular in shape is another good candidate for a slice-by-slice segmentation strategy as was used for the femur head. In fact, the contour extraction method we use for the femur body follows closely the one employed for the femur head, with a few minor exceptions. The biggest of these exceptions being that $ROI_B$ has $Z_s$; a slice where the femur splits into two disjoined objects. This split will necessitate a single-slice exception on how initial contours are derived.

Our segmentation strategy for the femur body once again consists of two consecutive steps: (a) starting by obtaining the rough contour of a primer slice, followed by its fine contour (b) the segmentation of subsequent slices, where the primer slice's segmentation initiates an outward cascade of basing an un-segmented slice's initial contour on its neighbouring's slice's final contour.

Compared to the femur head, the femur body is much more likely to come in contact with intra-muscular fat. In CT slices, this intramuscular fat appears as dark streaks between lighter sections of muscle. The contrast between the fat and muscle cause detrimental gradients which can produce unwanted forces on an evolving snake. However, since the surface of the femur body is well defined due to its thick shell of compact osseous tissue, we can "flatten" the

appearance of slices in $ROI_B$ to collapse the intensities of the fat and muscle together. Therefore, in addition to **upscaling** the input of the snake algorithm and performing a **ceiling threshold** on the contents of the femur-head's ROI, we also perform a **flooring threshold** to promote better results.

## 4.7.1 Primer Slice Segmentation

For the $ROI_B$, the primer slice is not the slice which is nearest to the center. Instead the bottom-most slice is chosen, which we refer to as $Z_b$. This slice should also correspond to the bottom-most slice of the pelvic scan, and contain a tubular cross-section of the femur body.

### *4.7.1.1 Finding the rough Contour*

Once again, the rough contour extraction finds a starting area for the fine contour extraction. The initial contour for this stage is the largest circle whose entirety fits inside the $ROI_B$'s area. Once this has been fitted, the morphological snake algorithm is applied to the slice using the same set of "rough" parameters used on the femur-head's primer slice.

Given the thick, high-contrast shell of the femur body, the final contour should be virtually free of defects and quite close to the result that will be obtained during the fine contour extraction phase (see Figure 4.18). Slightly jagged contours are likely to the only visible flaws on the rough contour, and even these will be reset using the fine step.

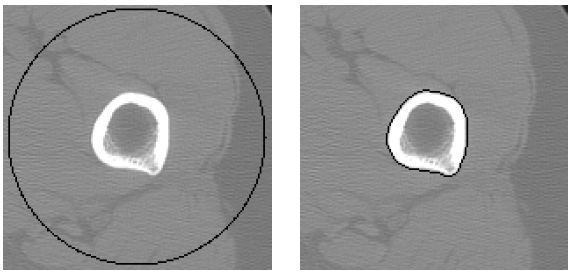

*Figure 4.18: (left) Initial contour for rough step (right) final contour for rough step*

#### 4.7.1.2 Finding the fine Contour

The fine contour serves the same purpose here than it did for the femur head: providing the decisive segmentation of the primer slice. Unlike the femur-head however, the cross-section of the femur body is not near-circular, meaning we do not employ a Hough transformation on the rough step's final contour to extract the best-fitting circle. Instead, we dilate the rough step's final contour much as we do for the sequential slices. The result is a curve which is near evenly-distanced from the femur body at the primer slice (see Figure 4.19). We use this contour as the fine step's initial contour

The final contour for the primer slice is obtained when the morphological snake algorithm is applied to our new initial contour. Correspondingly, we use the "fine" set of segmentation parameters to ensure the best results.

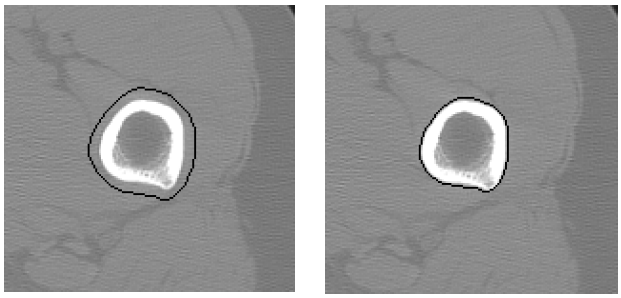

*Figure 4.19: (left) Initial contour for the fine step (right) Final contour for the fine step*

### 4.7.2 Subsequent Slice Segmentation

With final contour of the primer slice well defined, we continue with the segmentation of all the other slices in $ROI_B$. Our procedure for doing so is familiar: performing successive segmentations away from the primer slice. However, the primer slice for the $ROI_B$ is the bottom-most slice, so we can only iterate upwards.

Thus, an un-segmented slice $Z_i$ will always base its initial contour on $Z_{i+1}$. However, prior to using $Z_{i+1}$'s final contour as $Z_i$'s initial contour, we use the dilation morphological operator once again to expand the contour, ensuring that no sections of the femur head are outside its domain.

However, there exists a single slice in $ROI_B$ which requires exceptional initialization. That slice is $Z_s$; where the greater trochanter and femur-head first become two, disjoined objects. The split occurs at the height of intertrochanteric line and the greater trochanter tops-out shortly thereafter. Of the two objects, we focus on segmenting the greater trochanter as the femur head has already been segmented to completion.

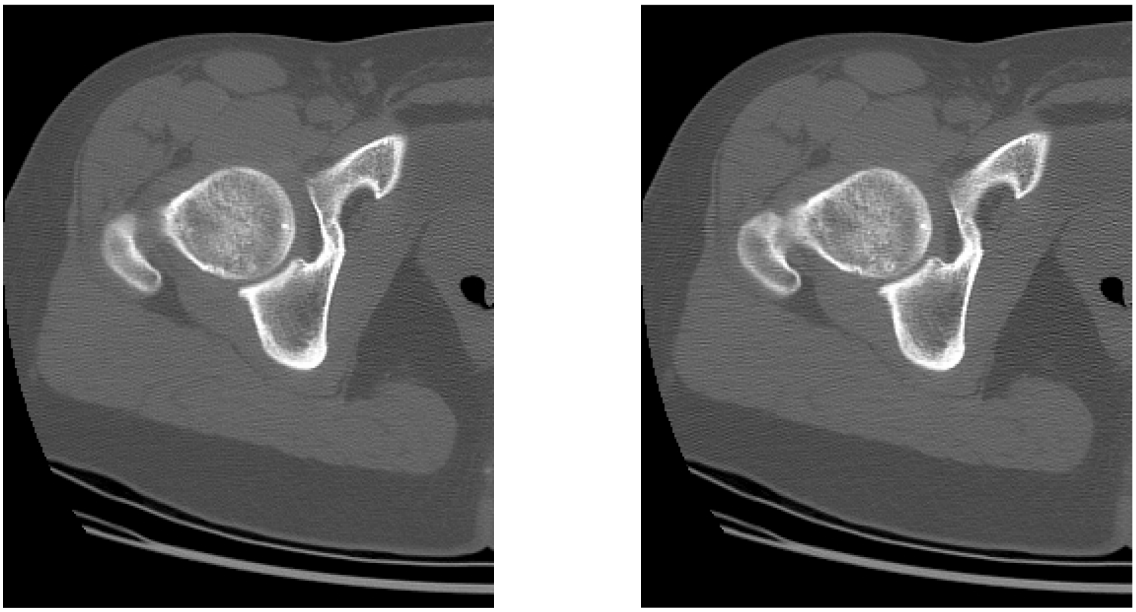

*Figure 4.20: Slices (left) $Z_s$ where the femur appears as two disconnected objects (right) $Z_{s+1}$ where the femur appears as a single connected object*

The initial contour for $Z_s$ is based not only the final segmentation of slice $Z_{s+1}$ in $ROI_B$, but also from the final segmentation of slice $Z_{s+1}$ in $ROI_H$. For shorthand's sake, we refer to the set of voxels contained within the final contours of slice $Z_{s+1}$ for $ROI_H$ as $V_H$ and the set of voxels contained within the final contours of slice $Z_{s+1}$ for $ROI_B$ as $V_B$. By subtracting the set of voxels in $V_H$ from $V_B$, we can obtain a good estimation of the greater trochanter's cross-section in slice

$Z_s$. Thus we use the largest set of connected voxels of $V_B - V_H$ to provide and initial contour for slice $Z_s$ (See Figure 4.21).

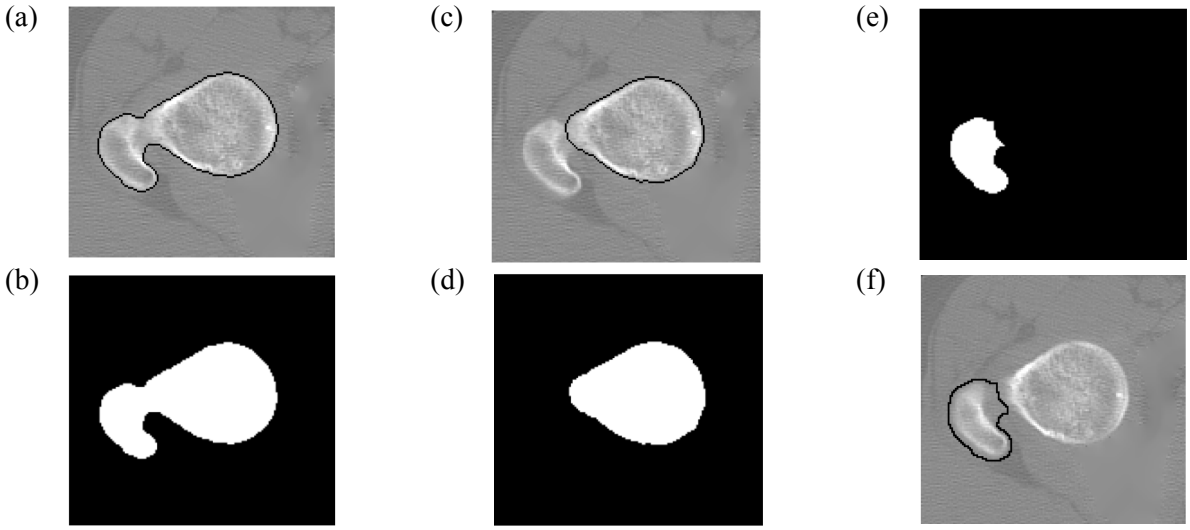


*Figure 4.21: (a) Final contour for slice $Z_{s+1}$ in $ROI_B$ (b) Voxels of set $V_B$ (c) Final contour for slice $Z_{s+1}$ in $ROI_H$ (d) Voxels of set $V_H$ (e) Volume for $ROI_H$ subtracted from $ROI_B$ (f) slice $Z_s$ with its initial contour*

No matter how one of the subsequent slices obtains its initial contour, it is used as input for the morphological snake algorithm along with the set of "fine" snake parameters. The final curve provided by the algorithm becomes our definite segmentation for $ROI_B$.

*Table 4.3: Sample sequence of initial contours (red) and final contours (green) starting from the primer slice and iterating towards the top of the femur*

| Slice | Contours | Slice | Contours |
|---|---|---|---|
| $Z_p$ | 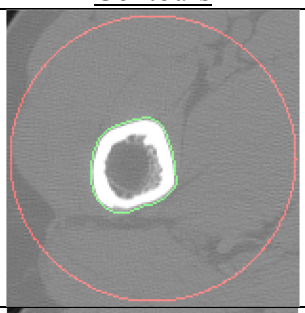 | $Z_{p+36}$ | 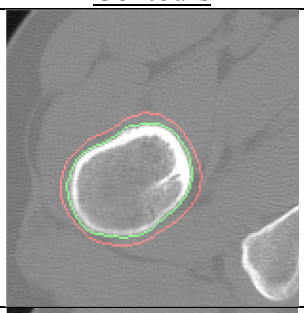 |
| $Z_{p+12}$ | 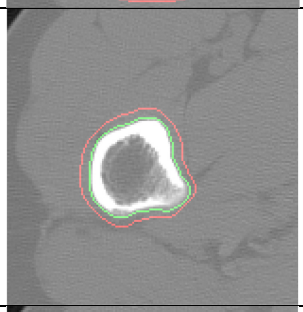 | $Z_{p+42}$ | 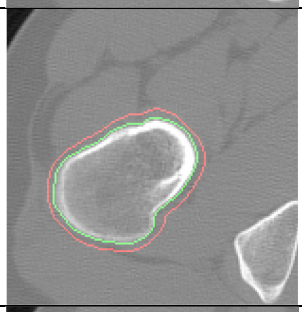 |
| $Z_{p+18}$ | 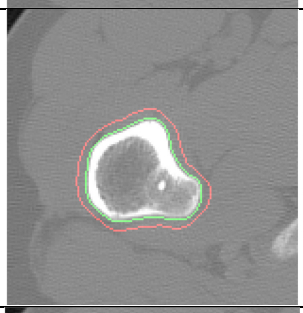 | $Z_{p+48}$ | 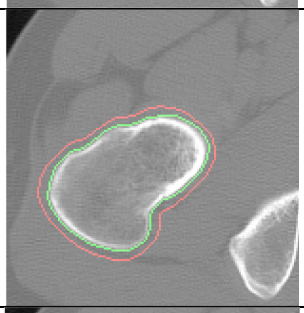 |
| $Z_{p+24}$ | 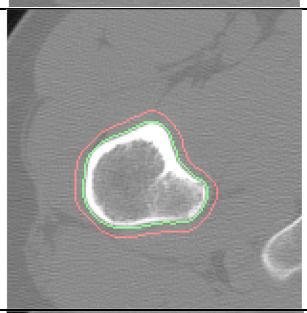 | $Z_{p+54}$ |  |
| $Z_{p+30}$ | 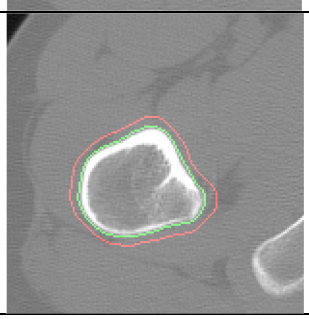 | $Z_{p+60}$ |  |

*Table 4.4: Sample sequence of initial contours (red) and final contours (green) starting from the $Z_s$ and continuing with its neighbouring slices*

| Slice | Contours | Slice | Contours |
|---|---|---|---|
| $Z_s$ | 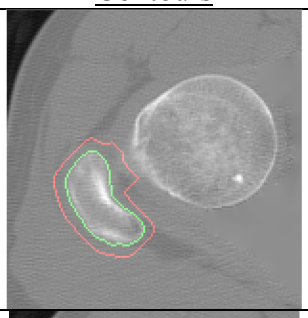 | $Z_{s+1}$ | 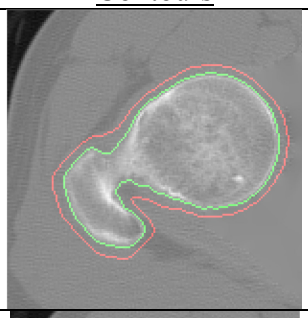 |
| $Z_{s-1}$ | 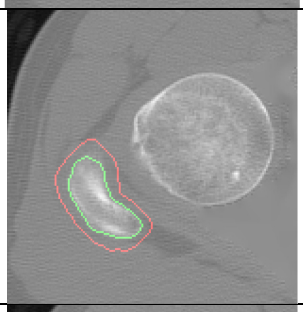 | $Z_{s+2}$ | 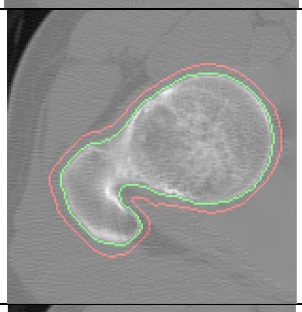 |
| $Z_{s-2}$ |  | $Z_{s+3}$ | 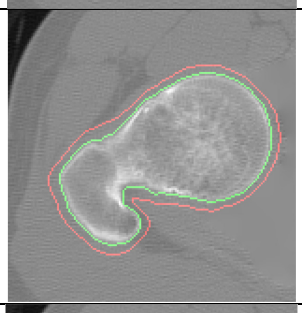 |
| $Z_{s-3}$ |  | $Z_{s+4}$ | 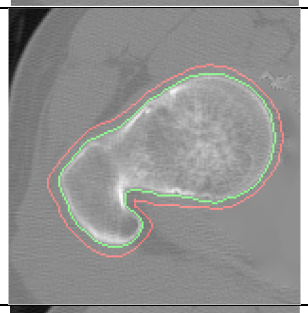 |
| $Z_{s-4}$ | 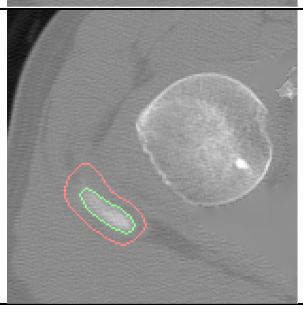 | $Z_{s+5}$ |  |

## 4.8 Post-Processing

The final step in our segmentation process is where we create a single model for the segmented femur. This is a simple matter of calculating the union between the voxels encased by $ROI_H$'s final contours with voxel's inside for $ROI_B$'s final contours.

This union will allow us to consolidate the slices which are only covered by one of the ROIs versus those covered by both. From here, the results can be viewed as its native collection of voxels or be polygonized for an improved presentation. See Figure 4.22 for an example of how the two voxel sets combine to create our final, patient specific 3D model of a femur.

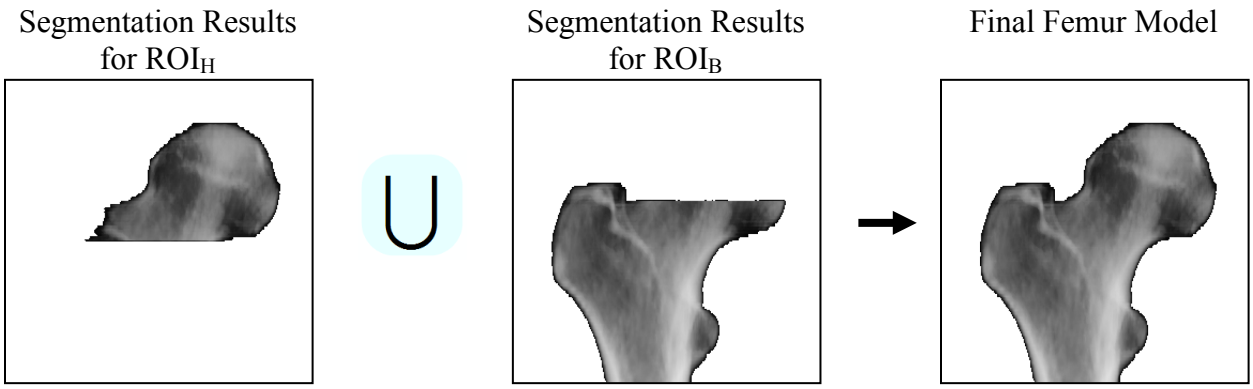


*Figure 4.22 Sample union of the 3D model from $ROI_H$ and the 3D model from $ROI_B$*

# Chapter 5 - Experimental Results and Evaluations

## 5.1 Hospital Database

We have received from the Ottawa General Hospital the medical images of 20 patients. Of these patients, 17 were formally diagnosed with a cam impingement in a least one hip while 3 belonged to a control group. For each patient, three sets of medical images were obtained: (1) a pelvic CT scan (2) an antero-posterior radiograph of the patient's pelvis along with (3) a lateral radiograph of the patient's pelvis. These images were taken between July 2006 and February 2008 and their breakdown and a summary of the physician's diagnosis can be found in Table 5.1.

*Table 5.1: Breakdown of the 20 patient from the Hospital's database*

| | **Male** | **Female** | **Total** |
|---|---|---|---|
| Number of Scans | 15 | 5 | 20 |
| Mean Age* | 36.9 | 36.6 | 36.8 |
| Youngest * | 19 | 29 | 19 |
| Eldest* | 54 | 47 | 54 |
| # Patients with Bilateral FAI | 6 | 1 | 7 |
| # Patients with Unilateral FAI (Left) | 4 | 3 | 7 |
| # Patients with Unilateral FAI (Right) | 2 | 1 | 3 |
| # Patients from Control Group | 3 | 0 | 3 |

*Age at scan's time of taking

### 5.1.1 DICOM Format

All of the medical images contained within the Hospital's FAI Database saved in the *Digital Imaging and COmunications in Medicine* (DICOM) [63] file format. Each of these DICOM files contains either a radiograph of a single slice from a CT scan encoded as lossless JPEG images. In

addition to image information, the DICCOM files also contains auxiliary information This information can be classified as regarding the

- **Patient** – Name, age , sex and referring physician
- **Imaging Machine** – Manufacturer and model
- **Image Acquisition** – Date taken, peak kiloVoltage, exposure time, x-ray tube current
- **Image Properties** – Resolution of the image, number of images in the set, Real-world dimensions of the voxels/pixels (in mm), the image's distance from the radiographic source

### 5.1.2 CT Scans

All of our medical images were acquired using a Lightspeed Plus CT Scanner by General Electric. The radiographs were captured first, and immediately followed by a CT scan. Both the radiographs and CT scans were taken using the LightSpeed Plus' *body filter*; however the radiographs are processed using a *STANDARD* convolution kernel while the CT scan highlight bones by using a *BONEPLUS* convolution kernel.

The spatial dimensions for both the radiographs & CT scans were nearly identical across patients, and can be seen in Table 5.2 and Table 5.3 respectively. The only difference being that CT scans of different patients differ in their number of slices.

*Table 5.2: Spatial properties of pelvic radiographs*

| **Area Resolution** | | **Pixel Spacing** | |
|---|---|---|---|
| **Resolution** | **Resolution** | **Width** | **Height** |
| 888 px | 596 px | 0.5968 mm | 0.5455 mm |

*Table 5.3: Spatial properties of pelvic CT scans*

| **Volume Resolution** | | | **Voxel Spacing** | | |
|---|---|---|---|---|---|
| **X** | **Y** | **Z** | **Width** | **Height** | **Depth** |
| 512 px | 512 px | Varying | 0.6836 mm | 0.6836 mm | 1.25 mm |

It's worth noting that the voxels are not cubic. A voxel's depth is nearly twice the size of its width of height. This is attributed to the selected distance between consecutive slices. It is important to remember that CT imaging exposes the patient to radioactive sources. Thus, increasing the distance between slices decreases the overall number of slices, resulting in less radiation exposure to the patient.

Each pixel/voxel is represented using a 16-bit monochrome signed intensity value which can be immediately translated into Hounsfield Units.

## 5.2 Testing Database

Of the 20 patients in the hospital database, we selected 6 which provided the most diverse sampling of patient sex, age, FAI pathology, bone femur size, femur orientation and femur shape. Particulars for each patient are displayed in Table 5.4 .

We subsequently manually segmented the femurs from the CT scans of each of these six patients, resulting in twelve, high accuracy femur models. These manual segmentations were performed in an image editing program, on a voxel-by-voxel, slice-by-slice basis in order to maximize their accuracy. As these manual segmentations were time consuming to obtain, we decided that twelve femurs were our bottom line to test the diversity of the hospital database.

*Table 5.4: Characteristics of the six patients who had their femurs manually segmented*

| **Patient #** | **Age** | **Sex** | **FAI Diagnosis** |
|---|---|---|---|
| 1 | 39 | M | Bilateral |
| 2 | 47 | F | Left |
| 3 | 29 | F | Left |
| 4 | 33 | M | Left |
| 16 | 22 | M | Right |
| 17 | 54 | M | Control |

Other than femur size, orientation and the presence of FAIs, our sample set shows a number of other inter-patient variations which would test the rigour of any femur segmentation strategy.

The most important dissimilarities between patients are innevitably located at or near the femur head. The femur body's thick, tubular sshape lessens the impact of inter-patient differences as far as segmentation is concerned.

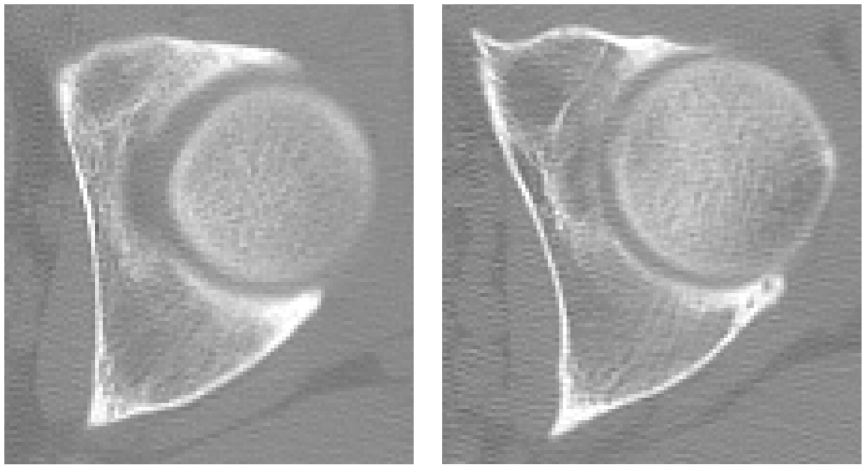

*Figure 5.1: Femur and acetabulum appear (left) well-spaced (right) close at points*

As an example, Figure 5.1 shows a slice where the boundaries of the femur-head and acetabulum appear quite close due to blurred edges and CT noise. Any segmentation strategy will need to separate these two objects.

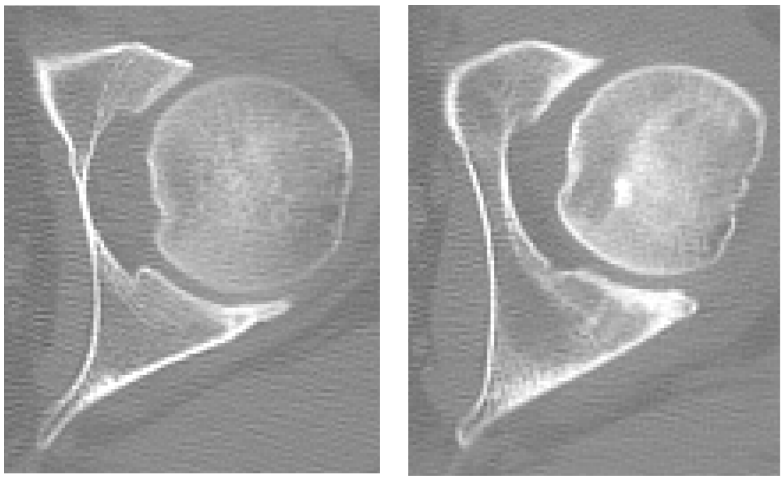

*Figure 5.2: Cross-sections where the femur head appears (left) near-circular (right) deformed*

Strict model-based metthods will have difficulty getting the contours from the right image in Figure 5.2 as it's a far cry from the average femur shape. Any segmentation strategy which seeks to enforce a sphericity constraint over the femur head will especially have difficulty here.

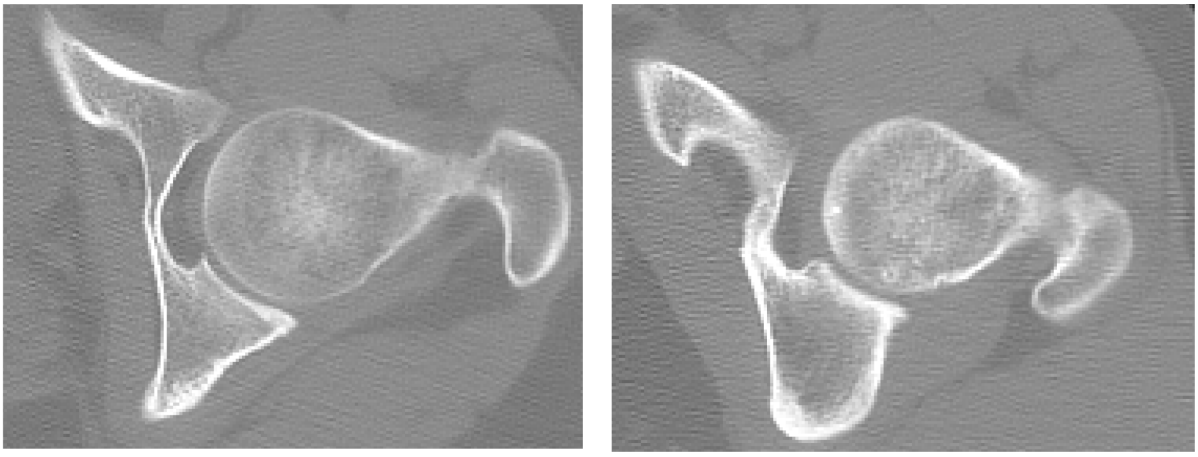

*Figure 5.3: Concavity between femur head and greater-trochanter is (left) wide (right) narrow*

Differential gaps between femur head and greater trochanter can be seen in Figure 5.3, where the more narrow of the two is expected cause some snake methods to halt their curve evolution prematurely. Also worth noting is the higher prevalence of compact bone in the slice with the narrow concavity.

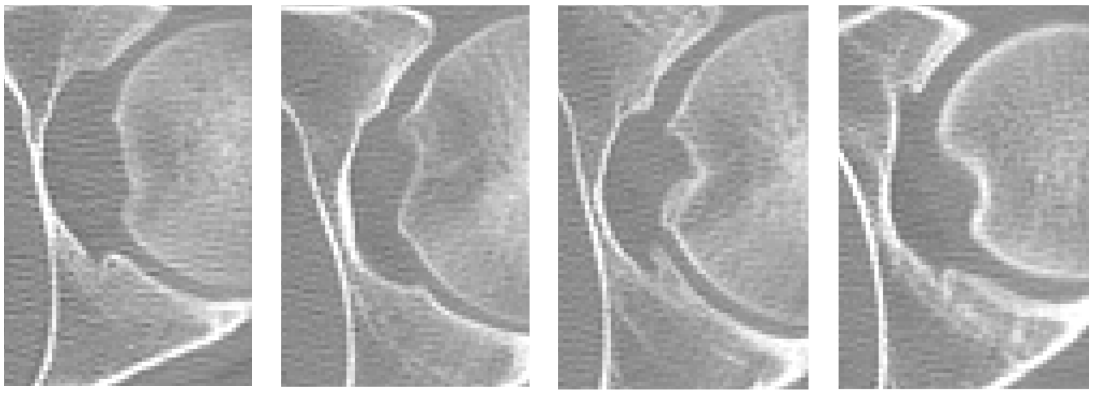

*Figure 5.4: Various shapes of the femur head's fovea*

Finally, Figure 5.4 ilustrates a wide array of foveas. Some of which are nearly straight, other are angular concavities while others still appear as deep dimples.

## 5.3 Experimental Setup

As for parameters used during the pre-processing step, we started off with an *upscale factor* of **2**. The resolutions of the resized-slices were sufficiently large that the evolving snake was better able to map the concavities on the interior of the greater trochanter. In addition, the upscale factor gave a nicer edge to some of the sharp turns in the femur head's exterior.

During the acetabular removal step, we used a threshold value of **172** to highlight voxels which belonged to the acetabulum's hard shell. Prior to the volume's conversion from Hounsfield Units, this value would roughly have corresponded to 316 HU. Across all six CT scans, we found that this value did well to emphasize the acetabulum's bones without accidentally accentuating the voxels for soft-tissue between the acetabulum and femur head.

We used a threshold value of **159** during the ceiling threshold step to highlight voxels corresponding to compact osseous tissue. Once again, prior to the volume's conversion from Hounsfield Units, this value would roughly have corresponded to 201 HU. Similarly, we identified through testing across our six CT scan samples that this threshold is the lowest obtainable without inadvertently introducing high-intensity noise into the slice.

After some experimentation, we discovered that lowering the ceiling threshold for the top-most slices of the femur head would occasionally improve results. For this reason we use a threshold value of **151** for the top-most 25% of slices above the primer slice. This accounts for the top-most 12.5% of the whole femur head ROI.

The *rough* and the *fine* contour extractions methods use two different sets of procedures, as well as input parameters. The *rough* method uses a threshold value to determine whether dilations or erosions are performed whereas the *fine* method uses an interval value of the image. The parameters for the former can be found in Table 5.5 and the latter in Table 5.6.

*Table 5.5: Test parameters for Morphological snake with edge-threshold-balloon (Rough Contours)*

| **σ** | **N** | **ETB** | **EDT** |
|---|---|---|---|
| 0.0 | 100 | 0.1 | 1.000 |

*Table 5.6: Test parameters for morphological snake with snake-balloon-difference-radius (Fine Contours)*

| **σ** | **N** | **DR** | **EDT** |
|---|---|---|---|
| 0.0 | 100 | 12 | 0.001 |

For these parameters, *G(I)* is the level-set method the contours are trying to minimize, $\sigma$ is the standard deviation of the Gaussian convolution applied to the original image, *N* is the maximum number of iterations, *EDT* is the threshold for G(I) during the speed propagation procedure, *ETB* is the threshold for G(I) during the balloon propagation procedure, and *DR* is the difference magnitude with respect to the central pixel value that propagates the balloon.

## 5.4 Segmentation Qualitative Results

The images below originate from patient #3; a female patient diagnosed with a cam impingement in her left hip. The CT scan on which the images are based is composed of 126 slices which spanned from the top of the patient's sacrum to the roughly a 1cm below her minor trochanters.

A side-by-side comparison of segmentation results obtained through our method and those obtained though manual segmentation can be seen in Table 5.7 for the femur head and Table 5.8 for the femur body. The femur used in the test was formally diagnosed with a cam impingement.

*Table 5.7: Comparison of our segmentation method results for the femur head with those from a manual segmentation*

| | Our Segmentation | Manual Segmentation | Difference |
|---|---|---|---|
| Head Top | 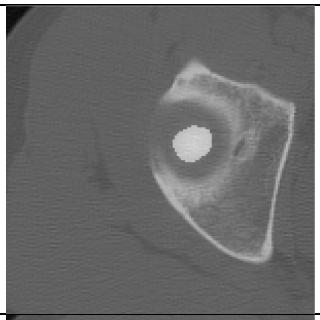 | 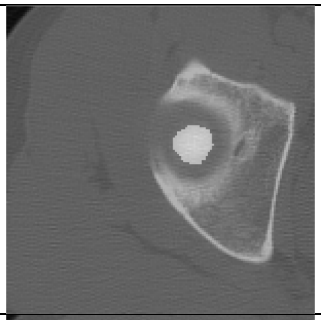 | 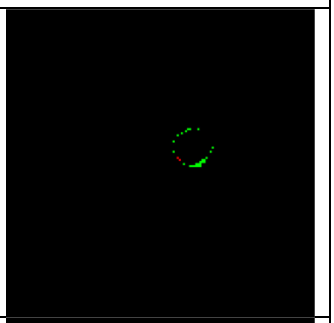 |
| Mid Head | 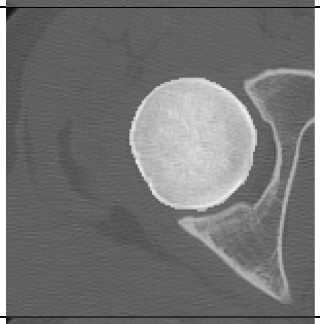 | 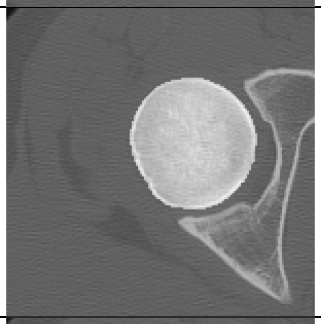 | 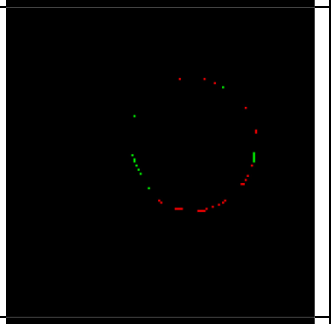 |
| Upper Greater Troch |  |  | 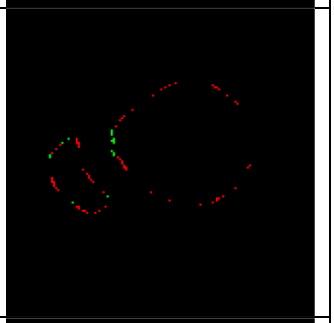 |
| Lower-Head |  | 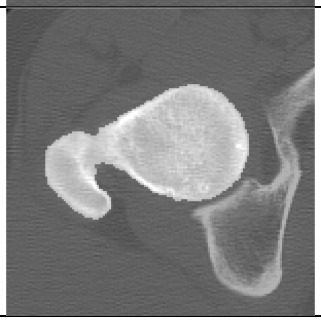 | 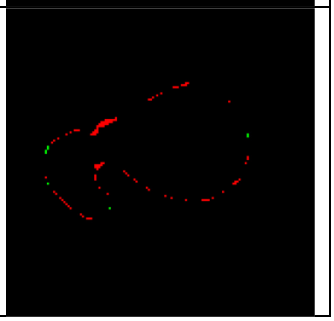 |

The left column contains the interior of our method's final contour for a particular slice. Voxels which are detected by our method to be part of the femur are highlighted in white.

The middle column contains the volume which is considered the target segmentation. Volume highlighted in white was manually segmented on a slice-by-slice, voxel-by-voxel basis with an image editing program.

*Table 5.8: Comparison of our segmentation method results for the femur body with those from a manual segmentation*

| | Our Segmentation | Manual Segmentation | Difference |
|---|---|---|---|
| Mid Greater Troch. | 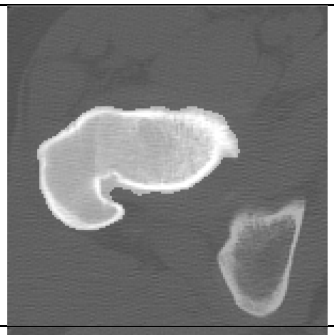 | 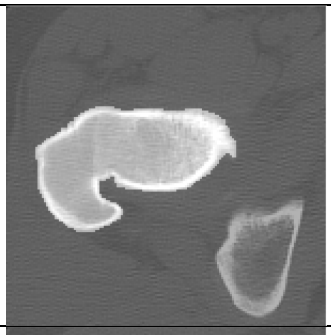 | 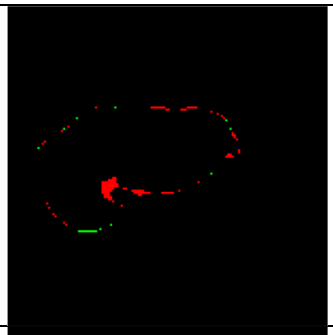 |
| Lower Greater Troch. | 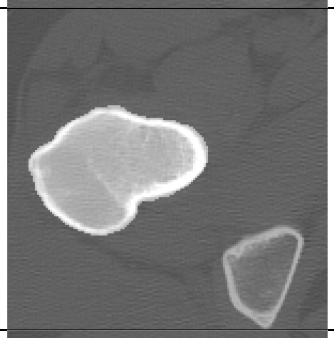 | 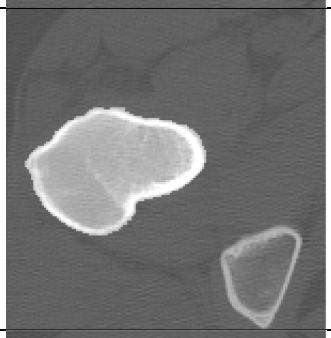 | 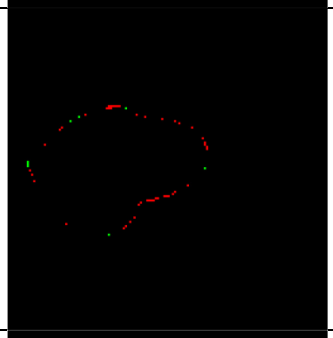 |
| Minor Troch | 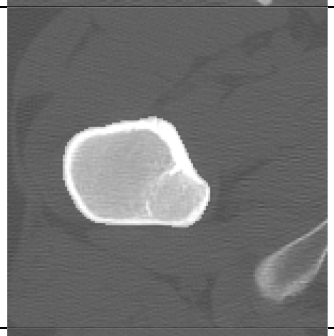 | 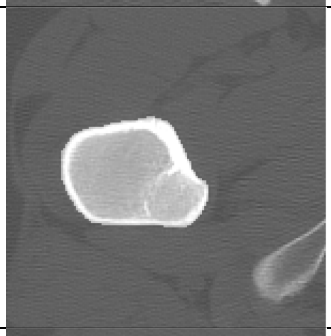 | 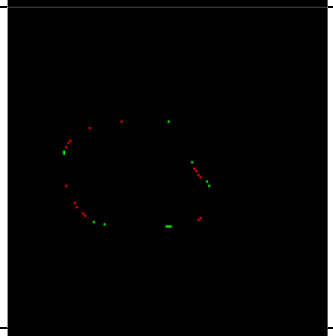 |
| Femur Body | 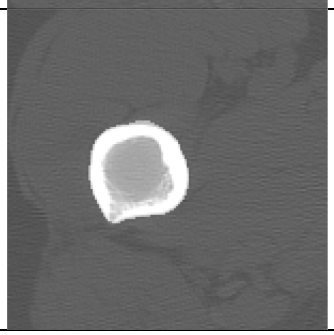 | 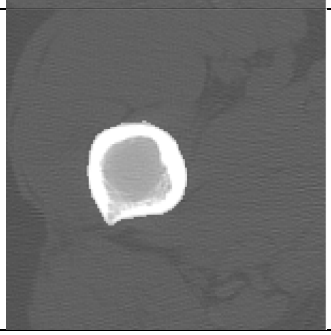 | 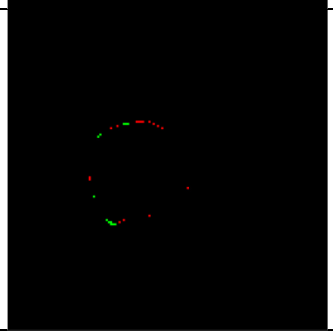 |

The right column shows how well these two segmentations overlap. Voxels shown in *black* indicate identical results for both segmentations. Green voxels indicated voxels which were a

member of the manual segmentation but not of our algorithmic segmentation while *red* voxels indicate the opposite.

Table 5.9, Table 5.10, Table 5.11, Table 5.12, Table 5.13 and Table 5.14 shows 3D renderings of the segmented femurs for each of our six sample patients. The first row of each table contains the renderings of femurs segmented with our method while the second row contains renderings from manually segmented femurs. On the same tables, the first two columns show projections of the patient's left femur while the second two columns show projections of the right femur. Both the first and third column and taken from an antero-posterior (AP) position. The second column's renderings are taken, starting from the AP position, 135° right, around the patient's trunk. Likewise, the fourth column's renderings are taken, starting from the AP position, 135° left, around the patient's trunk.

These rendering obtained through the following steps:

1. Label the voxels in or segmented volumes as '1' if belonging to a femur and '0' otherwise
2. Multiply the labels of each voxel from our segmented volumes with the original intensities of the corresponding voxels in the CT scan to produce a third, *filtered* volume
3. Render the filtered volume using a volume raycasting method to produce a 2D projection
4. Pixels in the 2D projection which were completely black, indicating regions outside the segmented volume, were replaced with white in order to provide a sharper outline to the femur's

The technique [64] used to produce the 2D projections is an example of a Digitally Reconstructed Radiograph (DRR) [65]. DRRs are an approximation of a 2D x-ray image obtained from CT or MRI data. A DRR's semi-transparent approach to volume rendering allows more depth to be presented compared to surface models.

*Table 5.9: Comparison of Volumetric Models for Patient #1*

| | AP of Left Femur | Rear-Lateral of Left Femur | AP of Right Femur | Rear-Lateral of Right Femur |
|---|---|---|---|---|
| Our Model |  |  |  |  |
| Manual Model |  |  |  |  |

*Table 5.10: Comparison of Volumetric Models for Patient #2*

| | AP of Left Femur | Rear-Lateral of Left Femur | AP of Right Femur | Rear-Lateral of Right Femur |
|---|---|---|---|---|
| Our Model |  |  |  |  |
| Manual Model |  |  |  |  |

*Table 5.11: Comparison of Volumetric Models for Patient #3*

| | AP of Left Femur | Rear-Lateral of Left Femur | AP of Right Femur | Rear-Lateral of Right Femur |
|---|---|---|---|---|
| Our Model |  |  |  |  |
| Manual Model |  |  |  |  |

*Table 5.12: Comparison of Volumetric Models for Patient #4*

| | AP of Left Femur | Rear-Lateral of Left Femur | AP of Right Femur | Rear-Lateral of Right Femur |
|---|---|---|---|---|
| Our Model |  |  |  | 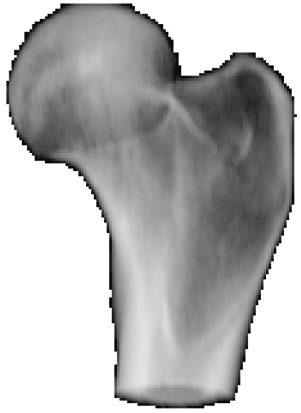 |
| Manual Model |  | 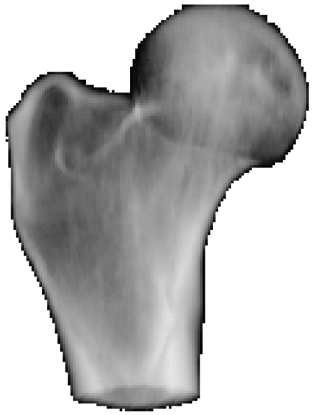 |  | 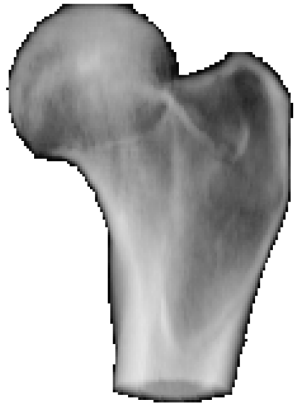 |

*Table 5.13: Comparison of Volumetric Models for Patient #17*

| | AP of Left Femur | Rear-Lateral of Left Femur | AP of Right Femur | Rear-Lateral of Right Femur |
|---|---|---|---|---|
| Our Model |  |  |  |  |
| Manual Model |  | 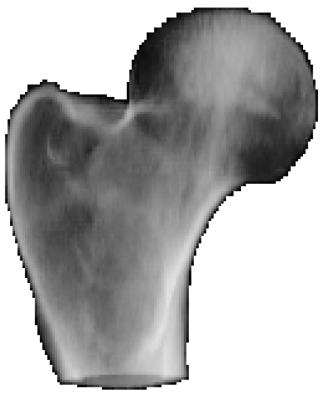 |  |  |

*Table 5.14: Comparison of Volumetric Models for Patient #20*

| | AP of Left Femur | Rear-Lateral of Left Femur | AP of Right Femur | Rear-Lateral of Right Femur |
|---|---|---|---|---|
| Our Model |  |  |  |  |
| Manual Model |  |  |  |  |

## 5.5 Segmentation Quantitative Results

In order to further validate our results, we sought to gather commonly used [66] segmentation statistics which we could use to compare our strategy against those which have been previously described. These statistics can either be described as volume-based or boundary-based or metrics.

**Volume-Based Metrics**

Given volumetric models of the same femur, *VM* and *VA* (the manually segmented and automatically segmented models respectively), we can overlap the two volumes to derive an overall measure of the correspondence between of the two volumes. We calculate the *Volumetric Overlap* (VO) as the number of voxels in the intersection of the automatic and manual models divided by the number of voxels in the union of the automatic and manual models. The volumetric overlap will have values that range from be 1 (a perfect segmentation) to 0 (no overlap at all).

Conversely, the *Volumetric Overlap Error* (VOE) is the measure of the overall difference between two volumes. It is obtained by subtracting the VO from 1. During testing we calculated the VOE for both individual slices (Eq. 5.1) and the global model (Eq. 5.2). Much like VOs, VOEs are measured in per-cents.

$$VOE_s = 1 - \frac{|VM_s \cap VA_s|}{|VM_s \cup VA_s|} \quad \text{Eq. 5.1}$$

$$VOE_g = 1 - \frac{\sum_{s=1}^{z}|VM_s \cap VA_s|}{\sum_{s=1}^{z}|VM_s \cup VA_s|} \quad \text{Eq. 5.2}$$

**Boundary-Based Metrics**

We initiate this second set of metrics by reducing the volumetric models into their shell equivalents. For each slice in a volume, we determine the *border voxels* of the segmentations.

These are defined as any voxels belonging to the object which have at least one neighbour that does not belong to the object. To maintain a clean boundary, an object voxel $V_{x,y,z}$ will have its searched neighbourhood restricted to the voxels $V_{x-1,y,z}$ , $V_{x+1,y,z}$ , $V_{x,y-1,z}$ and $V_{x,y+1,z}$ . We refer to the newly created shells of the volumetric models as $B_M$ and $B_A$; the boundaries for the manually and automatically segmented models respectively.

With our new models comes a new metric to measure our method's accuracy; *symmetric surface distance* (SSD). For each voxel in $B_M$, the closest voxel in $B_A$ is determined using Euclidean, real world distance. This method takes into account the generally different resolutions in the different scan directions.

At each step in our quantitative evaluation, we report four different types of the SSD-based measurements:

1. **Minimum Symmetric Surface Distance** ($SSD_{min}$) – For this measure, of all the SSD for voxels in a slice/volume, the *minimum* distance is selected. We obtain our $SSD_{min}$ values with Eq. 5.3, where X is the voxel in $B_M$ which has the minimum distance to its nearest-neighbour voxel (Y) in BA.
2. **Maximum Symmetric Surface Distance** ($SSD_{max}$) – For this measure, of all the SSD for voxels in a slice/volume, the *maximum* distance is selected. We obtain our $SSD_{max}$ values with Eq. 5.4, where X is the voxel in $B_M$ which has the maximum distance to its nearest-neighbour voxel (Y) in BA.
3. **Average Symmetric Surface Distance for the global model** ($SSD_{g.avg}$) - For this measure, the *average* of all the SSDs of the voxels in a *volume* is calculated. We obtain our $SSD_{g.avg}$ values with Eq. 5.5, where $n$ is the number of border voxels in $B_M$, and $X_i$ is one of the border voxels in $B_M$ , whose nearest neighbouring border voxel in $B_A$ is $Y$

4. **Average Symmetric Surface Distance for individual slices** ($SSD_{s.avg}$) - For this measure, the *average* of all the SSDs of the voxels in a *slice* is calculated. We obtain our $SSD_{s.avg}$ values with Eq. 5.6, where $B_{Mz}$ is the set of all border voxels for slice $_z$ in $B_M$, $n$ is the number of border voxels in $B_{Mz}$, and $X_i$ is one of the border voxels in $B_{Mz}$, whose nearest neighbouring border voxel in $B_A$ is $Y$

$$SSD_{min} = \min_{X \in B_M} \min_{Y \in B_A} dist(X,Y) \quad \text{Eq. 5.3}$$

$$SSD_{max} = \max_{X \in B_M} \min_{Y \in B_A} dist(X,Y) \quad \text{Eq. 5.4}$$

$$SSD_{g.avg} = \frac{\sum_{i=1}^{n} \left( Xi \in B_M \min_{Y \in B_A} dist(X_i, Y) \right)}{n} \quad \text{Eq. 5.5}$$

$$SSD_{s.avg} = \frac{\sum_{i=1}^{n} \left( Xi \in B_{Mz} \min_{Y \in B_A} dist(X_i, Y) \right)}{n} \quad \text{Eq. 5.6}$$

The results for $SSD_{min}$, $SSD_{max}$, and $SSD_{g.avg}$, $SSD_{s.avg}$ are all measured in millimeters. The lowest possible value for all four of these measurements is 0, which indicates a perfectly overlapping border.Table 5.15 is the first to display quantitative results for our method. It contains the voxel overlap errors for both femurs of all six of our sample patients. For each femur, the table's columns report the $VOE_g$, *average* $VOE_s$ of every slice in the segmentation, the *minimum* $VOE_s$ of every slice in the segmentation, and the *maximum* $VOE_s$ of every slice in the segmentation. Each one of these measurements is listed in *percent* error.

*Table 5.15: Voxel Overlap Errors for each femur*

| Patient # | Side | $VOE_g$ (%) | $VOE_s$ Avg. ± stdev (%) | $VOE_s$ Min (%) | $VOE_s$ Max(%) |
|---|---|---|---|---|---|
| 1 | Left | 2.51 | 3.36 ± 6.57 | 0.80 | 58.80 |
| | Right | 2.84 | 3.88 ± 8.21 | 0.84 | 71.30 |
| 2 | Left | 2.90 | 3.79 ± 5.84 | 1.11 | 48.61 |
| | Right | 3.14 | 3.99 ± 5.60 | 1.23 | 48.17 |
| 3 | Left | 2.22 | 2.42 ± 1.75 | 0.86 | 9.89 |
| | Right | 2.18 | 2.51 ± 2.42 | 0.62 | 19.38 |
| 4 | Left | 3.26 | 3.38 ± 1.77 | 0.68 | 9.94 |
| | Right | 3.54 | 3.92 ± 1.91 | 1.75 | 16.59 |
| 16 | Left | 2.41 | 3.59 ± 8.94 | 0.74 | 77.38 |
| | Right | 2.27 | 3.12 ± 6.00 | 0.87 | 52.47 |
| 17 | Left | 2.62 | 2.76 ± 1.85 | 1.24 | 13.41 |
| | Right | 2.67 | 2.88 ± 2.18 | 1.28 | 16.06 |
| **Femur Average** | | 2.71 ± 0.44 | 3.30 ± 0.56 | 1.00 ± 0.33 | 36.84 ± 25.17 |

Table 5.16 contains symmetrical surface distances for both femurs of all six of our sample patients. These SSDs are obtained by *not restricting* the elements of $B_A$ by slice. For each femur, the table's columns report the $SSD_{g.avg}$, $SSD_{s.avg}$, $SSD_{min}$, $SSD_{g.avg}$. Each one of these measurements is listed in millimetres.

*Table 5.16: Symmetric Surface Distances with no slice restriction on Y*

| | | **3D** | | | |
|---|---|---|---|---|---|
| **Patient #** | **Side** | **$SSD_{g.avg}$ ± stdev (mm)** | **$SSD_{s.avg}$ Avg. ± stdev (mm)** | **$SSD_{min}$ (mm)** | **$SSD_{max}$ (mm)** |
| 1 | Left | 0.26 ± 0.42 | 0.29 ± 0.27 | 0.00 | 4.83 |
| | Right | 0.29 ± 0.46 | 0.33 ± 0.44 | 0.00 | 6.30 |
| 2 | Left | 0.28 ± 0.41 | 0.31 ± 0.25 | 0.00 | 3.49 |
| | Right | 0.30 ± 0.44 | 0.32 ± 0.22 | 0.00 | 4.32 |
| 3 | Left | 0.23 ± 0.38 | 0.22 ± 0.11 | 0.00 | 2.76 |
| | Right | 0.22 ± 0.37 | 0.22 ± 0.11 | 0.00 | 2.76 |
| 4 | Left | 0.31 ± 0.43 | 0.30 ± 0.12 | 0.00 | 3.42 |
| | Right | 0.37 ± 0.40 | 0.37 ± 0.09 | 0.00 | 3.16 |
| 16 | Left | 0.26 ± 0.45 | 0.31 ± 0.51 | 0.00 | 7.36 |
| | Right | 0.25 ± 0.42 | 0.28 ± 0.33 | 0.00 | 4.93 |
| 17 | Left | 0.29 ± 0.38 | 0.29 ± 0.13 | 0.00 | 2.16 |
| | Right | 0.29 ± 0.39 | 0.29 ± 0.14 | 0.00 | 2.50 |
| **Femur Average** | | 0.28 ± 0.04 | 0.29 ± 0.04 | 0.00 ± 0.00 | 4.00 ± 1.60 |

Table 5.16 contains symmetrical surface distances for both femurs of all six of our sample patients. These SSDs are obtained by *restricting* the elements of $B_A$ to only contain border voxels sharing the same slice as *X*. For each femur, the table's columns report the $SSD_{g.avg}$, $SSD_{s.avg}$, $SSD_{min}$, $SSD_{g.avg}$. Each one of these measurements is listed in millimetres.

*Table 5.17: Symmetric Surface Distances with Y restricted to the same slice as X*

| | | 2D | | | |
|---|---|---|---|---|---|
| **Patient #** | **Side** | **$SSD_{g.avg}$ ± stdev (mm)** | **$SSDs_{.avg}$ ± stdev (mm)** | **$SSD_{min}$ (mm)** | **$SSD_{max}$ (mm)** |
| 1 | Left | 0.28 ± 0.46 | 0.30 ± 0.30 | 0.00 | 4.83 |
| | Right | 0.30 ± 0.52 | 0.35 ± 0.46 | 0.00 | 6.30 |
| 2 | Left | 0.28 ± 0.43 | 0.31 ± 0.26 | 0.00 | 3.49 |
| | Right | 0.31 ± 0.48 | 0.33 ± 0.22 | 0.00 | 4.32 |
| 3 | Left | 0.24 ± 0.46 | 0.23 ± 0.13 | 0.00 | 8.57 |
| | Right | 0.23 ± 0.41 | 0.23 ± 0.12 | 0.00 | 5.21 |
| 4 | Left | 0.33 ± 0.50 | 0.32 ± 0.14 | 0.00 | 6.30 |
| | Right | 0.37 ± 0.41 | 0.38 ± 0.10 | 0.00 | 4.59 |
| 16 | Left | 0.27 ± 0.49 | 0.33 ± 0.53 | 0.00 | 7.36 |
| | Right | 0.26 ± 0.45 | 0.29 ± 0.34 | 0.00 | 4.93 |
| 17 | Left | 0.29 ± 0.39 | 0.29 ± 0.14 | 0.00 | 2.90 |
| | Right | 0.29 ± 0.41 | 0.29 ± 0.14 | 0.00 | 3.06 |
| **Femur Average** | | 0.29 ± 0.04 | 0.30 ± 0.04 | 0.00 ± 0.00 | 5.16 ± 1.72 |

Table 5.18 presents a slice-by-slice case study of the VOEs and SSDs of a single femur. The CT scan from which the femur was segmented contained 106 slices, the femur first appears in slice 33, where the crown of the femur head emerges. The femur is cut-off by the end of the CT scan on slice 106, which is roughly 3-5 mm below the bottom of the minor trochanter.

*Table 5.18: Slice-by-slice case study of qualitative results obtained for Patient #2's left femur*

| **Slice #** | **$VOE_s$ (%)** | 2D | | | 3D | | |
|---|---|---|---|---|---|---|---|
| | | **$SSD_{s.avg}$ ± stdev (mm)** | **$SSD_{min}$ (mm)** | **$SSD_{max}$ (mm)** | **$SSD_{s.avg}$ ± stdev (mm)** | **$SSD_{min}$ (mm)** | **$SSD_{max}$ (mm)** |
| 33[1] | 48.61 | 2.11 ± 0.87 | 0.68 | 3.46 | 2.11 ± 0.87 | 0.68 | 3.49 |
| 34 | 12.02 | 0.59 ± 0.41 | 0 | 1.53 | 0.59 ± 0.41 | 0.00 | 1.53 |
| 35 | 18.36 | 1.05 ± 0.61 | 0 | 2.47 | 0.97 ± 0.50 | 0.00 | 1.85 |
| 36 | 11.20 | 0.76 ± 0.45 | 0 | 1.53 | 0.74 ± 0.43 | 0.00 | 1.37 |
| 37 | 9.34 | 0.74 ± 0.48 | 0 | 1.93 | 0.72 ± 0.45 | 0.00 | 1.93 |

| | | | | | | | |
|---|---|---|---|---|---|---|---|
| 38 | 6.76 | 0.56 ± 0.46 | 0 | 1.53 | 0.55 ± 0.44 | 0.00 | 1.43 |
| 39 | 3.92 | 0.34 ± 0.42 | 0 | 1.53 | 0.34 ± 0.41 | 0.00 | 1.37 |
| 40 | 4.27 | 0.40 ± 0.48 | 0 | 1.93 | 0.39 ± 0.44 | 0.00 | 1.37 |
| 41 | 3.18 | 0.33 ± 0.37 | 0 | 1.37 | 0.32 ± 0.37 | 0.00 | 1.25 |
| 42 | 4.24 | 0.43 ± 0.44 | 0 | 1.37 | 0.43 ± 0.43 | 0.00 | 1.37 |
| 43 | 2.59 | 0.29 ± 0.40 | 0 | 1.37 | 0.29 ± 0.39 | 0.00 | 1.37 |
| 44 | 2.35 | 0.27 ± 0.37 | 0 | 1.53 | 0.27 ± 0.37 | 0.00 | 1.42 |
| 45 | 2.42 | 0.27 ± 0.40 | 0 | 1.37 | 0.27 ± 0.40 | 0.00 | 1.37 |
| 46 | 1.63 | 0.19 ± 0.35 | 0 | 1.37 | 0.19 ± 0.34 | 0.00 | 1.37 |
| 47 | 1.85 | 0.22 ± 0.36 | 0 | 1.37 | 0.22 ± 0.36 | 0.00 | 1.37 |
| 48 | 2.29 | 0.27 ± 0.35 | 0 | 1.37 | 0.27 ± 0.35 | 0.00 | 1.37 |
| 49 | 1.85 | 0.23 ± 0.36 | 0 | 1.53 | 0.23 ± 0.36 | 0.00 | 1.53 |
| 50[2] | 3.05 | 0.30 ± 0.39 | 0 | 1.93 | 0.30 ± 0.38 | 0.00 | 1.93 |
| 51[3] | 3.29 | 0.31 ± 0.40 | 0 | 1.37 | 0.31 ± 0.40 | 0.00 | 1.37 |
| 52 | 2.34 | 0.24 ± 0.34 | 0 | 1.37 | 0.24 ± 0.34 | 0.00 | 1.37 |
| 53 | 3.16 | 0.28 ± 0.43 | 0 | 2.73 | 0.26 ± 0.38 | 0.00 | 1.42 |
| 54 | 2.21 | 0.23 ± 0.33 | 0 | 1.37 | 0.23 ± 0.33 | 0.00 | 1.37 |
| 55[4] | 2.33 | 0.25 ± 0.34 | 0 | 0.97 | 0.25 ± 0.34 | 0.00 | 0.97 |
| 56 | 2.16 | 0.24 ± 0.34 | 0 | 0.97 | 0.24 ± 0.34 | 0.00 | 0.97 |
| 57 | 1.87 | 0.21 ± 0.32 | 0 | 0.97 | 0.21 ± 0.32 | 0.00 | 0.97 |
| 58 | 2.70 | 0.30 ± 0.40 | 0 | 1.93 | 0.30 ± 0.39 | 0.00 | 1.93 |
| 59 | 1.73 | 0.19 ± 0.31 | 0 | 0.68 | 0.19 ± 0.31 | 0.00 | 0.68 |
| 60 | 2.93 | 0.32 ± 0.48 | 0 | 2.73 | 0.30 ± 0.41 | 0.00 | 1.43 |
| 61 | 1.99 | 0.23 ± 0.33 | 0 | 1.37 | 0.23 ± 0.33 | 0.00 | 1.37 |
| 62 | 3.60 | 0.39 ± 0.47 | 0 | 2.16 | 0.38 ± 0.44 | 0.00 | 1.53 |
| 63 | 2.72 | 0.28 ± 0.39 | 0 | 1.53 | 0.28 ± 0.39 | 0.00 | 1.43 |
| 64 | 3.62 | 0.37 ± 0.48 | 0 | 2.05 | 0.37 ± 0.47 | 0.00 | 1.85 |
| 65[5] | 4.22 | 0.43 ± 0.55 | 0 | 2.82 | 0.41 ± 0.48 | 0.00 | 1.85 |
| 66 | 4.19 | 0.44 ± 0.50 | 0 | 2.47 | 0.42 ± 0.45 | 0.00 | 1.58 |
| 67 | 2.47 | 0.27 ± 0.39 | 0 | 1.37 | 0.27 ± 0.39 | 0.00 | 1.37 |
| 68 | 2.46 | 0.32 ± 0.49 | 0 | 2.73 | 0.31 ± 0.45 | 0.00 | 2.40 |
| 69 | 1.80 | 0.21 ± 0.34 | 0 | 1.37 | 0.21 ± 0.33 | 0.00 | 1.25 |
| 70[6] | 1.71 | 0.19 ± 0.33 | 0 | 1.37 | 0.19 ± 0.33 | 0.00 | 1.37 |
| 71 | 2.03 | 0.23 ± 0.35 | 0 | 1.37 | 0.23 ± 0.35 | 0.00 | 1.25 |
| 72 | 1.39 | 0.16 ± 0.29 | 0 | 0.68 | 0.16 ± 0.29 | 0.00 | 0.68 |
| 73 | 1.45 | 0.17 ± 0.30 | 0 | 0.97 | 0.17 ± 0.30 | 0.00 | 0.97 |
| 74 | 1.57 | 0.18 ± 0.31 | 0 | 0.97 | 0.18 ± 0.31 | 0.00 | 0.97 |
| 75 | 2.15 | 0.24 ± 0.35 | 0 | 1.37 | 0.24 ± 0.35 | 0.00 | 1.25 |
| 76 | 1.11 | 0.13 ± 0.27 | 0 | 0.68 | 0.13 ± 0.27 | 0.00 | 0.68 |
| 77 | 2.78 | 0.31 ± 0.46 | 0 | 2.05 | 0.29 ± 0.42 | 0.00 | 1.37 |
| 78 | 1.56 | 0.18 ± 0.30 | 0 | 0.68 | 0.18 ± 0.30 | 0.00 | 0.68 |
| 79 | 2.14 | 0.24 ± 0.33 | 0 | 0.97 | 0.24 ± 0.33 | 0.00 | 0.97 |
| 80 | 2.25 | 0.24 ± 0.34 | 0 | 1.37 | 0.24 ± 0.34 | 0.00 | 1.37 |
| 81 | 1.78 | 0.19 ± 0.30 | 0 | 0.68 | 0.19 ± 0.31 | 0.00 | 0.68 |
| 82 | 2.02 | 0.21 ± 0.34 | 0 | 1.37 | 0.21 ± 0.34 | 0.00 | 1.37 |

| | | | | | | | |
|---|---|---|---|---|---|---|---|
| 83 | 2.41 | 0.24 ± 0.39 | 0 | 1.53 | 0.24 ± 0.35 | 0.00 | 1.43 |
| 84 | 1.96 | 0.19 ± 0.34 | 0 | 1.37 | 0.19 ± 0.34 | 0.00 | 1.37 |
| 85 | 3.34 | 0.32 ± 0.50 | 0 | 2.05 | 0.31 ± 0.46 | 0.00 | 1.43 |
| 86 | 2.56 | 0.24 ± 0.38 | 0 | 1.37 | 0.24 ± 0.38 | 0.00 | 1.37 |
| 87 | 2.71 | 0.25 ± 0.43 | 0 | 1.37 | 0.25 ± 0.43 | 0.00 | 1.37 |
| 88 | 4.78 | 0.43 ± 0.74 | 0 | 3.42 | 0.38 ± 0.58 | 0.00 | 2.30 |
| 89 | 3.00 | 0.27 ± 0.46 | 0 | 2.05 | 0.27 ± 0.45 | 0.00 | 1.85 |
| 90 | 2.54 | 0.24 ± 0.37 | 0 | 1.37 | 0.24 ± 0.37 | 0.00 | 1.37 |
| 91[7] | 2.80 | 0.24 ± 0.42 | 0 | 1.37 | 0.23 ± 0.41 | 0.00 | 1.37 |
| 92 | 3.04 | 0.26 ± 0.41 | 0 | 1.53 | 0.26 ± 0.40 | 0.00 | 1.43 |
| 93 | 2.75 | 0.24 ± 0.39 | 0 | 1.93 | 0.23 ± 0.38 | 0.00 | 1.43 |
| 94 | 1.99 | 0.18 ± 0.30 | 0 | 0.68 | 0.18 ± 0.30 | 0.00 | 0.68 |
| 95 | 2.15 | 0.17 ± 0.34 | 0 | 1.37 | 0.17 ± 0.34 | 0.00 | 1.37 |
| 96 | 3.03 | 0.25 ± 0.47 | 0 | 2.05 | 0.24 ± 0.42 | 0.00 | 1.53 |
| 97 | 2.23 | 0.19 ± 0.35 | 0 | 1.37 | 0.19 ± 0.34 | 0.00 | 1.37 |
| 98 | 2.48 | 0.21 ± 0.33 | 0 | 0.97 | 0.21 ± 0.33 | 0.00 | 0.97 |
| 99 | 3.04 | 0.25 ± 0.39 | 0 | 1.53 | 0.25 ± 0.39 | 0.00 | 1.53 |
| 100 | 2.42 | 0.20 ± 0.36 | 0 | 1.53 | 0.20 ± 0.36 | 0.00 | 1.43 |
| 101 | 3.14 | 0.25 ± 0.37 | 0 | 1.37 | 0.25 ± 0.37 | 0.00 | 1.25 |
| 102 | 2.52 | 0.20 ± 0.33 | 0 | 1.37 | 0.20 ± 0.33 | 0.00 | 1.37 |
| 103 | 2.00 | 0.15 ± 0.29 | 0 | 0.68 | 0.15 ± 0.29 | 0.00 | 0.68 |
| 104 | 2.66 | 0.21 ± 0.32 | 0 | 0.68 | 0.21 ± 0.32 | 0.00 | 0.68 |
| 105 | 2.39 | 0.18 ± 0.30 | 0 | 0.97 | 0.18 ± 0.30 | 0.00 | 0.97 |
| 106[8] | 3.21 | 0.24 ± 0.41 | 0 | 1.53 | 0.24 ± 0.39 | 0.00 | 1.37 |

[1] Top the femur head
[2] The top of the greater trochanter first appear as a separate object to the femur head
[3] Midsection of the femur head
[4] The Greater Trochanter and femur head first join as a single object
[5] Bottom of the femur head
[6] Bottom of the greater trochanter
[7] Midsection of the minor trochanter
[8] End of the CT scan

## 5.6 Results Evaluation and Discussion

### 5.6.1 Segmentation Process

The user initialization and automated segmentation of out method were performed on the same, modern desktop computer (Intel i7 processor with 4 cores running 2.67 GHz, 6GB of DRR3 RAM running at Windows 7 64bit Operating System). The start-to-finish time required to segment a single femur using our method can differ from patient to patient, depending on the

size of the CT scan, scan resolution, size of the femur, etc. However, during our testing the time required for each individual step could be expected to follow the estimated found in Table 5.19.

*Table 5.19: Time estimates for individual steps in our method's segmentation process*

| Task | Time Estimate |
|---|---|
| Manually setting ROIs, a femur head center and split-slice index | 1 minute |
| Automated acetabular removal | ~ 5 seconds |
| Automated femur-head segmentation | < 5 minutes |
| Automated femur-body segmentation | < 5 minutes |
| Automated merging of the two segmentations | Under 1 second |

The largest contributor to our method's computation time was the automated femur head and body segmentations steps. This can be traced back to the multiple applications of the comparatively computationally intensive morphological snake algorithm. In addition, the morphological snake processing time is greatly magnified by decision to upscale the slices. It's worth mentioning that our segmentation strategy has primarily been optimized for good results and not fast execution. Many strategies exists which could further reduce our solution's running time, such as multi-threading, GPU acceleration and using a unified image/curvature scheme throughout the program which would eliminate the frequent format conversions between the segmentation module and the visualisation module.

Of the six patients, one required minor manual correction of the curve's evolution. The voxels which compose patient #1's femur head were noticeably darker than any other patient's, which caused the snake's curve to intrude into the femur head's interior on curtain slices.

### 5.6.2 Qualitative Results

Looking at Table 5.7 and Table 5.8 provides us with some general insight into the our methods performance. Our segmentation strategy returns contours which are quite close to the

target manual segmentations, often differing by 1 voxel of less. The majority of regions where the two contours differ can be attributed to our automated solution being a little thicker than the manual segmentation. This can likely be attributed to the ceiling threshold value used in pre-processing being higher than necessary for most slices. This effect could be reduced by using a custom or adaptive ceiling threshold for each individual slice.

When the two contours differed greatly, it could be expected to be in one of three regions: narrow pits of greater trochanters, the bottom-most slice of the femur head, and the top-most slices of the femur head.

In the cases where a patient's femur has a narrow pit at the greater trochanter, the snake's curve is often unable to trace the interior of the concavity fully. This issue is native to most snake segmentation schemes and can be attributed to the external forces acting on the evolving contour cancelling each other out when inside narrow concavities [27]. Possible fixes to this shortcoming include increasing the upscale factor during the pre-processing phase or to alter the external force model to better carry the flow of gradients.

The bottom-most and top-most slice of the femur head are sources of error for the same reason: blurriness of contour. Normally, a femur's contours can be traced with the help of its high-intensity shell of compact bone. Unfortunately, at the top and the slope below of the femur head, the shell's voxel intensity becomes lower; the edges become feathered and harder to distinguish from noise. These blurred edges also introduce complications during manual segmentation, where the exact boundaries can't be determined with single-voxel precision. During our experimentation, region-based segmentation schemes were employed in an attempt to improve results for slices with blurred edges, but the contours they returned were less reliable than our current methods.

### 5.6.3 Quantitative Results

The overall femur averages from Table 5.15 show the $VOE_g$ (2.71 ± 0.44%), $VOE_s$ Average (3.30 ± 0.56%) and $VOE_s$ Minimum (1.00 ± 0.33%) were all quite low. However, the average $VOE_s$ maximum (36.84 ± 25.17%) shows a staggering difference. The origin of the $VOE_s$ maximum was the same for every femur: the top-most slice. As previously remarked, the top-most slices of the femur-head have blurred, noisy contours which makes it difficult for the evolving snake to find the desired halting location. The lack of sharp, well define contours can lead to wildly incorrect final segmentations, which is epitomized in the top-most slice of the femur head, and often also represented in the slices adjacent to the top-most slice. This can be seen in our case study, Table 5.18, where the topmost slice has as $VOE_s$ of 48.61%, and the following four slices span from 18.36 to 9.34%.

The last row of Table 5.16 shows an average of the symmetric surface distances for our segmented femurs, listing a SSDg.avg (0.28 ± 0.04mm), SSDs.avg Average (0.29 ± 0.04mm) and $SSD_{min}$ (0.00 ± 0.00mm) which were well under a single voxel's distance (0.68mm). The average femur $SSD_{max}$ on the other hand was listed at 4.00 ± 1.60mm, and is listed even higher (Table 5.17) when the neighbour search space is flattened. Generally, the voxel attributed to the $SSD_{max}$ could be expected to be found in one of three places: the top of the femur head, the bottom of the femur head, or in the pit of the greater trochanter. Errors associated with the femur-head's extremes are due to previously mentioned blurred femoral contours. Errors, associated with the pit next to the greater trochanter emerge when the region between the femur greater trochanter and femoral neck is narrow, causing a snake to stop evolving at the pit's entrance, instead of its depth.

A slice-by-slice overview of Patient #2's left femur can be seen in Table 5.18 in order to provide an inside-look at the measurements we obtained. In order to better read the table, here some landmark slices are provided. It should be noted that this particular femur did not have a narrow pit between the greater trochanter and the femoral head/neck.

### 5.6.4 Comparison

Qualitative metrics are the easiest way to compare the results from our method against the results previously published work. Unfortunately, quantities results are not always presented in research, and if they are, there is no standardized set of metrics. Taking into account that different segmentation strategies are validated under different conditions and databases, comparing the effectiveness of our methods against the implementations of others using these metrics is done under a best-effort approach.

Our segmentation strategy returns results which are quite close to the target manual segmentations. With an average surface distance of 0.28 ± 0.04mm from the manual model's contour, we are already within the 1-2 voxel (0.68-1.36mm) variability typical of manual segmentations [23].

The published method whose conditions were most similar to our own comes from Shmid's 2008 paper [54] describing a method of segmenting the femur and pelvic bones from low-resolution MRI datasets. Their method uses Principle Component Analysis to define global shape variations and Markov Random Field for local deformations. After testing six datasets, they reported a mean accuracy of 1.44 ± 1.1mm.

A method to segment the femurs and pelvic bones suffering from osteoarthritis was also proposed [55] by Yokota et al. in 2009. They accomplish this by embedding shape and pose variations for the femur and pelvis into a combined statistical shape model. They're best results

were obtained with a Hierarchical SSM; 1.20mm average distance for the overall hip shape and 1.78mm average distance for regions around the joint space. Their dataset consisted of 44 single-sided female hips; some of which were diagnosed with osteoarthritis, while others were asymptomatic.

Most recently (2011), Schmid et al. published [56] a model-based s method to segment the femur and pelvic bones from MRI datasets with low fields of view. They reported an $SSD_{Avg}$ of $1.21 \pm 0.53$mm, a $SSD_{max}$ of $7.57 \pm 2.46$ and a VOE of $18.02 \pm 6.12\%$ with their high-resolution, low field-of-view, MRI scans of the human femurs. Their dataset consisted of 43 healthy femurs.

# Chapter 6 - Conclusion

In this thesis, we described a method to segment a femur from a CT scan. This method is targeted towards segmenting femurs with pathological shape irregularities, making them poor subjects for model-based methods. Our motivating challenge was to segment femurs suffering from Femoral-Acetabular Impingements; an illness where a bony bump can exist on (or near) the head-neck junction of a femur. Our segmentation of these bones will be used to develop patient-specific 3D models of the femur, which can be used by surgeons during pre-operative planning for correction of FAIs and kinematic modelling of hip movement.

We initiate the segmentation procedure by having the user subdivide the femur into two regions (the near-spherical head and the vertically tubular body) and used two levels of segmentation (rough and fine). A number of pre-processing steps are employed on each ROI's volume to improve the shape and accuracy of our methodology, such as replacing sections of the acetabulum with low-gradient fill, using a flooring threshold to merge together different layers of soft tissue and using a ceiling threshold to emphasize voxels likely to be composed one bone. Afterwards, we segment the femur-head followed by the femur-body using a sequential set of related morphological snake operations. We finish our method by computing the union of the femur-head and femur-body's segmentation. Our method is very accurate for both non pathological hips and hips suffering from CAM-type impingements. From a dataset of 12 femurs, 6 of which were diagnosed with FAIs and the other 6 being asymptomatic, we recorded a *global volume overlap error* of **2.71 ± 0.44%**, and an *average symmetric surface distance* of **0.28 ± 0.04mm**. These results are a marked improvement over all other surveyed literature and sufficiently accurate to be used to in the creation of patient-specific 3D models.

The segmentation process is also easy to operate, requiring roughly a minute of the user's time to initialize and another ten minutes for the automated segmentation process to complete. The gold standard for segmentations of a CT scan can take days of arduous labelling of individual voxels, depending on the resolution of the CT scan. Given its speed and accuracy, our methodology could be used as a tremendous accelerant to completing manual segmentations. To this end, our method could be used to provide an initial model for the femur, at which point a radiologist could perform some minor relabeling of voxels to achieve a fast patient-specific model.

## 6.1 Contributions

Our contribution can be summarised with the following sentence:

- We detailed a method to segment femurs from CT scans, including femurs suffering from Femoral Acetabular Impingements, quickly and, on average, more accurately than any other semi-automatic method found in literature.

## 6.2 Future Research

At present, our method's largest short-falling is its concentration of high errors in slices at the tops of femur heads and in the pits near the greater trochanter. Resolving the former short-falling is made difficult by the blurry & noisy nature of cross-sections of the femur in its top-most slices. Resolving the latter short-falling is made difficult by a morphological snake's tendency to prematurely abort curve evolution into narrow concavities. We hope to be able to curb these respective sources of errors by introducing additional landmarks during the user-initialisation phase of our method.

Furthermore, we will expand our sample set of femurs to include all 40 femurs from the 20 patients in our database. As new manual segmentations become available from the Ottawa General Hospital, we will integrate their automated segmentation results to further evaluate the robustness of our method.

The next step in our research is to build an anatomical map of the hip and study the hip motion dynamics to further the diagnosis and treatment of FAIs. This will include not only femurs suffering from CAM-type impingements but also PINCER-types in acetabulums.

# References


[1] R. C. Gonzalez and R. E. Woods, *Digital Image Processing*, 3rd ed.: Pearson Prentice Hall, 2008.

[2] L. G. Shapiro and G. C. Stockman, *Computer Vision*.: Prentice-Hall, 2001.

[3] L. M. Ochoa, L. Dawson, J. C. Patzkowski, and J. R. Hsu, "Radiographic Prevalence of Femoroacetabular Impingments in a Young Population with Hip Complaints Is High," *Clinical orthopaedics and related research*, vol. 468, no. 10, pp. 2710-2714, 2010.

[4] M. Schuenke et al., *THIEME Atlas of Anatomy Series DVD1: General Anatomy and Musculoskeletal System*, 1st ed.: Thieme Medical Publishers, 2005.

[5] A. Agur and A. Dalley, *Grant's Atlas of Anatomy*, 12th ed.: Lippincott William & Wilkins, 2009.

[6] C. R. Wheeless the 3rd. (2010, September) Articular Cartilage - Wheeless' Textbook of Orthopaedics. [Online]. http://www.wheelessonline.com/ortho/articular_cartilage

[7] M. Hossain and J. G. Andrew, "Current Management of femoro-acetabular impingement," *Current Orthopaedics*, vol. 22, no. 4, pp. 300-310, 2008.

[8] J. C. Thompson, *Netter's Concise Altas of Orthopeadic Anatomy*, 1st ed.: Saunders, 2001.

[9] D. C. Rizzo, *Delmar's Fundamentals of Anatomy & Physiology*. Albany, United States of America: Delmar a division of Thompson Learning, 2001.

[10] L. Slomianka. (2009, Aug.) Blue Histology - Skeletal Tissues - Bone - School of Anatomy and Human Biology - The University of Western Australia. [Online]. http://www.lab.anhb.uwa.edu.au/mb140/CorePages/Bone/Bone.htm

[11] D. Field and J. O. Hutchinson, *Field's Lower Limb Anatomy, Palpation and Suface Markings*, 1st ed.: Churchill Livingstone, 2008.

[12] Dorling Kindersley. (2010) Ball and socket - free clip art - Dorling Kindersley. [Online]. http://www.dorlingkindersley-uk.co.uk/nf/ClipArt/Image/0,_1582263,00.html

[13] Dorling Kindersly. (2010) Hinge joint - free clip-art - Dorling Kindersley. [Online]. http://www.dorlingkindersley-

uk.co.uk/nf/ClipArt/Image/0,239033_1582265_239069,00.html

[14] M. H. M. Lee and A. Moroz. (2009, February) Physical Therapy (PT): Rehabilitation: Merck Manual Professional. [Online]. http://www.merck.com/mmpe/sec22/ch336/ch336b.html

[15] P. E., Allen, D. J. Beaule, J. C. Clohisy, P. Schoenecker, and M. Leunig, "The Young Adult with Hip Impingment: Deciding on the Optimal Intervention," *Journal of Bone & Joint Surgery*, vol. 91-A, no. 1, pp. 210-221, 2009.

[16] E. J. Zaragoza and P. E. Beaule, "Imaging of the painful non-artitic hip: Apractical approach to surgical relevancy," *Operative Techniques in Ortopaedics*, vol. 14, no. 2, pp. 42-48, 2004.

[17] M. Tannast, K. A. Siebenrock, and S. E. Anderson, "Femoroacetabular Impingment: Radiographic Diagnosis - What the Radiologist Should Know," *American Journal of Roentgenology*, vol. 188, pp. 1540-1552, 2007.

[18] "Tannast, M.; Diebenrock, K. A.; Anderson, S. E," *American Journal of Roentgenology*, vol. 188, pp. 1540-1552, 2007.

[19] M. Leunig and R. Ganz, "Femoroacetabular impingement: A common cause of hip complants leading to arthrosis," *Der Unfallchirurg*, vol. 108, no. 1, pp. 9-17, Jan 2005.

[20] A. Weir, R. J. de Vos, M. Moen, and J.L. Tol, "Prevalence of radiological signs of femoroacetabular impingment in patients presenting with long-standing adductor-related groin pain," *British Journal of Sports Medicine*, July 2009.

[21] A. Takeyama, M. Naito, K. Shiramizu, and T. Kiyama, "Prevalence of femoraacetabular impingment in Asian patients with osteoarthitis of the hip," *International Ortopaedics*, vol. 33, no. 5, pp. 1229-1232, 2009.

22] S. A. Jackson and R. M. Thomas, *Introduction to CT Physics*. Edinburgh: Churchill Livingstone, 2004.

[23] M. R. Kaus et al., "Automated 3-D PDM Construction From Segmented Images Using Deformable Models," *Medical Imaging, IEEE Transactions on*, vol. 22, no. 8, pp. 1005-1013, 2003.

[24] K. Kass, A. Witkin, and D. Terzopoulos, "Snakes: Active Contour Models," *International Journal of Computer Vision*, vol. 1, no. 4, pp. 321-331, 1987.

[25] L. Cohen, "On Active Contour Models and balloons," *CVGIP: Image Understanding*, vol. 53, no. 2, pp. 211-218, 1991.

[26] L. D. Cohen and I. Cohen, "Finite-Element Methods for Active Contour Models and Balloons for 2-D and 3-D Images," *Pattern Analysis an Machine Intelligence, IEEE Transactions on*, vol. 15, no. 11, pp. 1131-1147, 1993.

[27] C. Xu and J. L. Prince, "Snakes, Shapes, and Gradient Vector Flow," *Image Processing, IEEE Transactions on*, vol. 7, no. 3, pp. 359-369, 1998.

[28] T. McInerney and D. Terzopoulos, "T-snakes: Topology Adaptive Snakes," *Medical Image Analysis*, vol. 4, no. 2, pp. 73-91, 2000.

[29] R. Malladi, J.A. Sethian, and B.C. Vemuri, "Shape Modeling with Front Propagation: a Level Set Approach," *Pattern Analaysis and Machine Intelligence, IEEE Transactions on*, vol. 12, no. 2, pp. 158-175, 1995 2005.

[30] M.E. Leventon, W.E.L. Grimson, and O Faugaras, "Statistical Shape Influsence in Geodesic Active Contours," in *Computer Vision and Pattern Recongnition, Proceedings of the IEEE Conference on*, 2000, pp. 316-323.

[31] V. Caselles, R. Kimmel, and G. Sapiro, "Geodesic Active Contours," *Computer Vision, International Journal of*, vol. 22, no. 1, pp. 61-79, 1997.

[32] K. Siddiqi, Y. B. Lauriziere, A Tannenbaum, and S. W. Zucker, "Area and Length Minimizing Flows for Shape Segmentation," in *Computer Vision and Pattern Recognition, Proceedings of the 1997 Conference on*, 1997, pp. 621-627.

[33] T. Chan and L. A. Vese, "Active Contours Without Edges," *Images Processing, IEEE Transactions on*, vol. 10, no. 2, pp. 266-277, 2001.

[34] L. A. Vese and T. F. Chan, "A Multiphase Level Set Framework for Image Segmentation Using the Mumford and Shah Model," *Computer Vision, International Journal of*, vol. 50, no. 3, pp. 271-293, 2002.

[35] X. Wang, L. He, and W. Wee, "Deformable Contour Method: A Constrained Optimization Approach," *Computer Vision, International Journal of*, vol. 59, no. 1, pp. 87-108, 2004.

[36] J. A. Sethian, "A fast marching level set method for monotonically advancing fronts," *Proceedings of the National Academy of Sciences of the United States of America*, vol. 93, pp. 1591-1595, February 1996.

[37] L. Álvarez, L. Baumela, P. Henríquez, and P. Márquez-Neila, "Morphological Snakes," in *Computer Vision and Pattern Recognition, IEEE Conference on*, San Francisco, 2010.

[38] T.F. Cootes, C.J. Taylor, D. H. Cooper, and J Graham, "Training Models of Shape from Sets of Examples," in *British Machine Vision Conference, Proceedings of*, 1992, pp. 9-18.

[39] W. W. Song et al., "Model-Based Segmentation of Femoral Head and Acetabulum from CT Images," *Complex Medical Engineering, IEEE/ICME International Conference on*, pp. 586-590, 2007.

[40] T. F. Cootes, C. J. Taylor, D. H. Cooper, and J. Graham, "Active Shape Models - Their Training and Application," *Computer Vision and Image Understanding*, vol. 61, no. 1, pp. 38-59, 1995.

[41] T. F. Cootes, G. J Edwards, and C. J. Taylor, "Active Appearance Models," *European Conference on Computer Vision, Proceedings on*, vol. 2, pp. 484-4498, 1998.

[42] T. F. Cootes and C. J. Taylor, "Modelling object appearance using grey-level surface," in *British Machine Vision, Proceedings of the conference on*, 1994, pp. 479-488.

[43] D. Cremers, C. Schnörr, J. Weickert, and C. Schellewald, "Diffusion-Snakes Using Statistical Shape Knowledge," *Notes in Computer Science*, vol. 1888, pp. 164-174, 2000.

[44] D. Cremers, C. Schnorr, and J. Weickert, "Diffusion-Snakes: Combining Statistical Shape Knowledge and Image Information in a Variational Framework," in *Variational and Level Set Methods in Computer Vision, Proceedings of the IEEE Workshop On*, 2001, pp. 137-144.

[45] D. Cremers, F. Tischhauser, J. Weickert, and C. Schnorr, "Diffusion Snakes: Introducing Statistical Shape Knowledge into the Mumfor-Shah Functional," *Computer Vision, International Journal of*, vol. 50, no. 3, pp. 295-313, 2002.

[46] Y. Chen et al., "Using Prior Shapes in Geometric Active Contours in a Variational Framerwork," *Computer Vision, International Journal on*, vol. 50, no. 3, pp. 315-328, 2002.

[47] D. Cremers, S. J. Osher, and S. Soatto, "Kernel Density Estimation and Intrinsic Alignment for Shape Priors in Level Set Segmentation," *Computer Vision, International Journal of*, vol. 69, no. 3, pp. 335-351, 2006.

[48] F. Rosenblatt, "Remarks on some nonparametric estimates of a density function," *Annals of Mathematical Statistics*, vol. 27, pp. 832-837, 1956.

[49] S. Chen and R. J. Radke, "Level Set Segmentataion with Both Shape and Intensity Priors," in *Computer Vision, IEEE 12th Internation Conference on*, 2009, pp. 763-770.

[50] L. V. Safont and E. M. Marroquin, "3D Reconstruction of Third Proximal Femur (31-) with Active Contours," in *Image Analysis and Processing, Proceedings of the International Conference on*, 1999, pp. 458-463.

[51] R. A. Zoroofi et al., "Automated Segmentaiton of Acetabulum and Femoral Head From 3-D CT Images," *Information Technology in Biomedicine, IEEE Transactions on*, vol. 7, no. 4, pp. 329-343, 2003.

[52] N. Magnenat-Thalmann, L. Yahia-Cherif, B. Gilles, and T. Molet, "Hip Joint Reconstruction and Motion Visualization Using MRI and Optical Motion Capture," *Biomedizinische Technik/Biomedical Engineering*, vol. 48, no. s1, pp. 20-23, 2003.

[53] B. Gilles, L. Moccozet, and N. Magnenat-Thalmann, "Anatomical Modelling of the Musculoskeletal Systems," in *Medical Image Computing and Computer Assisted Intervention, International Conference on*, 2006, pp. 289-296.

[54] J. Schmid and N. Magnenat-Thalmann, "MRI bone segmentation using deformable models and shape priors.," *Medical Image Computing and Computer Assisted Intervention*, vol. 11, pp. 119-126, 2008.

[55] F. Yokota et al., "Automated Segmentation of the Femur and Pelvis from 3D CT Data of Diseased Hip Using Hierarchical Statistical Shape Model of Joint Structure," *Medical Image Computing and Computer Assisted Intervention - Lecture Notes in Computer Science*, vol. 5762, pp. 811-818, 2009.

[56] J. Schmid, J. Kim, and Nadia Magnenat-Thalman, "Robust statistical shape models for MRI bone segmentation in presence of small field of view," *Medical Image Analysis*, vol. 15, pp. 155-168, 2011.

[57] Behrang Amini. Healthbase. [Online]. http://www.healthbase.com/resources/medical-library/orthopedic/femur-angles.html

[58] L., Beumela, L., Marquez-Neila, P., Henriquez, P. Alvarez. (2010) Image Processing On Line. [Online]. http://www.ipol.im/pub/algo/abmh_real_time_morphological_snakes_algorithm/

59] P. H. Abrahams, S. C. Marks Jr, and R. T. Hutchings, *MCMinn's Color Atlas of Human Anatomy (CD ROM)*, 5th ed.: Mosby, 2002.

[60] R. C. Gonzalez and R. E. Woods, "Morphological Image Processing: Dilation," in *Digital Image Processing*.: Pearson Education, 2008, ch. 9.2.2, pp. 633-635.

[61] L. He et al., "A comparative study of deformable contour methods on medical image segmentation," *Image and Vision Computing*, pp. 141-163, 2008.

[62] L. A. F. Fernandes and M. M. Oliveira, "Real-timeline detection through an improved Hough transform voting scheme," *Pattern Recognition*, vol. 41, no. 1, pp. 299-314, January 2008.

[63] National Electrical Manufacturers Assosciation (NEMA). (2010) DICOM Homepage. [Online]. http://medical.nema.org/

[64] S. Stegmaier, M. Strengert, T. Klein, and T. Ertl, "A Simple and Flexible Volume Rendering Framework for Graphics-Hardware-based Raycasting," in *Volume Graphics, Proceedings of*, New York, USA, 2005, pp. 187-195.

[65] G. W. Sherouse, K. Novins, and E. L. Chaney, "Computation of digitally reconstructed radiographs for use in radiotherapy treatment design," *Radiation Oncolohy * Biology * Physics, International Journal of*, vol. 18, no. 3, pp. 651-658, March 1990.

[66] W Niessen et al. 3D Liver Tumor Segmentation Challenge 2008 - Home. [Online]. http://lts08.bigr.nl/about.php

[67] =Benjamin=. (2010, June) Introduction to Regional Anatomy/Lesson 3 - Wikiversity. [Online]. http://en.wikiversity.org/wiki/Introduction_to_Regional_Anatomy/Lesson_3

[68] Y. Mrabet. (2008, June) File:Human anatomy planes-ES.png - Wikimedia Comons. [Online]. http://commons.wikimedia.org/wiki/File:Human_anatomy_planes-ES.png

[69] T. F. Cootes, D. H. Cooper, C. J. Taylor, and J. Graham, "Trainable method of parametric shape description," *Image and Vision Computing*, vol. 10, no. 5, pp. 289-294, 1992.

[70] R. Malladi, J.A. Sethian, and B.C. Vemuri, "Shape Modeling with Front Propagation: a Level Set Approach," vol. 12, no. 2, pp. 158-175, 1995.

[71] F. Yokota et al., "Automated Segmentation of the Femur and Pelvis from 3D CT Data of Diseased Hip Uding Hierachical Statistical Shape Model of Joint Structure," *Medical Image Computing and Computer-Assisted Intevention: Lecture Notes from Computer Science*, vol. 5762, pp. 811-818, 2009.

# Appendix A Anatomical Terms

*Table 6.1 List of Anatomical Directions*

| Term | Direction |
|---|---|
| Anterior (Ventral) | Towards the front |
| Posterior (Dorsal) | Towards the back |
| Lateral | Towards the side (or away from the midline) |
| Medial | Nearest to the midline of the body |
| Superior | Uppermost or above |
| Inferior | Lowermost or below |
| Proximal | Nearest to the point of attachment or origin |
| Distal | Away from the point of attachment or origin |
| Cranial (Cephalic) | Towards the head |
| Caudal | Towards the tail (or synonym for Inferior) |

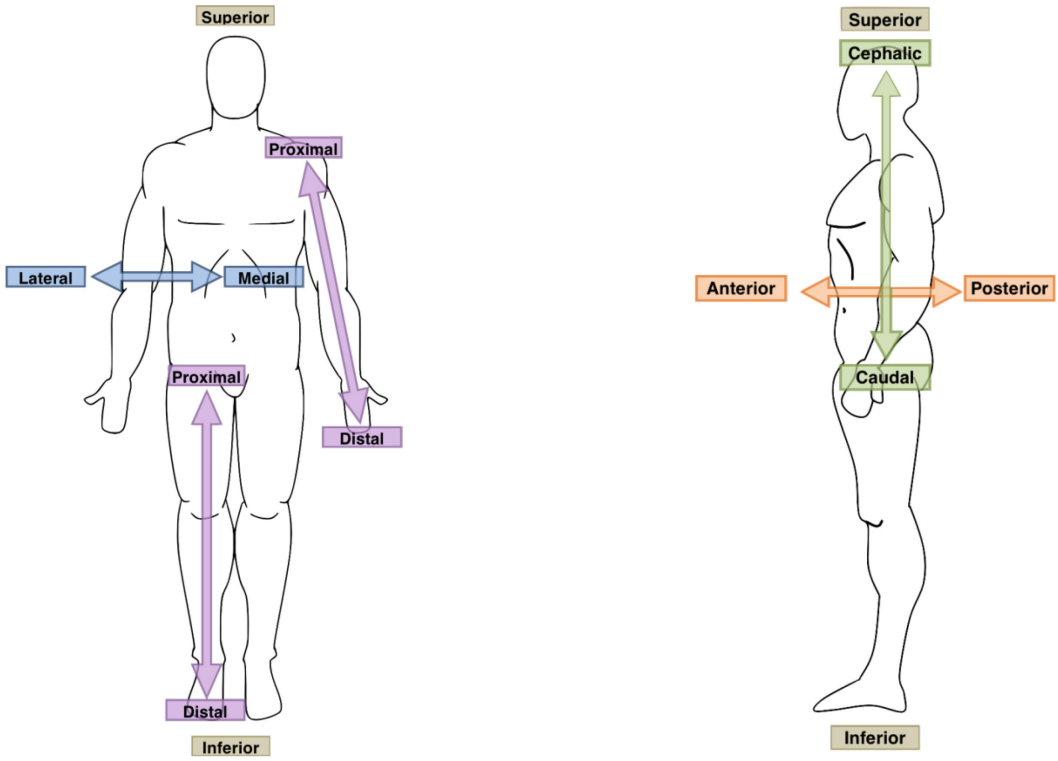


*Figure 6.1 Human Anatomical Directions [67]*

*Table 6.2 List of Anatomical Planes*

| **Term** | **Plane** |
|---|---|
| Midsagital | Plane that vertically divides the body through the midline into two equal left and right portions (or halves) |
| Sagital | Plane parallel to the midsagital plane dividing the body into unequal right and left portions |
| Coronal | Plane that divides the body into anterior and posterior portions |
| Transverse | Plane that divides the body into superior and inferior portions |

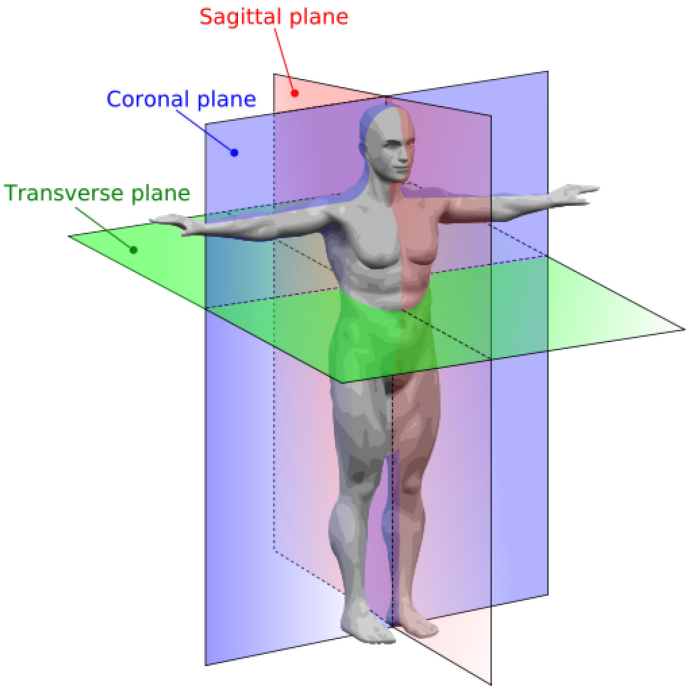


*Figure 6.2 Planes of human anatomy [68]*